Staged Attitude-Metrology Pointing Control and Parametric Integrated Modeling for Space-based Optical Systems

by

Ryan S. Lim

Submitted to the Department of Aeronautics and Astronautics
in partial fulfillment of the requirements for the degree of

Master of Science in Aeronautics and Astronautics

at the

MASSACHUSETTS INSTITUTE OF TECHNOLOGY

May 2006

Author ....
Department of Aeronautics and Astronautics
May 26, 2006

Certified by...
David W. Miller
Professor of Aeronautics and Astronautics
Thesis Supervisor

Accepted by...
Jaime Peraire
Professor of Aeronautics and Astronautics
Chair, Committee on Graduate Students

Staged Attitude-Metrology Pointing Control and Parametric Integrated Modeling for Space-based Optical Systems

by

Ryan S. Lim

Submitted to the Department of Aeronautics and Astronautics
on May 26, 2006, in partial fulfillment of the
requirements for the degree of
Master of Science in Aeronautics and Astronautics

Abstract

The quest for higher sensitivity and finer angular resolution in astronomy demands larger and more complex space imaging systems. This thesis presents the concepts developed for two different technologies that have the potential to contribute in improving the performance of space imaging systems.

The first technology is precision pointing control technology, which can provide fine optical control operating in conjunction with coarse formation flying attitude control in order to meet the stringent optical requirements. This will potentially enable a long baseline Formation Flying Interferometer (FFI) such as NASA's Terrestrial Planet Finder (TPF). The concept for precision pointing control was realized by a testbed called the Precision Pointing Optical Payload (PPOP). The design and implementation of the PPOP are described, followed by an experimental demonstration of staged pointing control. The global metrology system of the Synchronized Position Hold Engage Reorient Experimental Satellites (SPHERES) provides coarse attitude control, whereas the PPOP provides fine pointing control using a set of fast steering mirrors.

The second technology investigates parametric integrated modeling of space telescopes. This technology provides a design tool for examining alternative telescope architectures and identifying favorable architectures at an early stage of the design lifecycle. The MIT Space Systems Laboratory (MIT-SSL) is currently developing a parametric integrated model for a Modular Optical Space Telescope (MOST). This thesis provides an overview of the MOST model, with emphasis on the development of the optics sub-model. ZEMAX is used for calculating the wave front error based on the Zernike sensitivity analysis. A data interface between ZEMAX and MATLAB has been developed, which makes the process of performing the Zernike sensitivity analysis automated.

Thesis Supervisor: David W. Miller
Title: Professor of Aeronautics and Astronautics

Acknowledgments

I would like to thank my advisor Prof. David W. Miller for his guidance and support, and for providing me an opportunity to be a part of the MIT Space Systems Laboratory. There are not many places on earth where you can study theory, implement it on hardware, and actually see the hardware flying aboard the International Space Station. How exciting! I feel truly blessed to be able to call myself a "SSLer".

I would like to particularly acknowledge Dr. Alvar Saenz-Otero for both his friendship and technical support throughout the development of the Precision Pointing Optical Payload. Without his help and encouragements, it would have been impossible to finish this work. I appreciate greatly the helps from my friends and colleagues at the MIT Space Systems Laboratory. Specifically, I would like to mention Dr. Raymond Sedwick, Dr. Edmund Kong, Simon Nolet, Soonjo Chung, Scott Uebelhart, Daniel Kwon, Sangil Lee, and Jaemyung Ahn. Paul Bauer deserves special credit for his support with electronics.

Most of all, I cannot thank enough my family for their unlimited love, encouragements, and sacrifices.

Contents

List of Figures

List of Tables

Abbreviations

CCD	Charge Coupled Device
CST	Controlled Structures Technology
DDE	Dynamic Data Exchange
FAM	Full Aperture Metrology
FEM	Finite Element Model
FOV	Field of View
FSM	Fast Steering Mirror
GPIO	General Purpose Input Output
GPS	Global Positioning System
GSP	Guest Scientist Program
HM	Hybrid Metrology
HST	Hubble Space Telescope
IMU	Inertial Measurement Unit
ISS	International Space Station
LOS	Line of Sight
MACE	Middeck Active Control Experiment
MCM	Multi Chip Module
MIT	Massachusetts Institute of Technology
MOST	Modular Optical Space Telescope
OPD	Optical Path Difference
PADS	Position and Attitude Determination System
PPOP	Precision Pointing Optical Payload
SAM	Sub Aperture Metrology

SPHERES	Synchronized Position Hold Engage Reorient Experimental Satellites
Sphere	SPHERES micro-satellite
SSL	Space Systems Laboratory
STL	Satellite to Laptop
STS	Satellite to Satellite
TPF-FFI	Terrestrial Planet Finder Formation Flying Interferometry
WFE	Wave Front Error

Chapter 1

Introduction

1.1 Motivation

The quest for higher sensitivity and finer angular resolution in astronomy demands larger and more complex space imaging systems. While the Hubble Space Telescope (HST) has performed remarkably well over the past decades [18], using conventional monolithic systems such as the HST for further improving optical performance is prohibited due to both the cost associated with manufacturing large mirrors and the limited payload carrying capabilities of the current launch systems. The next generation of space telescopes, such as the ones proposed by NASA's Origins mission (Figure 1-1), explores a wide variety of advanced technologies and seeks to allow larger, lightweight optics to replace conventional monolithic telescopes.

When developing technologies for space imaging systems, issues such as cost, deployment, and precision of the optical systems must be addressed. A modular design approach can be used to reduce production cost by utilizing standardized interfaces. A modular design approach also increases the lifetime of spacecraft by providing the option of replacing only specific failed subsystems. When it is combined with formation flying technology, a modular design approach allows space systems to easily upgrade to new configurations, possibly providing testbeds for multiple space missions. The Self-assembling Wireless Autonomous Reconfigurable Modules (SWARM) project [8] (Figure 1-2) developed at the MIT Space Systems Laboratory (MIT-SSL)

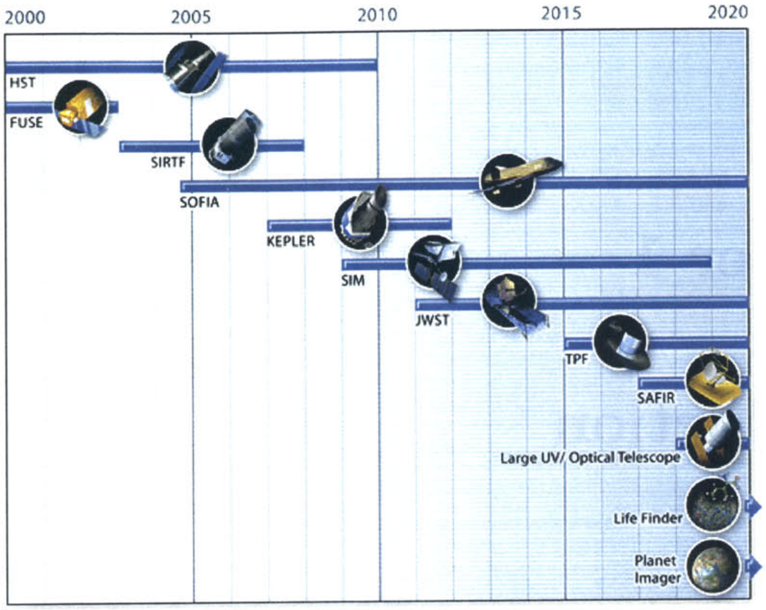

Figure 1-1: Timeline of NASA Origins missions [6]

demonstrated the use of a modular spacecraft that is capable of self-assembly and reconfiguration. Technology developments in lightweight space systems such as NASA's James Webb Space Telescope (JWST) [9] also provide benefit in cost by reducing areal density and therefore launch mass.

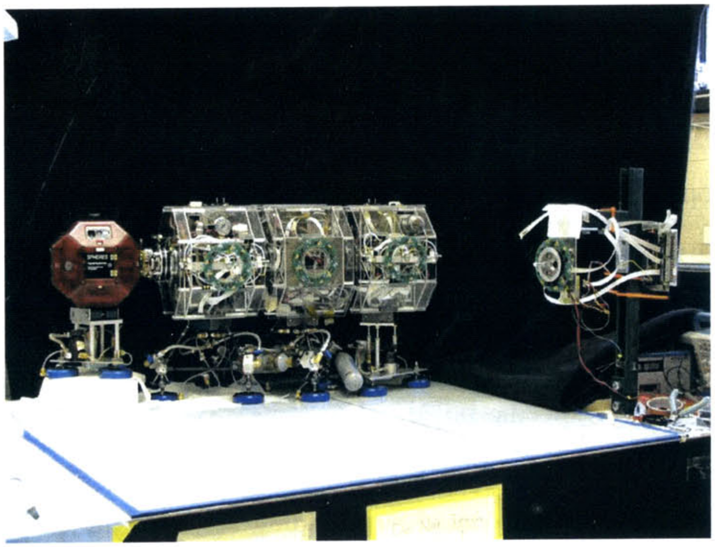

Figure 1-2: SWARM testbed developed at MIT-SSL

Another issue that needs to be considered when developing technologies for space imaging systems is deployment. Two different concepts are generally considered for deployment of future space imaging systems. The first concept is to deploy and assemble a space system by unfolding structurally connected subsystems. For example, the concept currently developed for the JWST (Figure 1-3) requires unfolding of solar panels, high-gain antenna, sunshield, separation tower, and segmented mirrors, following a pre-optimized sequence once the satellite is in orbit [9]. Deploying multiple segmented mirrors provides a way to increase aperture dimension beyond that which fits within the current launch shrouds. With a longer baseline for the effective aperture, finer angular resolution, far better than the HST offers, can be achieved.

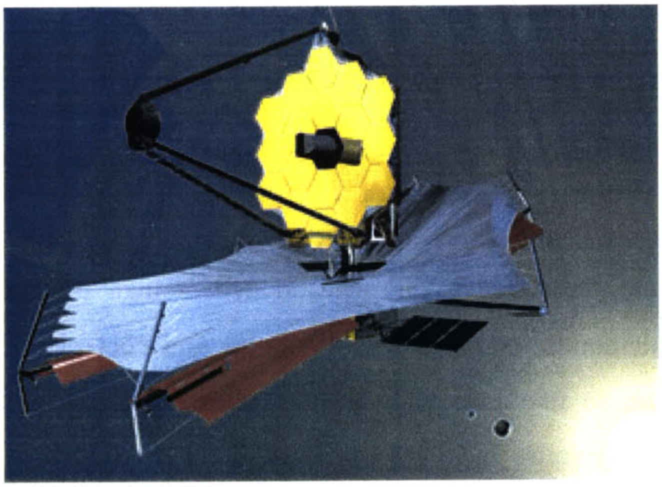

Figure 1-3: James Webb Space Telescope (courtesy of NASA)

The other concept is to deploy using formation flying technology. Formation flying technology provides an alternative approach to flying large structures in space. Instead of one large instrument, several smaller spacecraft are deployed and brought together to work as one complete system. In the concept developed for NASA's Terrestrial Planet Finder Formation Flying Interferometer (TPF-FFI) (Figure 1-4), five spacecraft, flying in formation about one kilometer apart, function as an optical interferometer [10]. Four of the spacecraft have telescopes, while the fifth acts as a combiner. Optical interferometry combines observations from multiple telescopes of the same target to achieve the results of a much larger telescope. The further apart the individual telescopes are, the finer is the resolution at the expense of the decreased sensitivity.

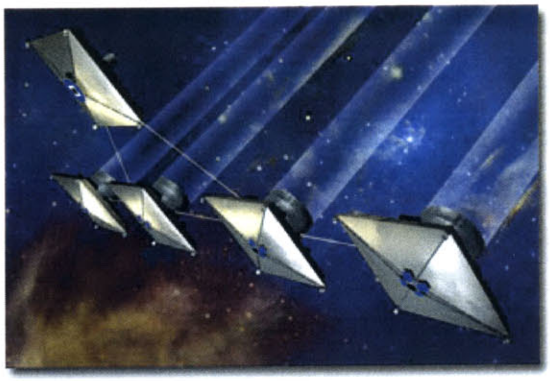

Figure 1-4: Terrestrial Planet Finder Formation Flying Interferometer (courtesy of NASA)

Along with the challenges posed by cost and deployment, space imaging systems must meet stringent positional tolerances and deliver high precision optics. This results in heavy demands on structural dynamics and controls. There are many available techniques to maintain high level of precision on a large, flexible space structure. These techniques include Controlled Structures Technology (CST) [19], application of passive and active damping, isolation, and active shape control. The Middeck Active Control Experiment (MACE) [11] testbed developed by the Space Engineering Research Center at the Massachusetts Institute of Technology flew on STS-67 in March of 1995, and successfully demonstrated various advanced control concepts under the influence of common spacecraft vibrational disturbances [26].

As mentioned so far, building high performance space imaging systems require consideration of various issues and technology developments in multi-disciplinary areas (Figure 1-6). This thesis presents two of such technologies, precision pointing control and parametric integrated modeling, that can contribute to the development of high performance space imaging systems. The capability of controlling the atti-

Figure 1-5: Middeck Active Control Experiment (MACE) hardware aboard the International Space Station

tudes of multiple free flying objects with finer accuracy opens up the possibility of realizing an optical system with a longer baseline such as seen in the concept developed for the TPF-FFI, which in turn will provide finer angular resolution according to the Rayleigh criterion. As will be discussed in Chapters 2 through 4, concepts for precision pointing control have been developed and realized by a testbed called the Precision Pointing Optical Payload (PPOP). The global metrology system of the Synchronized Position Hold Engage Reorient Experimental Satellites (SPHERES) provides coarse formation attitude control and the PPOP provides fine pointing control using a set of fast steering mirrors, thus forming a staged pointing control. Identical PPOPs will be mounted to each SPHERES satellite, which will provide modular testbed for precision pointing control experiments.

On the other hand, parametric integrated modeling provides the tools and techniques for designing high fidelity space imaging systems. It enables identifying the uncertainties and flexibilities embedded in complex systems at an early stage in the design process, and provides favorable architectures for further analysis, thus mitigating the risk of costly redesigns later. The MIT Space Systems Laboratory (MIT-SSL) is examining alternative architectures for a Modular Optical Space Telescope (MOST) by developing a simulation tool that automatically produces unique realizations of a space telescope model based on parametric inputs. Various control techniques are examined on the state-space integrated model created by the DOCS (Disturbance, Optics, Controls, and Structures) toolbox [15] in the MOST model, and favorable architectures are chosen based on the performance outputs such as line of sight jitter and wave front error.

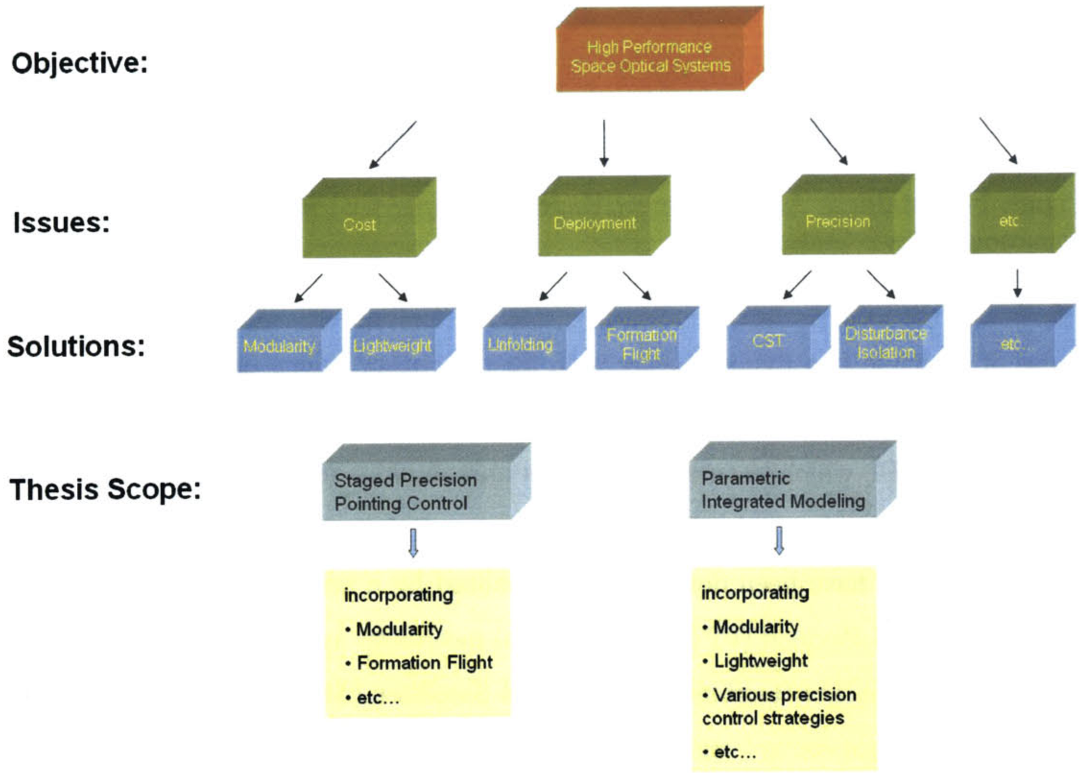

Figure 1-6: Developing high performance space optical systems: various challenges and possible solutions. This thesis presents two such solutions: precision pointing control and parametric integrated modeling.

1.2 Thesis Objectives

- To develop and demonstrate staged pointing control technology
- To provide tools and techniques for designing high fidelity optical systems through the development of a parametric integrated model for a Modular Optical Space Telescope

1.3 Thesis Outline

- Chapter 2 introduces several concepts developed for precision pointing control and discusses the concept chosen for a testbed development.
- Chapter 3 presents the design and development of a ground-based testbed, which seeks to demonstrate staged pointing control.
- Chapter 4 discusses the results from ground-based tests, which demonstrated staged pointing control.
- Chapter 5 discusses the development of a parameterized integrated model for a Modular Optical Space Telescope with emphasis on optics sub-model development.
- Chapter 6 summarizes the results from this thesis and offers suggestions for future work.

Chapter 2

Concepts of Precision Pointing Optical Payload

As mentioned in the previous chapter, one of the technologies that can potentially contribute in improving the performance of space imaging systems is precision pointing control technology. In order to demonstrate precision pointing control in a laboratory environment, staged pointing control concepts have been developed at the MIT-SSL. For coarse pointing control, the global metrology system of the Synchronized Position Hold Engage Reorient Experimental Satellites (SPHERES) is used. Fine pointing control is provided by a testbed named "Precision Pointing Optical Payload (PPOP)." This chapter provides a general description of the concepts developed for the PPOP. First, a brief overview of the SPHERES testbed is provided, and the limitations of the ultrasound metrology system currently implemented on each of the SPHERES satellites ("Spheres") are discussed. Then, performance requirements and the concepts developed for the PPOP are introduced. This chapter concludes with a description of the final concept chosen and the necessary modifications made on the initial design for the PPOP.

2.1 SPHERES: The Mothership

This section provides an overview of the SPHERES testbed. Much more detailed description of the SPHERES testbed can be found in [24], [34], and [35].

2.1.1 Overview

The Synchronized Position Hold Engage Reorient Experimental Satellites (SPHERES) testbed provides a facility to demonstrate and validate formation flight, estimation, and autonomy algorithms. The SPHERES testbed was specifically designed to reduce the high risk associated with flying untested space missions by providing an inexpensive, risk-tolerant laboratory environment for algorithm development and verification prior to an actual space mission.

The SPHERES operations plan is based on three different stages of development: initial algorithm development using the SPHERES simulation, experimentation on Spheres at the MIT Space Systems Laboratory (MIT-SSL), and 6DOF tests onboard the International Space Station (ISS). First, researchers independently develop custom algorithms using the SPHERES simulation. Through the unique interface framework provided by the Guest Scientist Program (GSP) [21], remote researchers compile, implement, and test their custom algorithms and iterate, if necessary, the code development process until desired results are achieved. Once acceptable performance has been demonstrated using the simulation, the algorithms are sent to the MIT-SSL for verification on the flight hardware in 2D. After the algorithms are tested on the flight hardware and optimized, the algorithms are sent to the ISS for 6DOF tests.

The SPHERES testbed consists of a number of autonomous micro-satellites (Spheres), metrology and communication systems hardware, and a computer that serves as a ground station. Each Sphere is self-contained, meaning that all the subsystems required for 6DOF maneuvers are embedded within each satellite. These embedded systems include propulsion, communications, and position/attitude determination system, power, and control subsystems. The propulsion subsystem consists of twelve cold-gas thrusters, a tank containing liquid carbon dioxide, a pressure reg-

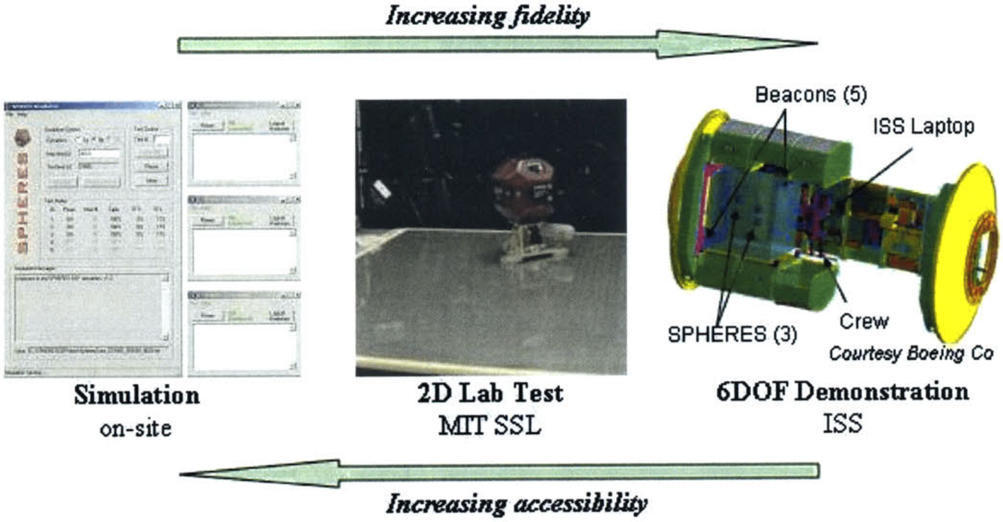

Figure 2-1: Three stages of the SPHERES operations plan

ulator, a pressure gage, and solenoid-actuated micro-valves. The twelve thrusters are positioned carefully to provide controllability in all six degrees of freedom. The communication subsystem consists of two independent radio frequency channels: the Sphere-To-Sphere (STS) channel and the Sphere-To-Laptop (STL) channel. The STS channel is used for communication among the Spheres and the STL channel is used for communication between the Spheres and the computer station. Ultrasound beacons and inertial measurement units form the position and attitude determination system (PADS), which provides real time position and attitude information to each satellite. The PADS will be further discussed in Section 2.1.2. Two AA-battery packs are used to power up each Sphere, providing operating time of approximately ninety minutes. The control subsystem produces thruster on-time commands based on required force and torque generation profile. A picture of the actual SPHERES flight hardware is shown in Figure 2-2. Physical properties of Spheres are listed in Table 2.1.

Figure 2-2: SPHERES satellite

Diameter	0.25 m
Mass	4.0 kg
Max Linear Acceleration	0.17 m/s^2
Max Angular Acceleration	3.5 rad/s^2
Power Consumption	15 W
Battery Life	$\sim$ 1.5 hr

Table 2.1: SPHERES satellite properties

Three different programs (Mass Property Identification, Autonomous Rendezvous and Docking, and TPF Multiple Spacecraft Formation Flight) are currently scheduled for testing onboard the ISS in the first flight. Additional three programs (Precision Optical Pointing, Tethered Formation Flight, and Mars Orbit Sample Retrieval) have been proposed for a re-flight mission. On April 24th, 2006, Russian spacecraft Progress 21P carried one SPHERES Satellite to the International Space Station. Currently, the first test session concentrates on tests which demonstrate both single-satellite control as well as initial formation flight and docking algorithm development using a SPHERES metrology beacon as the reference.

2.1.2 SPHERES Metrology System and Limitations

The SPHERES Position and Attitude Determination System (PADS) provides real-time metrology information to each satellite. In order to provide real time state (position, velocity, attitude, angular rate) information to each Sphere, the PADS takes two different forms of measurements: the measurements from the global metrology system and the measurements from the inertial measurement units.

The PADS global metrology system performs a function similar to that of the Global Positioning System (GPS), by providing measurements of each Sphere state with respect to the global (testbed) reference frame. Five external ultrasonic beacons are mounted at known locations in the global reference frame (Figure 2-3), and the ultrasound time-of-flight measurements from the external ultrasound beacons to each Sphere are used to determine the position and attitude of each Sphere with respect to the global reference frame.

Another set of measurements comes from the inertial measurement units (IMUs), which consist of accelerometers and rate gyroscopes mounted on each Sphere. An extended Kalman filter uses both the high rate IMU data (~1 kHz) and the low-rate global data (~5 Hz) to obtain state vector of each Sphere in real-time. Detailed description of the SPHERES PADS can be found in [22].

The SPHERES PADS provides metrology resolution of ~1.0 cm in translation and $\sim \pm 1^\circ$ in rotation. While this metrology resolution is suitable for many missions such as docking, interferometry missions such as the Terrestrial Planet Finder Formation Flying Interferometer (TPF-FFI) typically require more accurate metrology resolution (TPF-FFI requires 50-75 milli-arcseconds angular resolution for the baseline range of 40-100 m [25]). In order to achieve finer level of pointing accuracy, the Precision Pointing Optical Payload (PPOP) has been developed, which is the focus of Chapters 2 through 4.

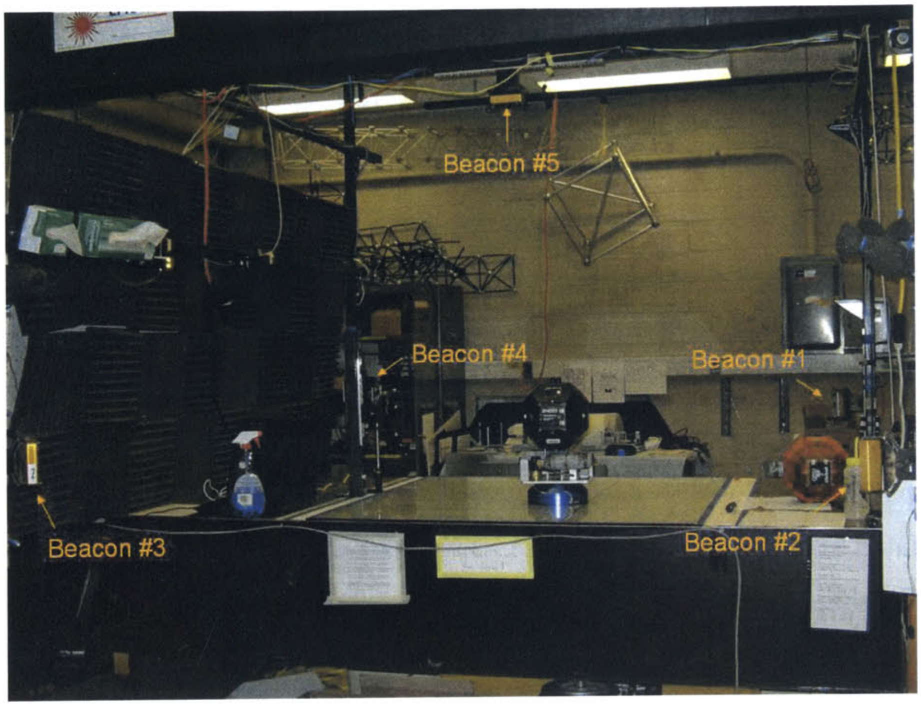

Figure 2-3: SPHERES testbed at MIT-SSL

2.1.3 SPHERES Expansion Port

Each Sphere has two flat panels on opposite sides that can be used to attach external payloads. One side provides a passive mechanical mounting points where external payloads that do not need any connections to the SPHERES internal electronics can be attached. The other side, named the SPHERES Expansion Port, provides both mechanical and electrical connections between an external payload and a Sphere. The Expansion Port provides four 2-56 screws attachment points for the mechanical connection. And the electrical connection is made through a single 100-pin connector that carries power and control signals to/from the SPHERES internal electronics [33]. The Spheres provide each external payload with power, communications, and necessary data handling, acting as the mothership to the external payloads. Figure 2-4 shows a picture of the SPHERES Expansion Port.

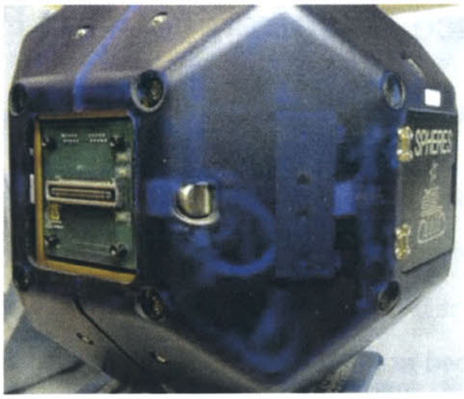

Figure 2-4: SPHERES Expansion Port

Several external payloads have been developed and successfully tested at the MIT-SSL. Two such payloads are the Universal Docking Port [32] and the Tether Formation Flight Payload [16] shown in Figure 2-5. Inheriting the experiences learned from the previous and currently ongoing projects, the Precision Pointing Optical Payload also utilizes the SPHERES Expansion Port for mechanical mounting, power, and data communication.

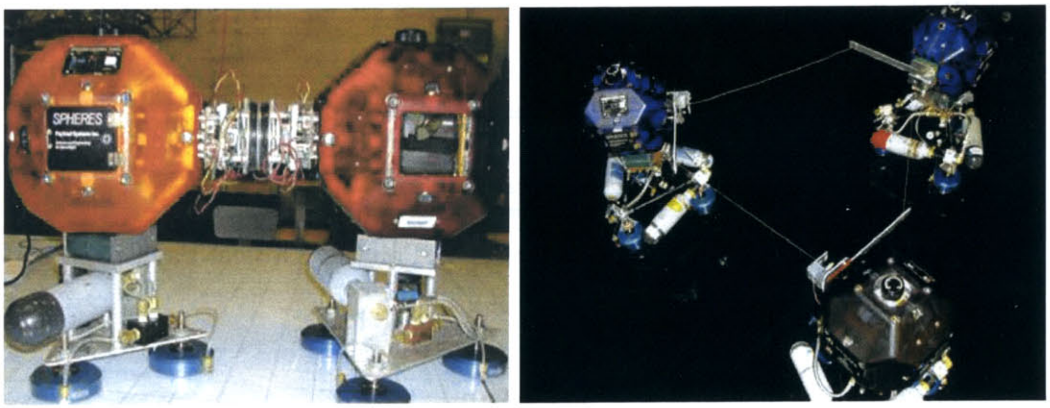

Figure 2-5: Example of external payloads: (Left) SPHERES Docking Payload (Right) SPHERES Tether Payload

2.2 Performance Requirements for Precision Pointing Optical Payload

As previously mentioned, the SPHERES PADS composed of the ultrasound metrology system and the inertial measurement units provides the metrology resolution of ~ 1.0 cm in translation and $\sim \pm 1°$ in rotation. The Precision Pointing Optical Payload (PPOP) has been developed at the MIT-SSL to overcome the metrology limitations posed by the SPHERES PADS, and to provide finer level of metrology accuracy suitable for interferometry missions such as the TPF-FFI. The current work focuses on improving the accuracy of the attitude metrology, with the goal of maintaining precision pointing between multiple Spheres.

In a mission, the SPHERES PADS can be initially used for coarse attitude control. Once Spheres are brought within ±1° from the target attitude, precision pointing control can take over and fine tune the attitudes of the Spheres, thus forming a multi-staged control. In order to realize a multi-staged control, the Field of View (FOV) requirement of the PPOP has been set to 3°, allowing 1° overlap with the angular resolution of the SPHERES PADS. Also, the operating range requirement has been set to 0.1 m - 0.5 m for the laboratory demonstration of precision pointing control. Table 2.2 lists the performance requirements set for the PPOP.

FOV	3°
Range	0.1 m to 0.5 m

Table 2.2: Requirements for the Precision Pointing Optical Payload

2.3 Precision Pointing Control Concepts

The basic concept of precision pointing control is illustrated in Figure 2-6. The Precision Pointing Optical Payload (PPOP) consists of a laser source pointed at a fast steering mirror (FSM) assembly, which in turn directs the laser beam to a beam-splitter. The beam-splitter then reflects some portion of the beam to a retro-reflector, which would then be reflected back to the beam-splitter. This time, however, it is the transmitted beam that will be detected by a CCD-based camera. Using the camera as a sensor, precision pointing can be achieved by directing the beam using the FSM. Each Sphere will be equipped with identical PPOP through the SPHERES Expansion Port, providing a modular testbed for precision pointing control experiments.

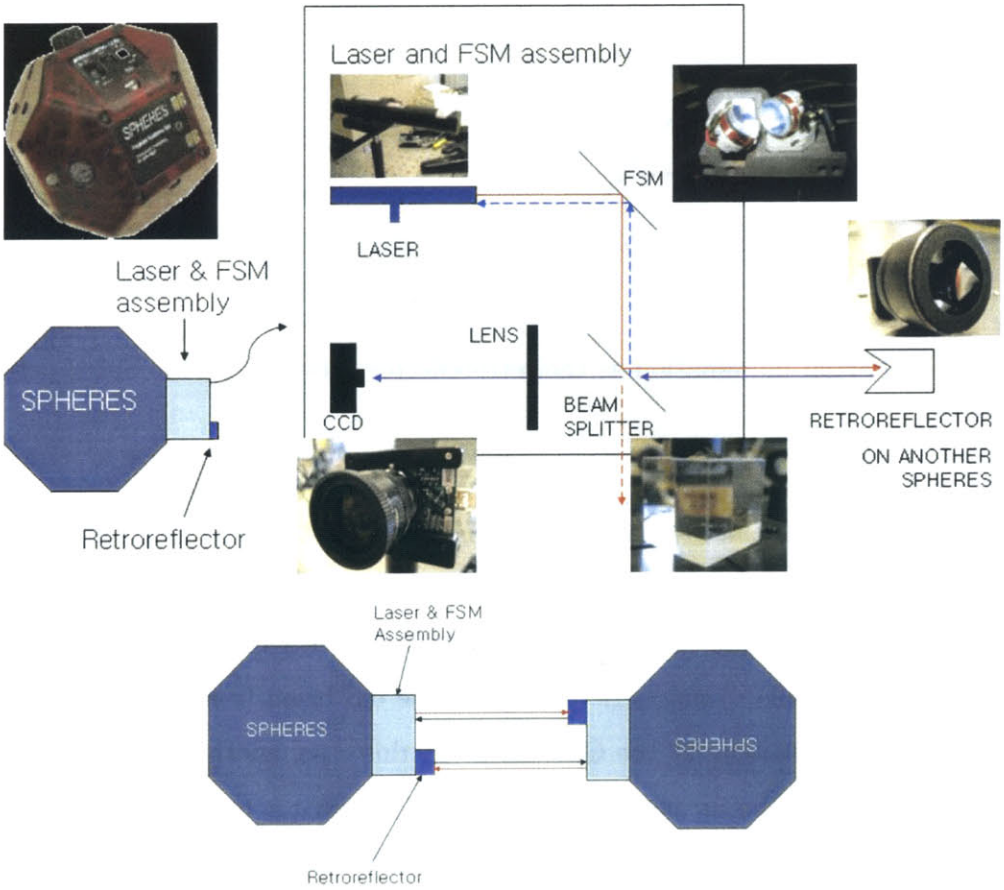

Figure 2-6: Precision Pointing Control Concept

Several different approaches can be made based on the basic concept just described. One can illuminate the aperture of the retroreflector mounted on another Sphere either partially using a collimated beam or fully using a diverging beam. The Sub Aperture Metrology (SAM) refers to the former, whereas the Full Aperture Metrology (FAM) refers to the latter. Also, combining the SAM and the FAM provides another alternative, which is named as the Hybrid Metrology (HM). Each of these approaches is described in the following sections.

2.3.1 Sub Aperture Metrology

The Sub Aperture Metrology (SAM) uses a collimated beam and illuminates the retroreflector only partially as shown in Figure 2-7.

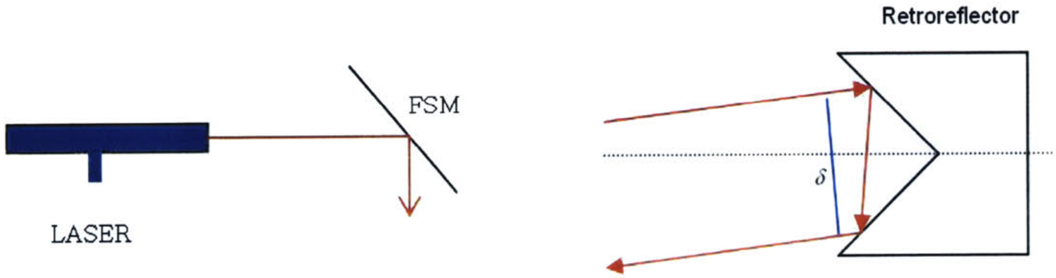

Figure 2-7: Partial illumination at the retroreflector provided by the Sub Aperture Metrology

One advantage of the SAM is that the SAM does not lose as much intensity as the FAM does since all the beams going into the retroreflector get reflected back. However, there is a beam ambiguity issue associated with the SAM. For example, one would not be able to uniquely distinguish the red beam from the blue beam in Figure 2-8 just by looking at the CCD data. In this case, another source is needed to uniquely identify the incoming beam. One such source is the voltage input data for the FSM assembly from which the angle of the incoming beam can be obtained. However, this increases the computational cost.

When using the SAM, one must take the offset caused by the retroreflector into account. If the offset is too large, the beam will not get focused onto the CCD-based camera. This limits the size of the effective aperture of the retroreflector; that is, one may implement a large retroreflector, but only small subsection of the retroreflector will actually be used, wasting the rest of the unused section of the retroreflector. To realize a compact design, the aperture size of the retroreflector should be chosen such that the size of the effective aperture where the laser beam is expected to hit is equal to or slightly less than the actual aperture size of the retroreflector.

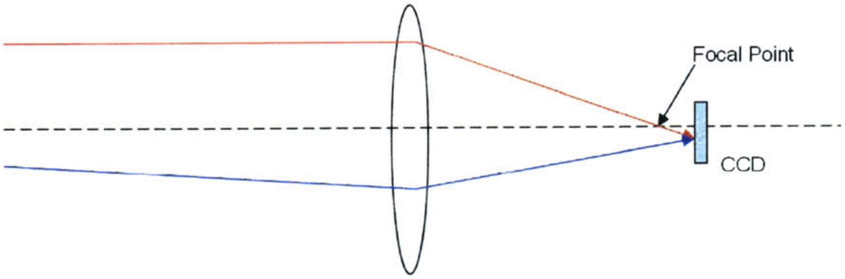

Figure 2-8: Beam ambiguity in the SAM: two beams with different incoming angles produce identical images on the CCD

2.3.2 Full Aperture Metrology

Instead of illuminating the retroreflector partially using the SAM, one can alternatively illuminate the retroreflector fully using the Full Aperture Metrology (FAM). Unlike the SAM, the FAM uses multiple retroreflectors and a diverging beam which illuminates the retroreflectors fully as shown in Figure 2-9.

One would see multiple dots on the CCD instead of a single dot for the FAM case. Using the relative distances between the dots on the CCD, one can remove the beam ambiguity issue seen in the SAM without using any other source but the CCD. Also using a diverging beam ensures that the returning beam from the retroreflectors get focused onto the CCD, making the offset issue seen in the SAM less importance for the FAM case. However, since not all the portions of the beam going into the retroreflectors get reflected back in the FAM case, the FAM loses a significant amount of intensity as the beam propagates. Also, since the FAM uses a diverging beam, the FAM alone is not appropriate for path length control, (a possible future extension of precision pointing control), which requires multiple collimated beams interfering with one another (Figure 6-1). One solution to this problem is to use both the SAM and the FAM together as described in the following section.

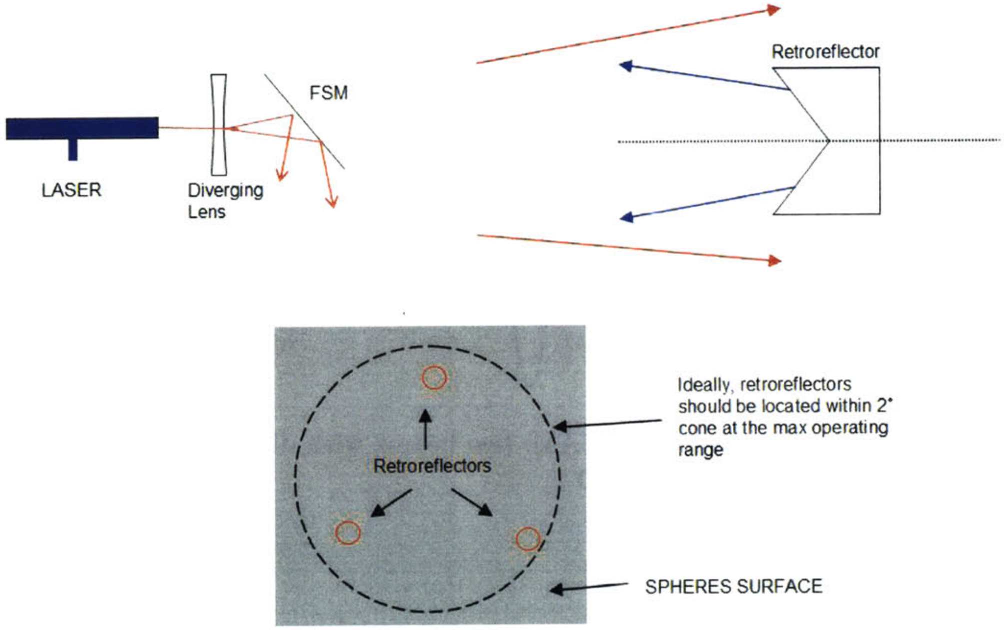

Figure 2-9: Full illumination at the retroreflector provided by the Full Aperture Metrology

2.3.3 Hybrid Metrology

One way to eliminate the limitations present in the SAM and the FAM is to combine both configurations together. The Hybrid Metrology (HM) combines the SAM and the FAM together in the hopes of eliminating the limitations posed by the SAM and FAM. The HM concept is shown in Figure 2-10.

In the HM, two different laser sources are used: a green laser for the SAM and a red laser for the FAM. The green laser beam stays collimated and performs the role of the SAM which can be used for producing interference fringes for path length control. The red laser beam diverges and performs the role of the FAM which can be used for performing precision pointing control. By combining the SAM and FAM together, the HM has the potential to eliminate the offset limitation seen in the SAM and the path length control limitation seen in the FAM. However, using multiple laser sources and multiple retroreflectors considerably increase the overall dimension of the PPOP, which is not desirable given the tight spacing available on the expansion port of the SPHERES satellite.

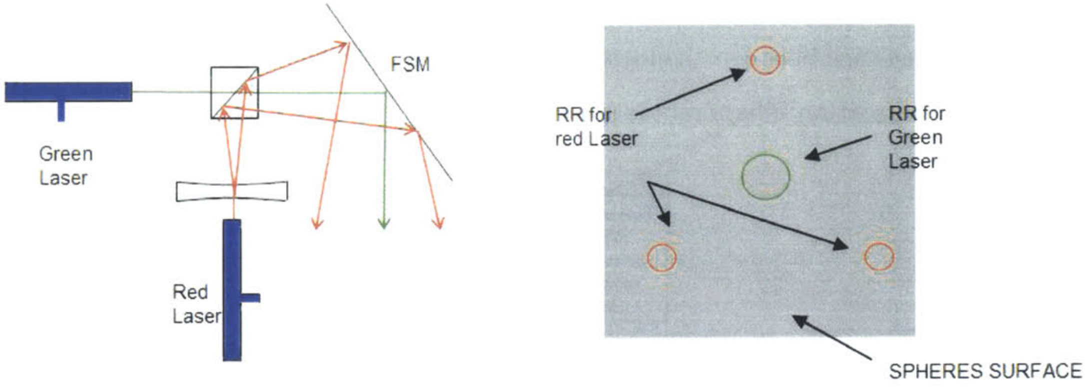

Figure 2-10: Hybrid Metrology

2.4 Ray Tracing Analysis

Mainly due to its compact design and simplicity, the SAM was chosen as the desired metrology for the first prototype development of the PPOP. In this section, a basic ray tracing analysis for the SAM is presented. Geometrical optics with paraxial approximations (Section 2.4.1) was used throughout the analysis. Effects of aberrations and diffraction were not considered in the analysis for simplicity. The following sections describe the expressions obtained for calculating the beam positions at various locations in the optical train of the PPOP.

2.4.1 Preliminaries

Paraxial Approximations

In geometrical optics, the paraxial approximations described in the following are used.

The paraxial approximations uses 1^{st} order Taylor approximations:

$\sin\varepsilon \approx \varepsilon \approx \tan\varepsilon \qquad \cos\varepsilon \approx 1 \; \sqrt{1+\varepsilon} \approx 1 + \frac{1}{2}\varepsilon$

where ε is the angle between a ray and the optical axis.

Also, the distance between the location of the axial ray intersection and the actual off-axis ray intersection is ignored as shown in Figure 2-11.

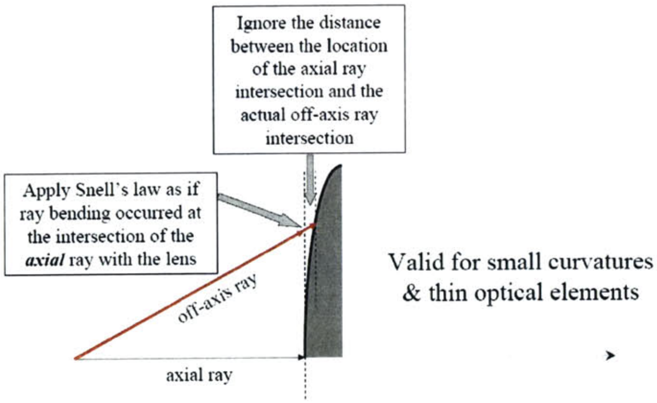

Ignore the distance between the location of the axial ray intersection and the actual off-axis ray intersection

Apply Snell's law as if ray bending occurred at the intersection of the ***axial*** ray with the lens

Valid for small curvatures & thin optical elements

Figure 2-11: Paraxial approximation (Source: MIT 2.710 OpenCourseWare)

Sign Convention

Figure 2-12 shows the sign convention used in the ray tracing analysis. Note that the positive axes of rotation for the two mirrors in the FSM assembly are denoted by green arrows. The mirrors are termed as "Mirror 1" and "Mirror 2" in the order as the ray passes through for clarity purposes. The origin of the XYZ axes coincide with the center of the beam splitter.

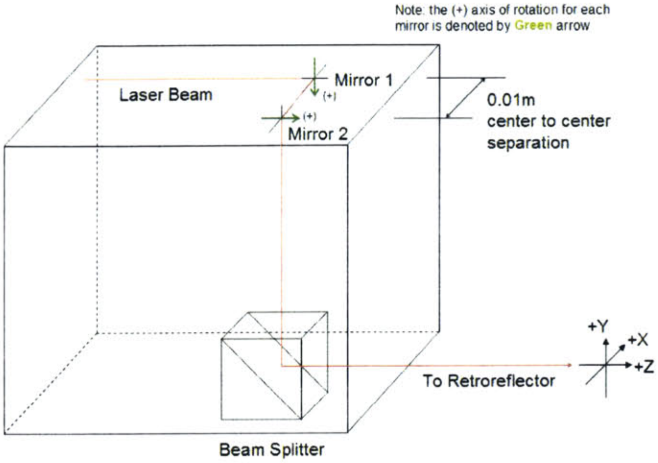

Figure 2-12: Sign convention used in the ray tracing analysis

Basic Mirror Mechanism

Figure 2-13 illustrates how beams get reflected at the mirror. Note that the angle of the reflected beam is twice the mirror actuation angle. Therefore, one must make sure that the angular range of the mirror is at least half of the required outgoing beam angular range in order to meet the field of view requirement.

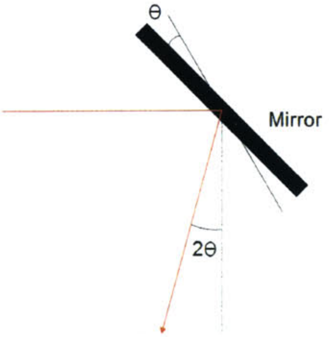

Figure 2-13: Beam gets reflected by 2θ upon the actuation of mirror by θ

2.4.2 Mirror 1 Actuation: Vertical Beam Control

Mirror 1 (M1) and Mirror 2 (M2) in the FSM assembly provide independent beam controls in the vertical (Y direction in Figure 2-12) and the horizontal (X direction in Figure 2-12) direction. Mirror 1 controls the beam position in the vertical direction whereas Mirror 2 controls the beam position in the horizontal direction. The beam location on the XY plane can be obtained by combining the effects of the actuation of Mirror 1 and Mirror 2 together. Section 2.4.2 focuses on the beam control in the vertical direction through Mirror 1 actuation by θ_{m1} as shown in Figure 2-14. The effects of Mirror 2 actuation are given in Section 2.4.3.

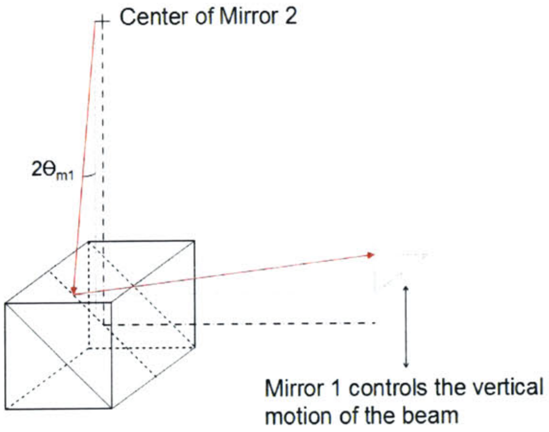

Figure 2-14: Vertical beam control by Mirror 1

M1: Mirror 2 to Beam Splitter

When M1 is rotated by $+\theta_{m1}$, the beam hits the top face of the beam splitter at the location defined by the following expression:

$$(0.01 + h) \tan 2\theta_{m1} \tag{2.1}$$

where h is the distance between the center of Mirror 2 and the top face of the beam splitter (See Figure 2-15). Note that '0.01' in Equation (2.1) denotes the physical separation distance between M1 and M2 in meters.

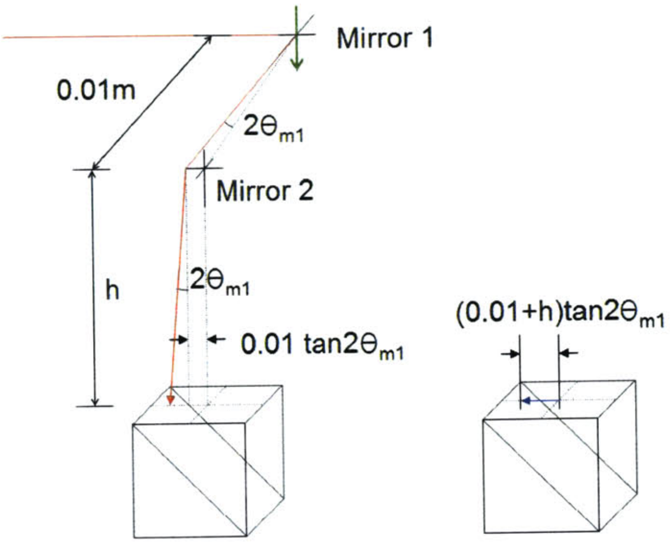

Figure 2-15: Determining the location of the beam on the beam splitter - Mirror 1

M1: Beam Splitter to Retroreflector

Figure 2-16 shows the detailed ray tracing analysis through the beam splitter. In order to simplify the expressions, variable k was defined to be the length traveled by the refracted beam inside the beam splitter before it hits the 45° slanted surface. k is denoted by the blue line in Figure 2-16.

k can be obtained using the following equation.

$$k = \frac{\frac{d}{2} - (h + 0.01)\tan 2\theta_{m1}}{\sin(45^\circ + \theta_{g1})} \sin(45^\circ) \tag{2.2}$$

where θ_{g1} can be obtained using the Snell's law:

$$\theta_{g1} = \sin^{-1}\left(\frac{\sin 2\theta_{m1}}{n_{BS}}\right) \tag{2.3}$$

Here, n_{BS} is the index of refraction for the beam splitter, which is approximately equal to 1.5. The vertical displacement v from the center of the beam splitter at range R can be obtained using Equation (2.4).

$$v = \frac{d}{2} - k\cos\theta_{g1} + (d - k\cos\theta_{g1})\tan\theta_{g1} + R\tan 2\theta_{m1} \tag{2.4}$$

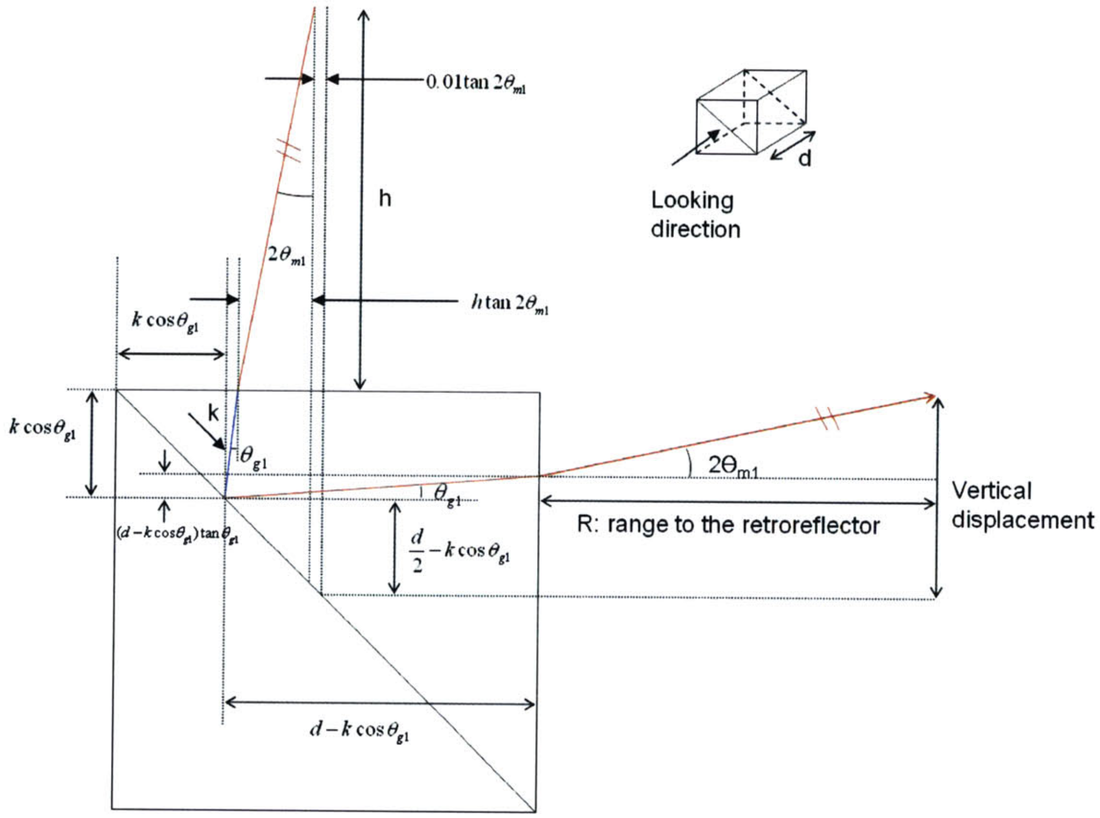

Figure 2-16: Ray tracing through the beam splitter - Mirror 1

Equation (2.4) can be used to appropriately choose the size of the retroreflector. In order to make sure that the beam hits the retroreflector, one must make sure that half of the size of the retroreflector aperture should be larger than the vertical displacement created by M1 at range R, assuming that the retroreflector and the beam splitter are located on the same plane with their centers passing through the same axis. Note that range is defined as the distance between the beam splitter face towards the retroreflector to the entrance aperture of the retroreflector, not to the actual fold mirrors that consist of the retroreflector.

Retroreflector Offset

The expressions for obtaining the offset created by the retroreflector are described in the following. Two parameters, p and q, are defined as shown in Figure 2-17.

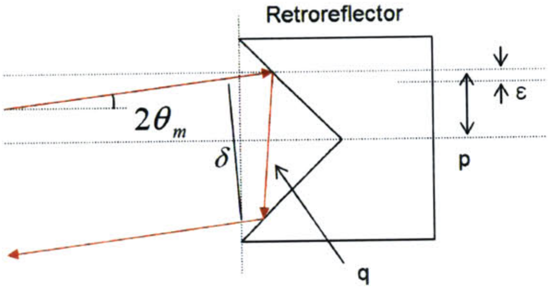

Figure 2-17: Offset created by retroreflector

The incoming beam angle is $2\theta_m$, twice the mirror actuation angle. Assuming that the incoming and the outgoing beams are parallel, the offset created by the retroreflector, δ, can be calculated using the following expressions:

$$\epsilon = \left(\frac{1}{2}D_{RR} - |R|\right)\left(1 - \frac{1}{1 + \tan 2|\theta_m|}\right) \tag{2.5}$$

$$p = |R| + \epsilon \tag{2.6}$$

$$q = \frac{2p}{\sin(45^\circ - 2|\theta_m|)} \sin 135^\circ \tag{2.7}$$

$$\delta = q \sin(90^\circ - 4|\theta_m|) \tag{2.8}$$

where D_{RR} is the diameter of the retroreflector aperture.

These expressions are valid for both Mirror 1 and Mirror 2 actuations.

M1: Exiting Beam Splitter towards Focusing Lens

As the returning beam from the retroreflector gets refracted at the beam splitter surface and propagates through the beam splitter, the beam encounters further displacements. Therefore, one must make sure that the beam coming from the retroreflector not only enters, but also exits the beam splitter successfully. If the beam fails to either enter or exit the beam splitter successfully, then one must use either a bigger beam splitter or reduce offset created by the retroreflector. S_1 is defined as in Figure 2-18, and the vertical location of the beam on the exiting beam splitter face towards the focusing lens can be calculated as following.

$$S_1 = \frac{\delta_1}{\cos 2\theta_{m1}} \frac{|\theta_{m1}|}{\theta_{m1}} \tag{2.9}$$

$$v_{to\_lens} = \frac{d}{2} - k\cos\theta_{g1} - k\cos\theta_{g1}\tan\theta_{g1} - S_1 \tag{2.10}$$

Note that the outgoing angle of the beam is $2\theta_{m1}$ and the positive θ_{m1} produces negative v_{to_lens}.

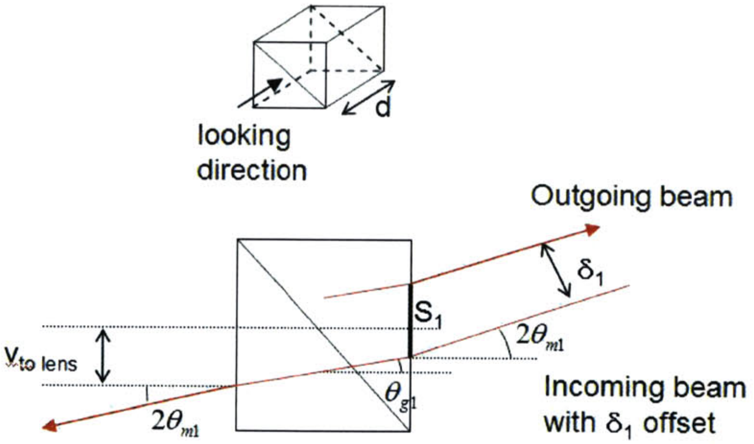

Figure 2-18: Vertical location of the beam on the beam splitter face towards the focusing lens

Going Through the Lens

The thick lens formula given in Equation (2.11) and Equation (2.12) are used to obtain the angle and the location of the beam coming out of the focusing lens. These expressions are valid for both Mirror 1 and Mirror 2 actuations. The notations used in the thick lens formula are given in Figure 2-19.

$$\alpha_{out} = \left(1 + \frac{n-1}{n}\frac{d}{R'}\right)\alpha_{in} - \left[(n-1)\left(\frac{1}{R} - \frac{1}{R'}\right) + \frac{(n-1)^2 d}{nRR'}\right] y_{in} \tag{2.11}$$

$$y_{out} = \frac{d}{n}\alpha_{in} + \left(1 - \frac{n-1}{n}\frac{d}{R}\right) y_{in} \tag{2.12}$$

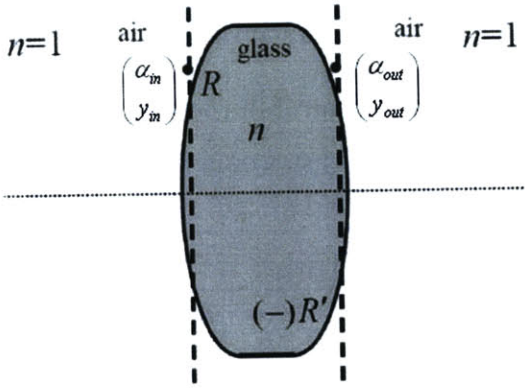

Figure 2-19: Notations used in the thick lens formula

Note that positive θ_{m1} produces negative α_{in} and y_{in} as illustrated in the following expressions. $d_{BS-lens}$ denotes the separation distance between the beam splitter and the focusing lens.

$$\alpha_{in} = -2\theta_{m1} \tag{2.13}$$

$$y_{in} = v_{to\ lens} + d_{BS-lens} \tan 2\theta_{m1} \tag{2.14}$$

Focusing onto CCD

Once α_{out} and y_{out} are obtained using Equation (2.11) and Equation (2.12), the vertical location of the beam on the CCD-based camera, y_{CCD}, can be calculated as following. $d_{lens-CCD}$ denotes the separation distance between the focusing lens and the CCD-based Camera.

$$y_{CCD} = y_{out} + d_{lens-CCD} \tan \alpha_{out} \tag{2.15}$$

In order to successfully focus the beam onto CCD, one would have to design the optical train such that y_{CCD} is less than half of the vertical dimension of the CCD sensor.

2.4.3 Mirror 2 Actuation: Horizontal Beam Control

Mirror 2 (M2) provides the beam control in the horizontal direction (X direction in Figure 2-12) when actuated by θ_{m2} as shown in Figure 2-20.

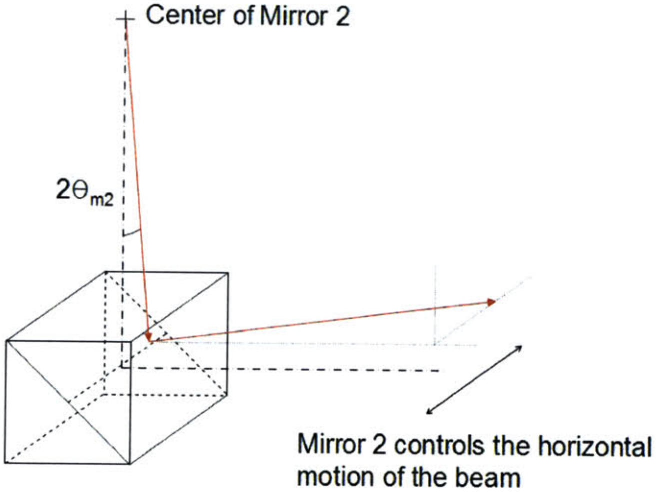

Figure 2-20: Horizontal beam control by Mirror 2

A ray tracing analysis similar to the one given in the previous section for the Mirror 1 actuation was performed for the Mirror 2 actuation in this section. The resulting ray tracing expressions for the key locations in the optical train are given in the following. Note that the retroreflector offset calculation formulae given in Equation (5.4) - (2.8) and the thick lens formulae given in Equation (2.11) - (2.12) also apply to the Mirror 2 actuation case, and therefore, those equivalent expressions for the Mirror 2 case have not been included in this section.

M2: Mirror 2 to Beam Splitter

When Mirror 2 is rotated by $+\theta_{m2}$, the beam hits the top face of the beam splitter at the location defined by the following expression:

$$h \tan 2\theta_{m2} \tag{2.16}$$

Figure 2-21 illustrates the propagation of the beam from the center of Mirror 2 to the top face of the beam splitter.

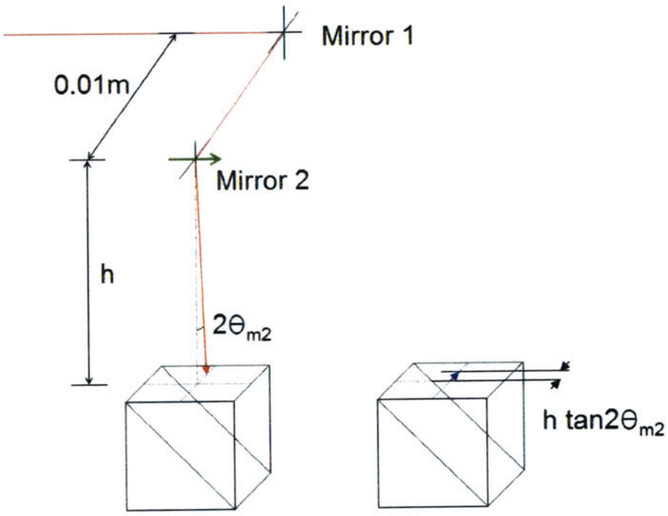

Figure 2-21: Mirror 2 actuated by θ_{m2}

M2: Beam Splitter to Retroreflector

Similarly to the Mirror 1 case, the horizontal displacement *hor* from the center of the beam splitter at range R can be obtained using Equation (2.17).

$$hor = h \tan 2\theta_{m2} + d \tan \theta_{g2} + R \tan 2\theta_{m2} \tag{2.17}$$

where θ_{g2} can be obtained, once again, using the Snell's law:

$$\theta_{g2} = \sin^{-1}\left(\frac{\sin 2\theta_{m2}}{n_{BS}}\right) \tag{2.18}$$

A detailed ray tracing analysis for the beam propagating in the beam splitter towards the retroreflector is illustrated in Figure 2-22.

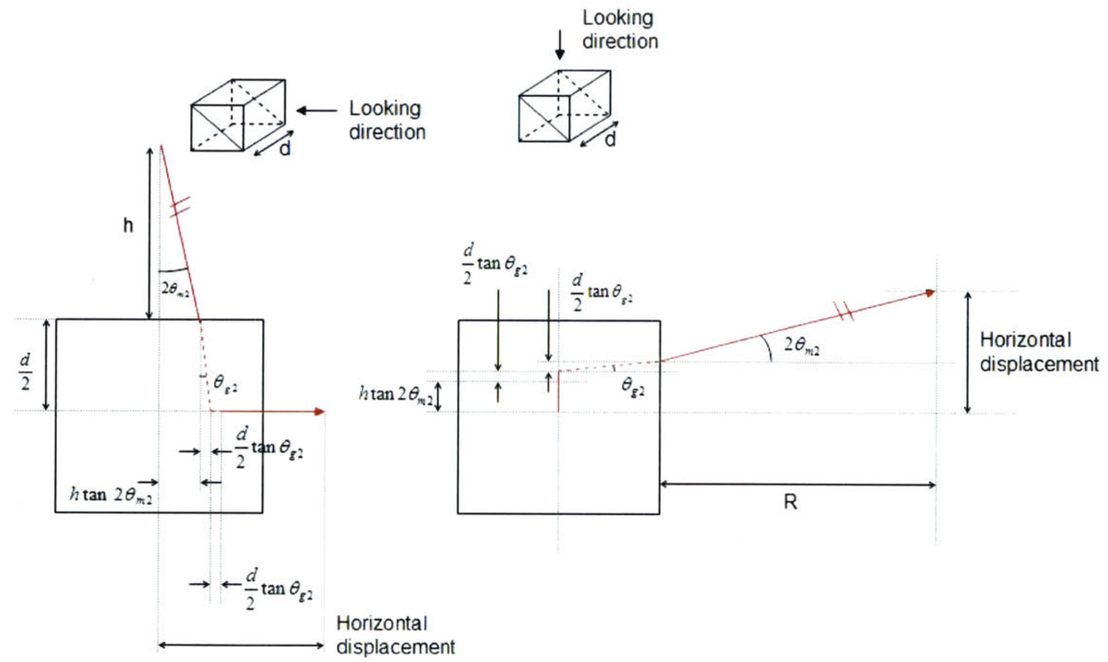

Figure 2-22: Ray tracing through beam splitter - Mirror 2

M2: Exiting Beam Splitter towards Focusing Lens

S_2 is defined as in Figure 2-23 and the horizontal location of the beam on the beam splitter face towards the focusing lens can be calculated as following:

$$S_2 = \frac{\delta_2}{\cos 2\theta_{m2}} \frac{|\theta_{m2}|}{\theta_{m2}} \tag{2.19}$$

$$h_{to\_lens} = h \tan 2\theta_{m2} - S_2 \tag{2.20}$$

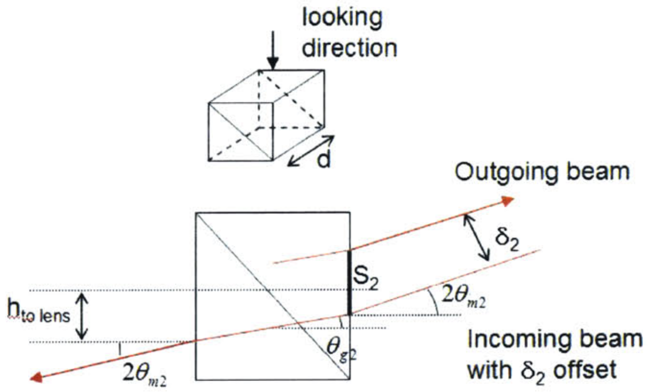

Figure 2-23: Horizontal beam location on the beam splitter face towards the focusing lens

Focusing onto CCD

Equation (2.5) - (2.8) and Equation (2.11) - (2.12) can also be used for the case with Mirror 2. Following the similar steps as in the Mirror 1 case, the horizontal location of the beam on CCD, x_{CCD}, can be calculated as the following.

$$x_{CCD} = x_{out} + d_{lens-CCD} \tan \alpha_{out} \tag{2.21}$$

Once again, x_{CCD} should be less than half of the horizontal dimension of the CCD sensor in order to successfully focus the beam onto the camera.

2.5 Concept Downselection and Modification

This section presents the performance prediction for the Sub Aperture Metrology (SAM) obtained through the ray tracing analysis described in the previous section. The performance prediction results were used to determine the feasibility of the SAM concept for a prototype development. This section concludes with a description of the final concept chosen for a prototype development.

2.5.1 Performance Prediction and Experimental Validation of Ray Tracing Analysis

Using MATLAB, a technical computing language, the expressions derived in the ray tracing analysis were put into a custom code (Appendix C). Different sets of commercially available beam splitters, retroreflectors, and focusing lens were tested for various operating ranges. For each test case, the maximum mirror actuation angles that allow successful image acquisition on the CCD were obtained. Table 2.3 shows some of the results given by the MATLAB code.

	Range (m)	Beam Splitter Side Length (m)	Retroreflector Diameter (m)	Θ_{min} (deg)	Θ_{max} (deg)
Mirror 1	0.25	0.254	0.254	-0.38	+0.38
Mirror 2				-0.52	+0.52
Mirror 1	0.4	0.254	0.254	-0.21	+0.21
Mirror 2				-0.28	+0.28
Mirror 1	0.5	0.254	0.254	-0.16	+0.16
Mirror 2				-0.22	+0.22

Table 2.3: Predicted results from MATLAB ray tracing code

A simple experiment was performed on an optics table (see Figure 2-24) in the MIT-SSL in order to provide a rough check on the MATLAB code.

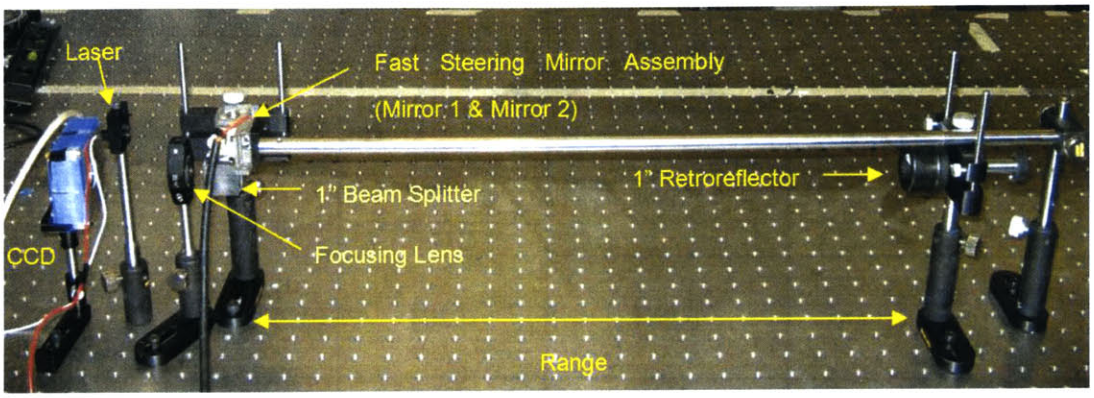

Figure 2-24: Experimental setup for MATLAB ray tracing code validation

Table 2.4 describes the experimental setup. The exact specifications for the focusing lens used were not available when the experiment was performed and the lens parameters were measured carefully with a caliper (Table 2.5). Note that the values in Table 2.4 and Table 2.5 were also used in the MATLAB code when the results in Table 2.3 were generated. The experimental results are listed in Table 2.6.

	Mirror 2 to Beam Splitter (mm)	Beam Splitter to Lens (mm)	Lens to CCD (mm)
Setup Configuration	13	15	80

Table 2.4: Experimental setup configuration

Aperture Diameter (mm)	Back Focal Length (mm)	Center Thickness (mm)	Edge Thickness (mm)
25.4	60	4	2

Table 2.5: Estimated lens parameters

	Range (m)	Beam Splitter Side Length (m)	Retroreflector Diameter (m)	Θ_{min} (deg)	Θ_{max} (deg)
Mirror 1	0.25	0.254	0.254	-0.3298	+0.3298
Mirror 2				-0.4507	+0.4507
Mirror 1	0.4	0.254	0.254	-0.2178	+0.2178
Mirror 2				-0.3025	+0.3025
Mirror 1	0.5	0.254	0.254	-0.1603	+0.1603
Mirror 2				-0.2405	+0.2405

Table 2.6: Experimental results for MATLAB ray tracing code validation

The experimental results given in Table 2.6 agree with the theoretical results provided by the MATLAB ray tracing code with marginal errors. The average percentage error between the experimental results and the theoretical results turned out to be $\sim$ 8%. Considering the possible sources of error such as the misalignment error and the numerical error from the paraxial approximations, it was inferred that the MATLAB produces correct results.

2.5.2 Concept Modification for Prototype Development

In order to achieve the performance requirements given in Table 2.2, the mirrors should be able to actuate at least 1.5° (±0.75°) at the operating range of 0.5 m while still focusing the beam onto the CCD successfully. However, both the analytical and the experimental results shown in the previous section suggest that the requirements cannot be met with the SAM. Besides, the ray tracing analysis was developed assuming a perfect alignment between the beam splitter and the retroreflector. Both the angular and the translational misalignments will make the performance even worse according to the equations given in the Appendix A.

In order to meet the performance requirements, one can use a bigger beam splitter and a bigger lens with more focusing power. One can also use an array of tiny retroreflectors, which would effectively reduce the offset magnitude caused by the retroreflector. However, due to the limitations posed by both the allowable package dimension and the budget, using more sophisticated components was not a feasible option for the first prototype development. Instead, a slight modification was made on the original SAM concept in order to achieve the performance requirements. Figure 2-25 shows the modified concept.

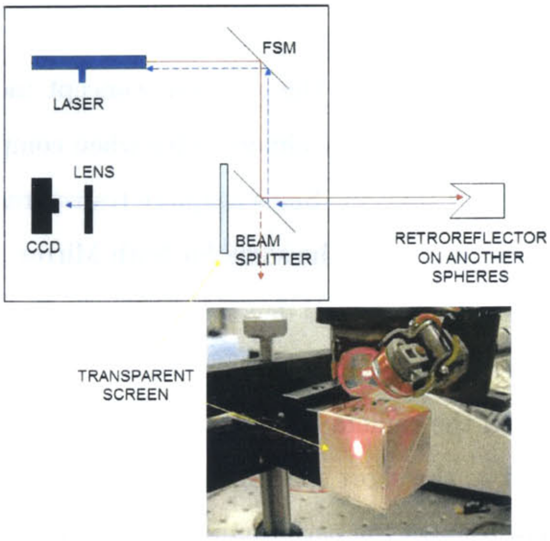

Figure 2-25: Modified concept chosen for prototype development

Instead of focusing the beam directly onto the CCD, the modified concept uses a transparent screen, and the image of the beam on the screen is used for precision pointing control. The modified concept still has to consider the effects of the retroreflector offset. However, the CCD captures the beam as long as the beam makes it to the beam splitter face towards the lens. This eliminates the deviation of the beam that takes place between the beam splitter and the lens, and therefore improves the performance. Table 2.7 shows the results from a simple experiment performed to predict the performance of the modified concept for the range of 0.5 m. Same test setup shown in Figure 2-24 was used and the maximum mirror actuation angles that allow successful image acquisition on the CCD were obtained.

	Range (m)	Beam Splitter Side Length (m)	Retroreflector Diameter (m)	Θ_{min} (deg)	Θ_{max} (deg)
Mirror 1	0.5	0.254	0.254	-0.4213	+0.4213
Mirror 2				-0.4213	+0.4213

Table 2.7: Experimental results for allowable mirror actuation angles obtained using the modified concept

As the results in Table 2.7 show, the modified concept increases the range of the allowable mirror actuation angle by almost twice when compared with the range provided by the original SAM concept. Since a square transparent screen is used, the allowable mirror actuation angles are the same for both Mirror 1 and Mirror 2.

The modified concept was chosen and developed into the Precision Pointing Optical Payload (PPOP). As will be described in Section 3.1.5, a micro lens with a short focal length is mounted on the camera board in the PPOP. The wide FOV provided by the micro lens as well as the short spacing between the micro lens and the CCD sensor enables the PPOP to meet the performance requirements given in Table 2.2. It should be noted that the modified concept cannot be used to do path length control using interference fringes. If path length control is desired in the future, one would have to use the original SAM with more sophisticated optical components.

2.6 Chapter Summary

This chapter presented a brief overview of the SPHERES testbed. The limitations of the SPHERES Position and Attitude Determination System (PADS) were explained, and the concepts for precision pointing control were introduced as the ways for overcoming the limitations. Three different concepts for precision pointing control were presented: the Sub Aperture Metrology (SAM), the Full Aperture Metrology (FAM), and the Hybrid Metrology (HM). The SAM was chosen for further analysis due to its simplicity. A ray tracing analysis was developed using geometrical optics, and was used to predict the expected performance of the SAM. Based on the results of the ray tracing analysis and the simple experiment performed on an optics table, it was determined that the SAM with direct focusing of the beam onto the CCD cannot meet the performance requirements. In order to improve the performance, the original SAM concept was modified. Instead of focusing the beam directly onto the CCD, the modified concept uses a transparent screen, and the image of the beam on the transparent screen is used for precision pointing control. The results from a simple experiment show that the modified concept improves the performance by a factor of two. Hence, the modified concept was chosen as the final concept for the Precision Pointing Optical Payload (PPOP). The next chapter describes the realization of the concept chosen into the prototype development of the PPOP.

Chapter 3

Testbed Development of Precision Pointing Optical Payload

The concept for precision pointing control described in the previous chapter was developed into a testbed called the "Precision Pointing Optical Payload (PPOP)." The optical components and the avionics implemented in the PPOP are described. A discussion of the data communication between a Sphere and the PPOP is followed. This chapter concludes with providing a snap shot of the CAD model developed as well as a picture of the actual prototype built.

3.1 Optical Components

The Precision Pointing Optical Payload (PPOP) consists of a laser, a fast steering mirror (FSM) assembly, a beam splitter, a retroreflector, a focusing lens, and a CCD-based camera. Each of the optical components used in the PPOP is described in this section.

3.1.1 Laser

The precision pointing control concept chosen requires the beam to be collimated and to have a moderate power at the same time. HLM-635-02LPA laser module shown in

Figure 3-1 was chosen as the source of the beam for the optical payload.

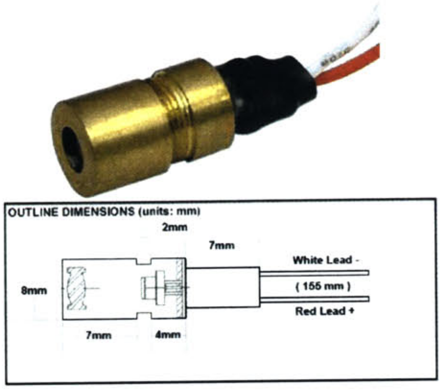

Figure 3-1: HLM-635-02LPA laser module

HLM-635-02LPA laser module integrates a collimating lens, a laser diode, and a driver circuit inside a solid brass housing, and provides a bright collimated beam. The specifications for HLM-635-02LPA laser module are shown in Table 3.1.

Operating voltage	3 ∼ 5 V
Operating current	40 ± 15 mA
Cw output power	≤ 3.0 mW
Wavelength at peak emission	630 - 645 nm
Collimating lens	Aspheric Plastic (ϕ7)
Housing	Brass
Spot size at 5M	6 ± 2 mm
Divergence	1.6 mrad
Mean time to failure	5000 hrs
Operating Temp. range	+10 ∼ +40° C
Storage Temp. range	-20 ∼ +65° C

Table 3.1: HLM-635-02LPA laser module specifications

3.1.2 Fast Steering Mirror

Figure 3-2 shows the fast steering mirror (FSM) assembly used in the PPOP. The FSM assembly consists of two mirrors, which provide the control of the laser beam in both the horizontal and the vertical directions. The exact specifications for the mirrors were not available when the FSM assembly was purchased, and therefore, some of the key properties for the mirrors were experimentally obtained.

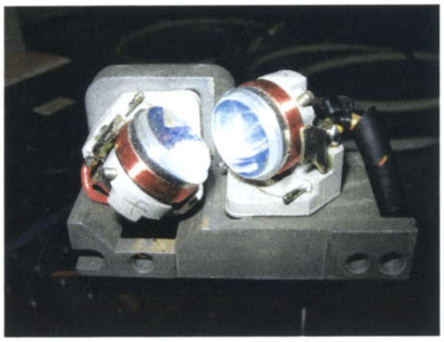

Figure 3-2: Fast steering mirror assembly used in the Precision Pointing Optical Payload

Angular Stroke Capability

The angular stroke that each of the two mirrors in the FSM assembly is capable of was experimentally determined by applying current to the mirrors. A laser beam was reflected onto a wall by the mirrors, and the deflections of the beam on the wall were recorded. The current was varied from 0 to +255 ma, and the positive current actuated the mirror in one direction. Negative current actuates the mirror in the other direction. Figure 3-3 shows the setup configuration used in the measurement. The recorded values for the beam deflection as well as the derived values for the corresponding angular stroke of the mirror are also shown in Figure 3-3.

As shown in Figure 3-3, the mirrors in the FSM assembly are capable of providing angular strokes in the range of $\sim \pm 12^\circ$ (0.0224 deg/mA), which is sufficient considering the $\sim \pm 1^\circ$ angular resolution that the SPHERES PADS provides.

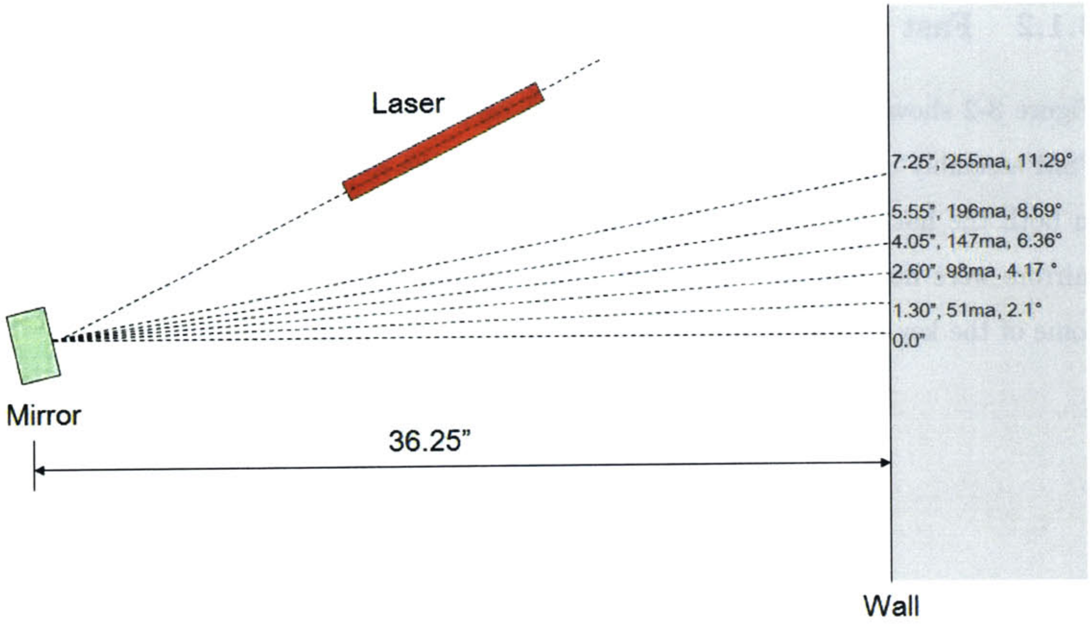

Figure 3-3: Angular stroke measurement for the fast steering mirrors

Damping and Natural Frequency Estimation

The damping coefficient and the natural frequency of the fast steering mirrors were also obtained experimentally. A load of 1.5V was initially applied to the mirror using a AA battery. Then, the load was removed by disconnecting the battery, and the mechanical vibrations of the mirror were measured as voltage fluctuations on an oscilloscope. A snap shot of the voltage fluctuations obtained on the oscilloscope is shown in Figure 3-4.

The natural frequency of the mirror (ω_n) was obtained to be ~68.97 Hz (433.32 rad/s) by measuring, and then converting the period of the voltage fluctuations. Two different approaches, the curve fitting approach and the logarithmic decrement approach, were taken to estimate the damping coefficient (ξ) of the fast steering mirrors.

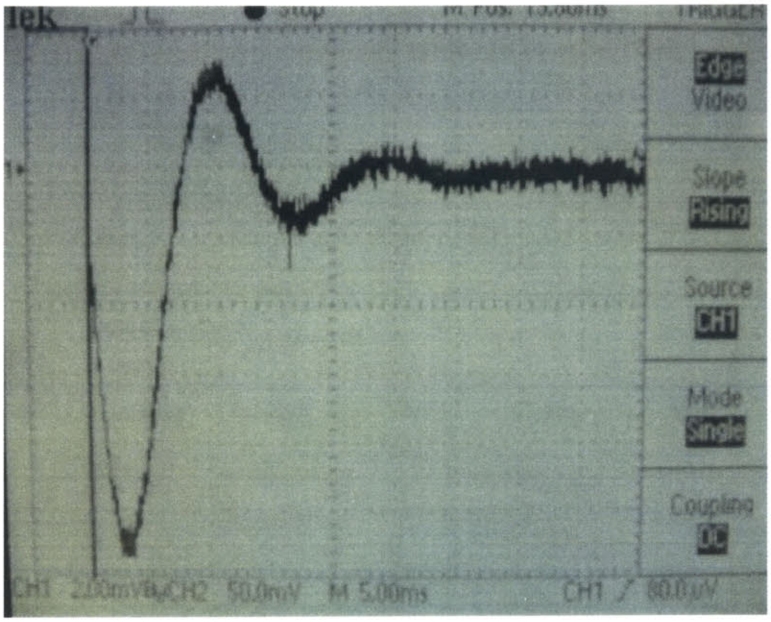

Figure 3-4: Mechanical vibration of the fast steering mirror

In the curve fitting approach, the peak points in the voltage fluctuation curve in Figure 3-4 were fitted with an exponential curve. Using the second-order approximation for the dynamics of the mirrors (Equation 3.1), the damping coefficient for the mirrors was calculated to be 0.302. Figure 3-5 shows the data points and the resulting curve fit used to obtain the damping coefficient.

$$y = Ae^{-\xi\omega_n t} \tag{3.1}$$

In the logarithmic decrement approach the amplitude of motion, x_1, at the beginning of a cycle and the amplitude, x_2, at the end of the cycle were measured. Using Equation 3.2 and 3.3, the damping coefficient was obtained to be 0.2958, which agrees with the result obtained using the curve fitting approach.

$$\delta = ln\left(\frac{x_1}{x_2}\right) \tag{3.2}$$

$$\xi = \frac{\delta}{\sqrt{(2\pi)^2 + \delta^2}} \tag{3.3}$$

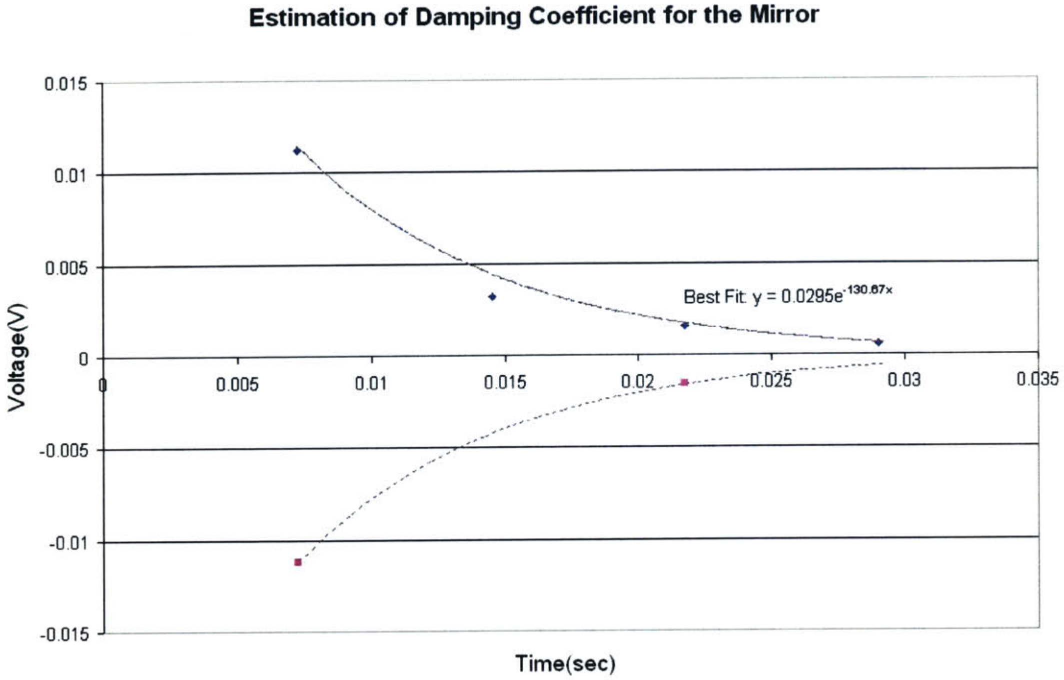

Figure 3-5: Damping estimation for the fast steering mirror using the curve fitting approach

The fast steering mirror properties are summarized in Table 3.2.

Resistance	$\sim 7.7\ \Omega$
Angular Stroke	$\sim \pm 12°$
Damping Coefficient (ξ)	$\sim$0.3
Natural Frequency	$\sim$68.97 hz (433.32 rad/s)

Table 3.2: Estimated mirror properties

3.1.3 Beam Splitter

Figure 3-6 shows the beam splitter used in the Precision Pointing Optical Payload.

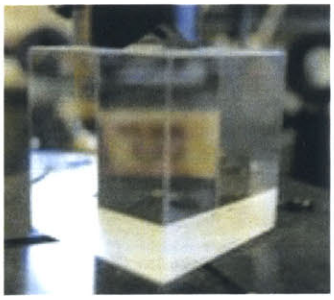

Figure 3-6: Beam splitter used in the Precision Pointing Optical Payload

A one-inch cubic 50%-50% power beam splitter is used. Every time the laser beam hits the beam splitter, 50% of the beam gets transmitted and the other 50% gets reflected. In the precision pointing control concept chosen, the laser beam hits the beam splitter twice, and the loss in the beam's intensity could be significant since the beam loses half of its intensity every time it hits the beam splitter. Therefore, one should make sure to use a powerful laser as the source of the beam in order to provide strong enough intensity at the end of the optical train. One alternative option would be to use a polarizing beam splitter instead of a power beam splitter. A polarizing beam splitter separates the laser beam into two orthogonally polarized components. The intensity of the beam gets reduced only once when the unpolarized beam first hits the beam splitter and gets polarized. However, appropriate wave plates need to be placed along the optical train to keep the polarizations of the beam proper, making the system bulky. Due to its simplicity, a 50%-50% power beam splitter was chosen for the PPOP.

3.1.4 Retroreflector

The retroreflector used in the PPOP is shown in Figure 3-7.

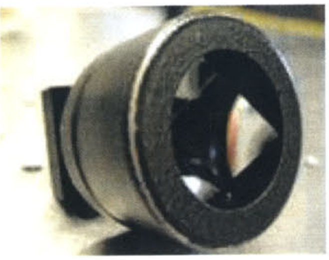

Figure 3-7: Retroreflector used in the Precision Pointing Optical Payload

The retroreflector is constructed of three surface mirrors assembled into a corner cube and has a one-inch aperture. The parallel incident light is reflected with some offset back to the light source, regardless of the angle of incidence. Depending on the angle of the incident light, undesirably large offset could be produced, and one must keep the offset small when designing an optical system. Using an array of tiny reflectors such as shown in Figure 3-8 is an alternative option, which can effectively reduce the magnitude of the offset. However, using more sophisticated components increases the budget requirement and therefore, a simple, corner cube retroreflector was chosen for the PPOP.

Figure 3-8: Array of tiny retroreflectors which could be used to reduce the retroreflector offset

3.1.5 Focusing Lens and CCD

A CCD-based digital camera was chosen as the sensor for precision pointing control. The camera contains 480x640 pixels and produces a 2D image on a grayscale of 0-255, with 255 being the brightest intensity value on the scale. As will be discussed in Section 4.1, the location of the centroid of the laser beam is determined from the intensity of each pixel. The actual centroid location and the target centroid location are compared, and appropriate control law is applied to eliminate the error between the actual and the target centroid location. A picture and the specifications of the camera can be found in Figure 3-9 and Table 3.3.

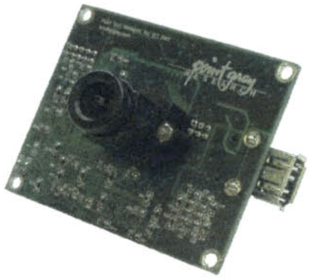

Figure 3-9: CCD-based camera used in the Precision Pointing Optical Payload with a micro focusing lens mounted on the CCD board

Point Grey Research Inc. provides micro lens with three different focal lengths for the Dragonfly camera: 4, 6, or 8 mm. The shortest possible distance between the beam splitter and the camera is desired to keep the size of the payload compact, and therefore, the micro lens with focal length of 4 mm was chosen. Note that smaller focal length implies larger FOV of the camera according to Equation (3.4) [17]. In turn, larger FOV makes the distance between the beam splitter and the camera shorter.

$$FOV = \frac{d}{f}n = 2.44\frac{\lambda}{D_{eff}}Qn \tag{3.4}$$

where n is the number of pixels along the x axis or the y axis of CCD matrix, d is the pixel size, f is the focal length, and Q is a quality factor.

Manufacturer	PointGrey
Model	Dragonfly
Imaging Device	1/3" Sony CCD
Colers	Grayscale
Resolultion	480x640
Connector	6-pin IEEE1394 (FireWire)
Dimensions	2.5" x 2"
Frame Rate	Up to 30 fps
Pixel Size	7.4μm
Focal Length	4 or 6 or 8 mm

Table 3.3: Camera specifications

3.2 Integration

This section describes the avionics used in the PPOP and its integration with the optical components described in the previous section. The data interface established between a Sphere and the PPOP through the SPHERES Expansion Port is also described.

3.2.1 UC1394a-1 Multi-Chip Module: The Brain for Precision Pointing Optical Payload

The UC1394a-1 Multi-Chip Module (MCM) purchased from Orsys acts as the brain for the PPOP. A picture of UC1394a-1 MCM is shown in Figure 3-10. As illustrated in Figure 3-11, on-board DSP, FPGA and a wide variety of serial, analog, and configurable digital I/O resources of UC1394a-1 MCM provide users with an extensive range of plug & play and software programmable capabilities for various applications including IEEE 1394 firewire applications. The key hardware features are listed in the following.

- Texas Instruments TMS320C5509 DSP Processor
- Xilinx 50kGate Spartan-II FPGA
- 8MBytes of 100MHz SDRAM, and 512kBytes of FLASH ROM
- RS-232, USB, McBSP, I2C, JTAG, integral analog to digital conversion for four analog inputs
- 27 uncomitted FPGA I/O pins for user configurable digital I/O
- Real-Time Clock (200Mhz)
- 30mm x 36mm, 116 pin PLCC footprint

Figure 3-10: Ultra compact UC1394a-1 Multi-Chip Module

Using Code Composer Studio [12], a code generation tool provided by Texas Instrument, a realtime embedded application was developed for precision pointing control. The application utilizes one IEEE1394 channel for establishing the camera interface, three General Purpose Input Output (GPIO) pins for generating appropriate input signals to the fast steering mirrors, one GPIO pin for controlling laser on/off, and the RS232 UART channel for communicating data to/from the SPHERES satellite.

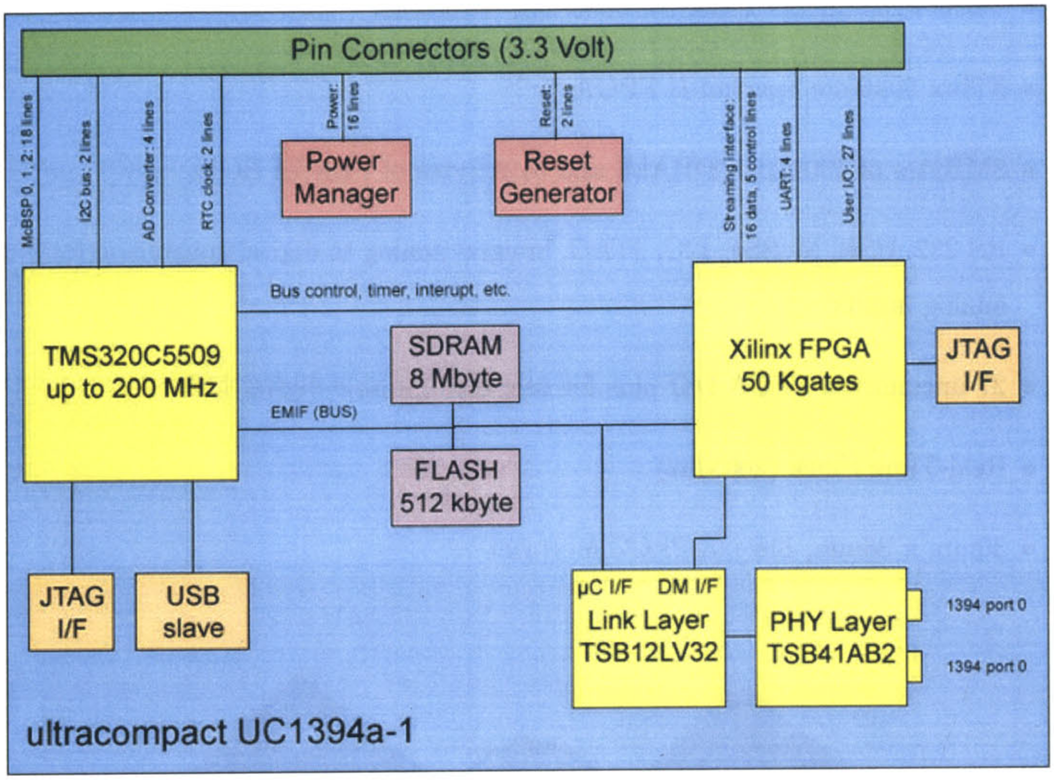

Figure 3-11: Various building blocks embedded in UC1394a-1 Multi-Chip Module [7]

When programming an application onto TMS320C5509 DSP processor, one must make sure not to exceed the 64K page limit imposed by TMS320C5509. TMS320C5509 is a 16 bit, fixed integer DSP processor and it restricts pointer manipulation to be always done modulo 64K. Since the CCD-based camera has 480x640 pixels which exceed 64K, one must use a proper cast when needed and carefully handle the intensity data stored in each pixel. A detailed description on how to develop an application using TMS320C5509 is given in [29].

3.2.2 Metrology Ring

The SPHERES ultrasound beacon used for relative state estimation is currently mounted on the opposite side of the SPHERES Expansion Port, not on the side where the PPOP is mounted. Therefore, the PPOP needs to have its own metrology system for the case of controlling relative states of multiple Spheres without using the global metrology system. Even though not yet fully developed, the PPOP is equipped with the metrology ring shown in Figure 3-12 for relative coarse attitude control. The metrology ring consists of three identical metrology boards, each equipped with an Infra-Red (IR) transmitter/receiver and a Ultra-Sound (US) transmitter/receiver which enable the satellites to determine their positions relative to one another. Each board is an arc that is 1/3 of a ring with an inner diameter of 3 inches and an outer diameter of 3.8 inches. The metrology ring was originally developed for the Self-assembling Wireless Autonomously-Reconfigurable Modules (SWARM) project at the MIT-SSL. A detailed description of its functionality can be found in [5].

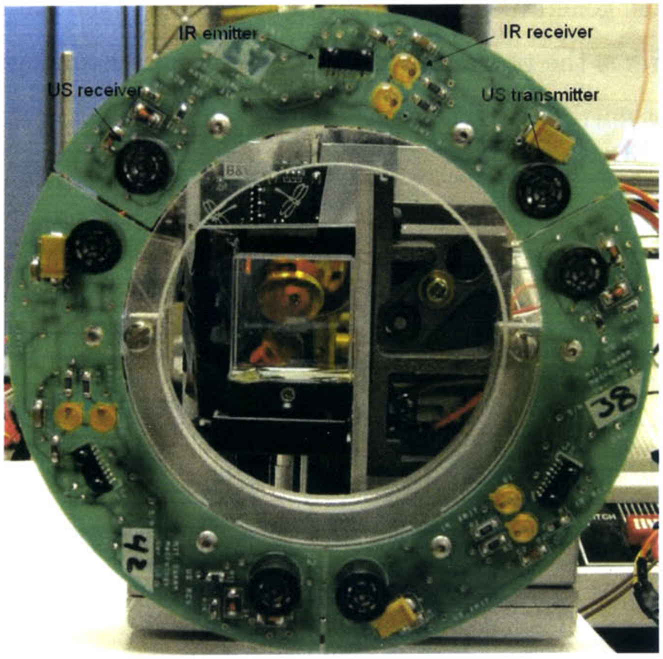

Figure 3-12: Metrology ring for relative state estimation

3.2.3 Fast Steering Mirror Actuation

Three GPIO pins on the UC1394a-1 MCM, one MAX5523 digital to analog (D-to-A) converter, and two LM4861 power amplifiers are used to generate appropriate analog input signals to the fast steering mirrors. MAX5523 is a 10-bit serial D-to-A converter and it requires three input signals: Data Input, Clock, and Chip Select signals. These three signals are generated by the UC1394a-1 MCM using a 10 kHz timer interrupt and sent to MAX5523 through the GPIO pins available on the UC1394a-1 MCM. The Data Input values are read in to MAX5523 on the rising edge of the Clock signal and the Chip Select signal must be asserted low while Digital Input values are read in. The three signals must meet the timing requirements given in [4] in order to successfully transmit the Data Input values. Upon receiving the Data Input values, MAX5523 generates two analog outputs, one for each mirror, according to the magnitude of the Data Input value received. An internal reference voltage of 3.89V is used, and since it is a 10-bit D-to-A converter, Data Input values of 0, 512, and 1023 create 0, 1.945, and 3.89V analog signals, respectively. LM4861 power amplifiers then amplify these analog signals, generating appropriate input signals to the fast steering mirrors. Figure 3-13 illustrates the process of generating appropriate analog power inputs to the power steering mirrors.

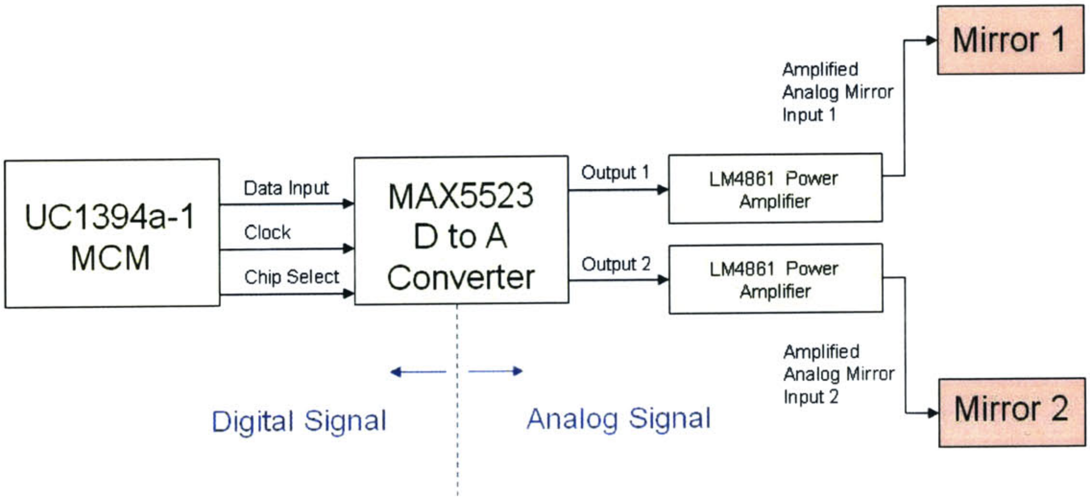

Figure 3-13: Process of generating analog inputs to the fast steering mirrors

Determining the Mirror Resolution

The resolution of the fast steering mirrors depends on both the resolution of the D-to-A converter and the gain used in the power amplifier. Figure 3-14 shows a typical LM4861 power amplifier circuit. Users need to choose the amplifier gain, $\frac{R_f}{R_i}$, appropriately for the desired range of the output signal. The voltage output of LM4861 can be determined using the following equation [3].

$$V_{out} = -\frac{R_f}{R_i}(2V_{in} - V_{ref}) \tag{3.5}$$

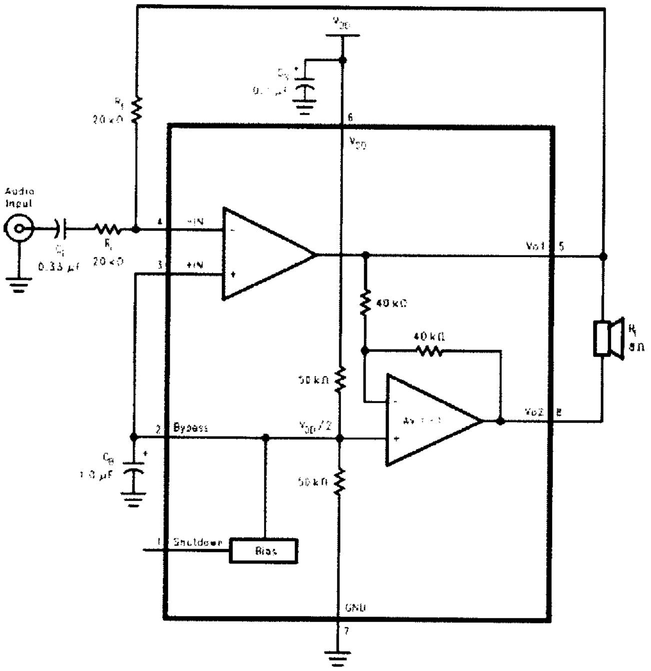

Figure 3-14: Typical LM4861 power amplifier circuit

47kΩ and 100kΩ were chosen for R_f and R_i, respectively. This gain along with V_{ref} of 3.89V produces ± 1.8283V output signals, which gives ±5.32° mirror actuation. Since the resolution of MAX5523 D-to-A converter is 10 bit, this gives the mirror resolution of $0.01^\circ/DA_{COUNT}$.

R_f	47kΩ
R_i	100kΩ
V_{ref}	3.89 V
D-to-A converter resolution	10 bit (1024)
Mirror range	±5.32°
Mirror resolution	$0.01°/DA_{COUNT}$

Table 3.4: Values used to set the range and resolution of the fast steering mirrors

3.2.4 Power

Power for the PPOP is provided by the SPHERES satellite through the SPHERES Expansion Port. There are three available power supplies at the SPHERES Expansion Port as shown in Table 3.5.

Power Supply	Rating
+5V	0.5A
+15V	0.5A
-15V	0.5A

Table 3.5: Power supplies available at the SPHERES Expansion Port

Out of the three available power supplies, +5V and +15V were chosen to provide power to the PPOP. Three power regulator circuits were built to produce +12V, +5V, and +3.3V out of the +15V supply. The regulated +12V provides power to the CCD-based camera whereas the regulated +5V provides power to the D-to-A converter chip and the power amplifier chips. The regulated +3.3V is used by the UC1394a-1 Multi-Chip Module. The unregulated +5V available at the SPHERES Expansion Port is used to power up the laser. A transistor circuit was built for the laser and On/Off of the laser was controlled by software using a GPIO pin on UC1394a-1 MCM. The complete schematics for the circuits implemented are given in Appendix D. Table 3.6 summarizes the power budget for the PPOP.

From +15V@0.5A (7.5W)	
UC1394a-1 MCM	3.3V@450mA (1.5W)
Camera	12V@~0.15A (~2W)
MAX5523 D/A Converter	5V@5μA (25μW)
LM4861 Amplifiers	2 x 5V@0.01A (0.05W)
From +5V@0.5A (2.5W)	
Laser	5V@0.015A (0.075W)
IR Receivers US Receivers/Translators	Miscellaneous

Table 3.6: Precision Pointing Optical Payload power budget

3.2.5 Data Communication with SPHERES

The US/IR Bypass lines available at the SPHERES Expansion Port are used to communicate the metrology data between a Sphere and the PPOP. All the other data are transmitted through the UART pins at the SPHERES Expansion Port using RS232 serial communication. The baud rate of 115200 bps was used for the serial communication.

Figure 3-15 shows the types of data transmitted through the serial communication between a Sphere and the PPOP. Sphere sends two different commands: the laser control command and the target centroid set command. The laser control command controls the power input to the laser. If the laser control command is 'On', then power is applied to the laser and the laser gets turned on. If the laser control command is 'Off', then power is not applied to the laser and the laser stays in its off state. The target centroid set command sends the desired location for the centroid of the laser beam to the PPOP. For example, if the center of the CCD is chosen as the desired location for the centroid of the laser beam, then the target centroid set command sends '$V_{Target} = 320$, $H_{Target} = 240$' to the PPOP, which is the location of center in the 480x640 CCD matrix.

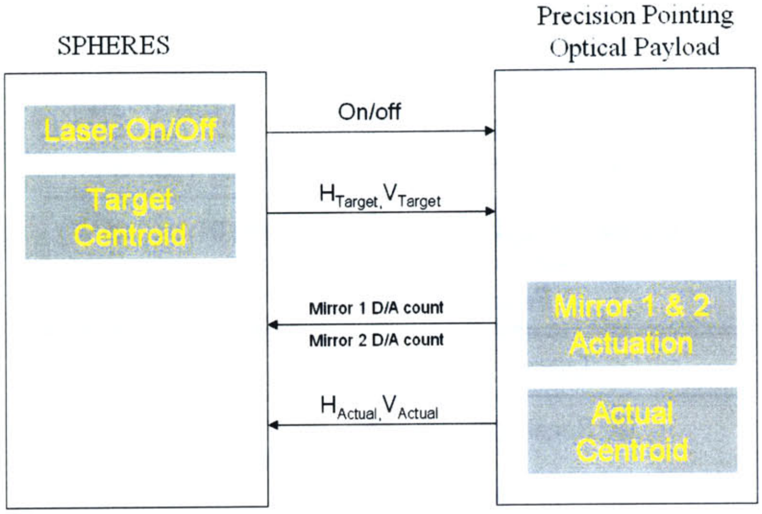

Figure 3-15: Types of data transmitted between a Sphere and the Precision Pointing Optical Payload

In return, the PPOP sends the mirror actuation magnitudes and the actual location of the centroid of the laser beam to the Sphere. The mirror actuation magnitudes can be obtained from the D-to-A counts applied to each mirror and it is the D-to-A counts that are actually sent to the Sphere. For example, D-to-A count of 1023 suggests that the mirror is actuated to the extreme in one direction whereas D-to-A count of 0 suggests that the mirror is actuated to the extreme in the other direction. D-to-A count of 512 suggests that the mirror is not actuated.

Each of the data transmitted through the serial communication is composed of six one-byte packets. The first byte is set to 0xFF and is used to signal the start of the data transmission. The second byte denotes the type of data being sent. The last four bytes contain the actual data. The sample code given in the following shows the packet structure for the target centroid set command. The second packet sets the target centroid location as the type of data being transmitted. The V_{Target} data is stored in the third and the fourth packet, and the H_{Target} data is stored in the fifth and the sixth packet.

```
void expOptPointTargetSet(unsigned int Vtarget,unsigned int Htarget)
{
    *SMT335CP4 = 0xFF;
    *SMT335CP4 = OPT_POINT_TARGET;
    *SMT335CP4 = (Vtarget && 0xFF);
    *SMT335CP4 = ((Vtarget>>8) && 0xFF);
    *SMT335CP4 = (Htarget && 0xFF);
    *SMT335CP4 = ((Htarget>>8) && 0xFF);
}
```

3.3 Design and Fabrication of Precision Pointing Optical Payload

Using SolidWorks, an engineering CAD software, the design for the PPOP was carried out. Simple joints with bolts and nuts were used. The beam splitter was mounted on an adjustable mount. Tip and tilt of the beam spitter can be adjusted by turning the knobs underneath the mount. The base plates have slots which enable the adjustment of the location of the object plane of the camera. The distance between the camera and the beam splitter was set such that the image of the beam splitter fills up slightly less than 480 pixels of the CCD sensor (refer to Figure 4-7). Figure 3-16 shows the CAD model developed for the PPOP.

Based on the CAD model, an actual prototype was fabricated out of aluminum using a milling machine, a lathe, and a waterjet. Figure 3-17 shows the actual prototype built for the PPOP.

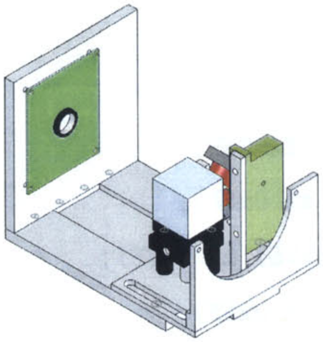

Figure 3-16: CAD model of the Precision Pointing Optical Payload developed using SolidWorks

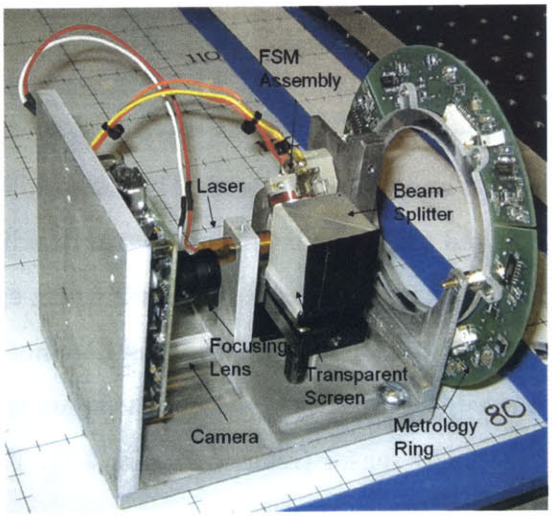

Figure 3-17: Prototype developed for the Precision Pointing Optical Payload

3.4 Chapter Summary

This chapter introduced the optical components and the avionics that constitute the Precision Pointing Optical Payload (PPOP). The fast steering mirrors were characterized and the key mirror performance metrics such as angular stoke and resolution were obtained. The main digital signal processor of the PPOP was described and its data communication with the SPHERES main processor was illustrated. The CAD model and the actual prototype of the PPOP were introduced. With the prototype built and the necessary data interfaces established, it is ready to perform precision pointing control experiments. The next chapter describes the controllers developed for staged pointing control experiments and the experimental results.

Chapter 4

Staged Pointing Control Using Precision Pointing Optical Payload

As discussed in Chapter 1, precision pointing control technology can provide fine pointing control in a staged optical pointing control in order to achieve stringent pointing requirements demanded by stellar inteferometry missions such as TPF-FFI. This chapter presents the staged pointing control experiments performed at the MIT-SSL using the Precision Pointing Optical Payload (PPOP) prototype developed. Coarse pointing control is accomplished using the SPHERES Position Attitude Determination System (PADS). The PPOP provides fine pointing control using the CCD-based camera as the sensor and the fast steering mirror(FSM) assembly as the actuators. The algorithms used for both coarse and fine pointing control are presented as well as the experimental data obtained.

4.1 Control Algorithms

To accomplish staged pointing, multiple control algorithms have been developed. The SPHERES global estimator and a proportional-derivative controller are used for coarse pointing control. For fine pointing control, the PPOP utilizes a centroid calculation algorithm and a proportional-integral-derivative controller. This section discusses the control algorithms developed for both coarse and fine pointing control.

4.1.1 Coarse Control

As mentioned in Section 2.1.2, the SPHERES PADS utilizes time-of-flight data of the ultrasound signals emitted by the external beacons and the IMU readings in order to determine states of each Sphere. The SPHERES PADS provides two different estimators: the global estimator for absolute state estimates and the relative estimator for relative state estimates. For the staged pointing control experiments performed, the absolute state estimates obtained using the global estimator are used. The state vector x is a 13x1 vector containing the position r, velocity v, quaternion q, and the angular rate ω components.

$$x = \begin{bmatrix} r^T & v^T & q^T & \omega^T \end{bmatrix} = [r_x \; r_y \; r_z \; v_x \; v_y \; v_z \; q_1 \; q_2 \; q_3 \; q_4 \; \omega_x \; \omega_y \; \omega_z] \tag{4.1}$$

The time-of-flight measurements are updated at 4 Hz, and the gyroscopes are sampled at 1 kHz. Since both the propagation of the attitude states and the computation of an absolute position based on time-of-flight measurements are non-linear, an extended Kalman filter is used to get the state estimates [28].

Once the absolute state estimates are obtained using the global estimator, the state errors are fed into a PD controller. The PD controller simply outputs force and torque commands proportional to state errors. The attitude angular error θ_e around the Euler axis defined by the unit vector $[n_x \; n_y \; n_z]$ is expressed in terms of quaternion,

$$\tilde{q} = [\tilde{q}_1 \; \tilde{q}_2 \; \tilde{q}_3 \; \tilde{q}_4] = \left[n_x \sin\left(\frac{\theta_e}{2}\right) \quad n_y \sin\left(\frac{\theta_e}{2}\right) \quad n_z \sin\left(\frac{\theta_e}{2}\right) \quad \cos\left(\frac{\theta_e}{2}\right) \right] \tag{4.2}$$

Then, the attitude control law is of the form [28],

$$T_x = 2 \cdot K_p \cdot \tilde{q}_1 + K_d \cdot \omega_x \tag{4.3}$$

$$T_y = 2 \cdot K_p \cdot \tilde{q}_2 + K_d \cdot \omega_y \tag{4.4}$$

$$T_z = 2 \cdot K_p \cdot \tilde{q}_3 + K_d \cdot \omega_z \tag{4.5}$$

The force and torque commands given by the PD controller are then converted to thruster On/Off time using a pulse-width modulator. The duration of the thruster firing pulse can be derived through the conservation of thrust impulse during each control period [22]. The control update frequency of 1 Hz is used in the experiments. The timing diagram of the coarse pointing control using the global estimator and the PD controller is given in Figure 4-1.

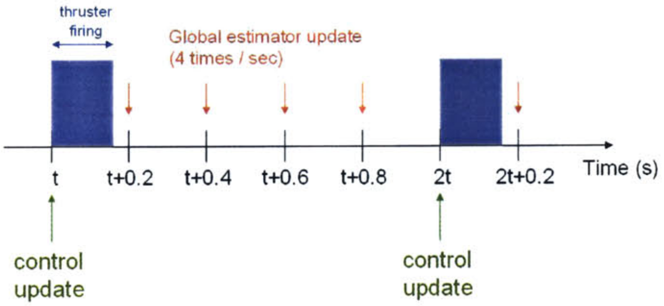

Figure 4-1: Timing diagram for the coarse attitude control

4.1.2 Fine Control

Once the SPHERES PADS brings the Sphere within the close proximity of the target position, the fine pointing control of the PPOP takes over. In order to accurately point to the target attitude, the PPOP uses the CCD-based camera as its sensor. Using the fast steering mirrors as the actuators, the objective of the PPOP is to maintain the location of the laser dot on the CCD at the target location (center) of the CCD. This requires two separate algorithms, one for calculating the centroid of the laser dot on the CCD and the other one for actuating the fast steering mirrors. Each of the two algorithms is described in the following.

Centroid Calculation

Many different methods have been developed to determine the centroid of a light source, and these are commonly used in star-tracking algorithms. Here, two such algorithms are presented.

The first algorithm uses a pre-set threshold value. It scans each of the pixels on the CCD until an intensity value above the pre-set threshold is found. Once such a pixel is found, the algorithm records the pixel location and increments its counter by one. The locations of the pixels with an intensity value above the pre-set threshold are added together, and the centroid of the light source (e.g. laser beam) is obtained by dividing the sum of the locations of the bright pixels by the total count. Figure 4-2 illustrates a sample centroid calculation using the first algorithm.

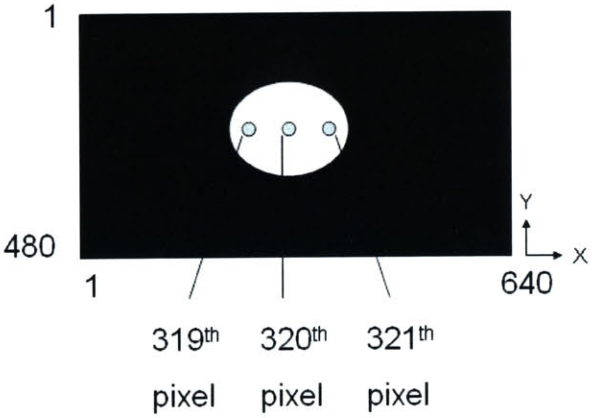

$$Centroid\ X = \frac{319+320+321}{3} = 320$$

Figure 4-2: A sample centroid calculation using a threshold intensity value

The second algorithm uses the center of intensity approach given in Equation 4.6:

$$Centroid = \frac{\Sigma_{i=1}^{n} i \cdot intensity_i}{\Sigma_{i=1}^{n} intensity_i} \tag{4.6}$$

where n is the number of pixels along the x axis or the y axis of a CCD matrix.

One advantage of the second algorithm over the first algorithm is that the second algorithm produces more accurate results for the centroid calculation. For example, as illustrated in Figure 4-3, if a circular laser beam with its brightest source located at an off-center position were used, then the first algorithm would still calculate the centroid of the beam to be at the center of the beam, whereas the second algorithm would calculate the centroid to be located at some place closer to the brightest source, thus producing more accurate result.

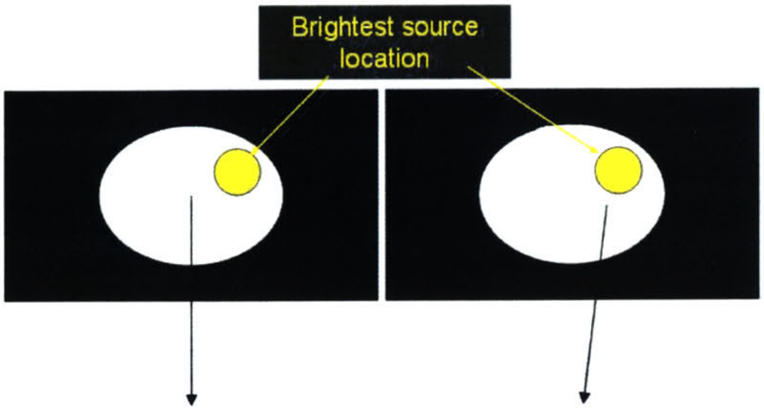

Centroid is still at the center if the first algorithm were used.

The second algorithm takes the brightest point into account and the centroid is somewhere closer to the yellow dot, not at the center thus producing more accurate result.

Figure 4-3: Accuracy comparison between the first algorithm and the second algorithm

However, the second algorithm takes every pixels into account when performing the centroid calculation, even the pixels with zero intensity. This makes the second algorithm computationally inefficient when compared to the first algorithm which takes into account only the pixels with high intensity. The centroid calculation times for the two algorithms were measured on an oscilloscope by probing the signals from a General Purpose Input Output (GPIO) pin on the UC1394a-1 multi-chip module. The GPIO pin was set high at the beginning of the centroid calculation and was brought back to low at the end of the centroid calculation. The processing time for the first algorithm depends on the size of the laser dot on the CCD, which in turn determines the number of pixels with an intensity above the pre-set threshold value. The laser dot shown in Figure 4-4 was used for the processing time measurements for the two algorithms.

Figure 4-4: Image of the laser dot used for the centroid calculation time measurements

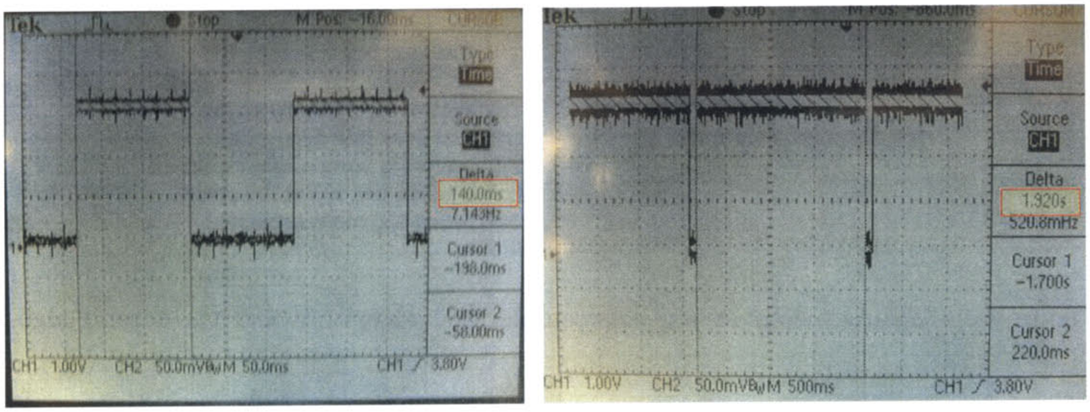

Figure 4-5: Centroid calculation time comparison: (Left) the first algorithm takes 140 ms to run, (Right) the second algorithm takes 1920 ms to run

As can be seen in Figure 4-5, the first algorithm takes ~140 ms to run whereas the second algorithm takes ~1920 ms to run. Even though the second algorithm provides more accurate results, its slow processing time makes the second algorithm not a suitable algorithm to use. On the other hand, the first algorithm runs faster but does not provide results as accurate as the results provided by the second algorithm. For precision pointing control, an algorithm that is both fast and accurate is desired.

Therefore, the first algorithm and the second algorithm are combined together in order to provide accurate centroid values with a short amount of time.

The combined algorithm still uses the center of intensity approach. However, unlike the second algorithm, it only uses the pixels with an intensity above the preset threshold intensity for the centroid calculation. Using both the first and the second algorithms makes it possible to preserve the accuracy provided by the second algorithm, and at the same time, to save processing time by not considering the pixels with low intensity. As illustrated in Figure 4-6, the combined algorithm takes ~168 ms to run, which is significantly faster than the second algorithm. For the laser dot shown in Figure 4-4, the first, the second, and the combined algorithm calculate the centroid (x,y) of the dot to be: (354, 225), (361, 233), (362, 233), respectively.

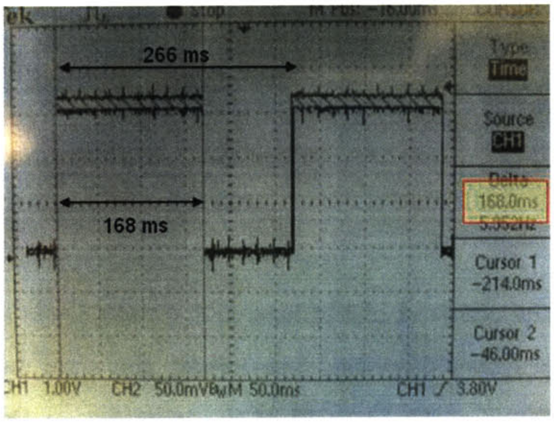

Figure 4-6: The combined algorithm takes 168 ms to run

Note that all the three algorithms sampled only the regions covered by the transparent screen (Figure 4-7) instead of the full 480x640 CCD matrix, when generating the results described above. The sub-sampling allows a further increase in the efficiency of the algorithms.

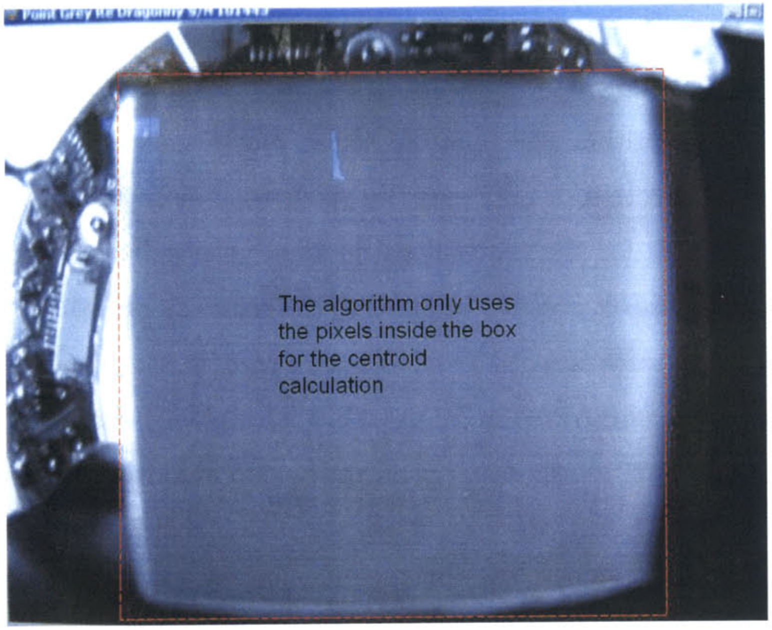

Figure 4-7: Illustration of Sub-sampling: Only the interested regions on the CCD are sampled to further increase the efficiency of the algorithm. (Image is taken after removing the optical filter)

Mirror Control

Once the location of the centroid of the laser dot on the CCD is obtained using the combined centroid algorithm described previously, the error between the center of the CCD and the location of the centroid of the laser dot on the CCD is computed. Then, the PPOP actuates the fast steering mirrors based on the magnitude of the error, and fine pointing control is achieved as the error is reduced. The control laws for the fast steering mirror actuations are developed using a PID controller. Using Euler's method (Equation 4.7) for the approximation of derivatives, the discrete forms of the PID control terms are derived as shown in Equations 4.8 through 4.10.

$$\dot{x}(k) \simeq \frac{x(k+1) - x(k)}{T} \tag{4.7}$$

where $T = t_{k+1} - t_k$ (time interval), $x(k)$ is the value of x at t_k, and $x(k+1)$ is the value of x at t_{k+1}.

$$Proporional: \quad u(k) = Ke(k) \tag{4.8}$$

$$Integral: \quad u(k) = u(k-1) + \frac{K}{T_I} Te(k) \tag{4.9}$$

$$Derivative: \quad u(k) = \frac{KT_D}{T}[e(k) - e(k-1)] \tag{4.10}$$

where K is the proportional gain, T_I is the integral time, and T_D is the derivative time.

Then, the three terms in Equations 4.8 through 4.10 are combined to yield,

$$u(k) = u(k-1) + K\left[\left(1 + \frac{T}{T_I} + \frac{T_D}{T}\right)e(k) - \left(1 + 2\frac{T_D}{T}\right)e(k-1) + \frac{T_D}{T}e(k-2)\right] \tag{4.11}$$

where $e(k)$ is the value of the error between the center of the CCD and the location of the centroid of the laser dot on the CCD at t_k, $e(k-1)$ is the value of e at t_{k-T}, $e(k-2)$ is the value of e at t_{k-2T}, $u(k)$ is the digital input to the digital-to-analog converter at t_k (which, in turn, provides the analog input to the fast steering mirror), and $u(k-1)$ is the value of u at t_{k-1}.

As can be seen in Figure 4-6, the time interval T between the control updates is ~266 ms. Of the available 266 milliseconds, the first 168 milliseconds are used for the centroid calculation, and the remaining 98 milliseconds are used for the mirror control.

Note that when combining the control terms in Equations 4.8 through 4.10, a care has to be provided [20]. The combined continuous transfer function D is

$$D(s) = \frac{u(s)}{e(s)} = K\left(1 + \frac{1}{T_I s} + T_D s\right). \tag{4.12}$$

Then, the differential equation relating $u(t)$ and $e(t)$ is

$$\dot{u} = K\left(\dot{e} + \frac{1}{T_I}e + T_D\ddot{e}\right) \tag{4.13}$$

Using Euler's method (twice for $\ddot{e}$), the PID control law can be obtained as shown in Equation 4.11.

The block diagram for the staged pointing control is shown in Figure 4-8. The centroid data and the mirror actuation data are passed to the SPHERES DSP (denoted by the dotted lines), however, they are currently not being used to affect the control laws for the coarse pointing control. The durations for the thruster firings are determined only using the global estimator and the PD controller. Future versions of the coarse controller will include the integration of the data passed from the PPOP to affect the thruster firings.

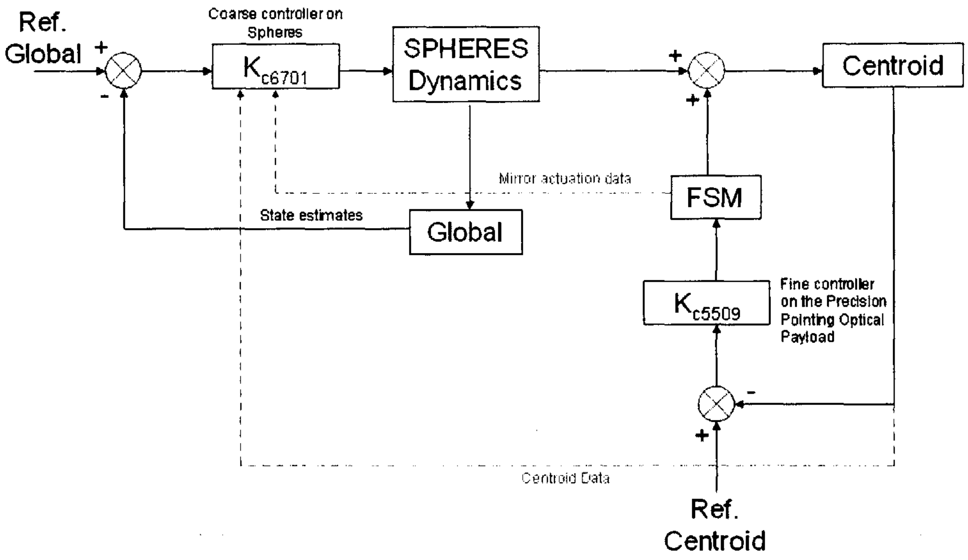

Figure 4-8: Block diagram for staged pointing control

4.2 Experiments

This section describes the experiments performed to demonstrate the staged pointing control. Three different experiments were performed: (i) coarse pointing using the coarse controller only, (ii) fine pointing using the fine controller only, and (iii) staged pointing using both the coarse and the fine controller. The experimental results for each test case are presented in the following.

4.2.1 Coarse Pointing Using Coarse Controller Only

This section presents the results obtained from the attitude hold experiments performed using the coarse controller provided by the SPHERES global estimator and the PD controller. The fine controller of the PPOP was not used. The experiments were performed for the purpose of illustrating how accurately the coarse controller can control the attitude of the Sphere before the fine control stage begins. The test setup is shown in Figure 4-9.

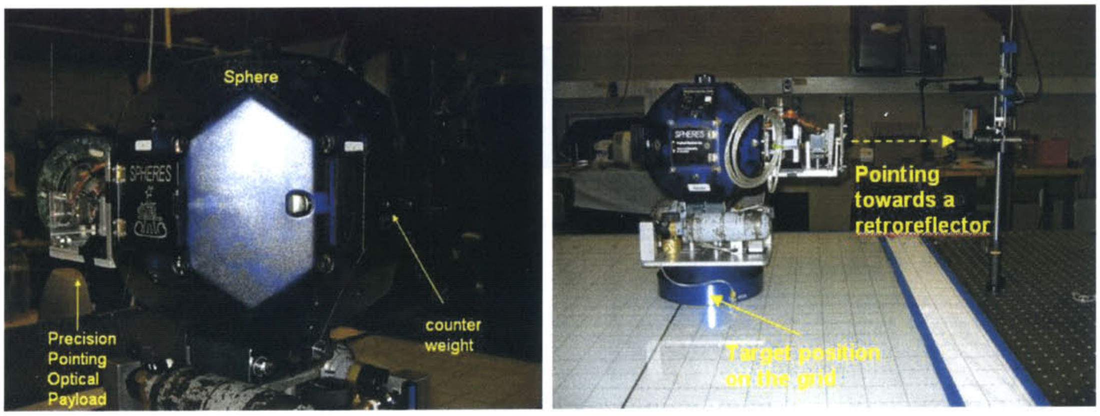

Figure 4-9: Test setup for attitude hold experiments

The PPOP and a counter weight were attached to the Sphere. The target state vector of [0.75 1.30 1.35 0 0 0 0 0 1 0 0 0 0] was used, which commanded the Sphere to hold its position at (x, y, z) = (0.75 m, 1.30 m, 1.35 m) in the global reference frame and point towards the retroreflector with zero translational and angular velocity.

The moment of inertia of the PPOP was estimated using a hanging pendulum, and the mass property of the Sphere was modified to take the added mass into account. Figure 4-10 shows the hanging pendulum used to estimate the moment of inertia of the PPOP with respect to the vertical axis.

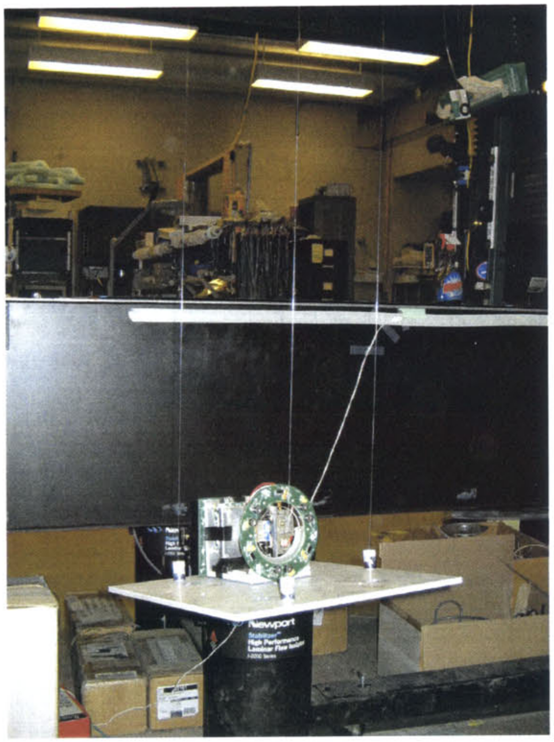

Figure 4-10: Estimating the moment of inertia of the Precision Pointing Optical Payload using a hanging pendulum

The PPOP was placed on the plate of the hanging pendulum, and a small angular disturbance was applied to the plate. The time it takes to undergo ten oscillations was measured. Using Equation 4.14 [27], first, the moment of inertia, J, of the combined system of the plate and the PPOP about the vertical axis was obtained to be 0.03875 kg m^2. Then, the moment of inertia of the plate alone (0.0322 kg m^2) was subtracted from the moment of inertia of the combined system to provide the moment of the inertia of the PPOP. The moment of the inertia of the PPOP about the vertical axis was obtained to be 0.0065 kg m^2. The results are listed in Table 4.1.

$$J = \frac{mgr^2T^2}{4n^2\pi^2 l} \tag{4.14}$$

where m is the combined mass of the plate and the PPOP in kg, g is the gravitational constant (9.81 kg/s), r is the average distance between the center of the plate to the hanging lines in m, n is the number of oscillations, T is the time it takes to complete n oscillations in sec, and l is the average length of the hanging lines in m.

Mass	Plate: 1.844 kg Precision Pointing Optical Payload: 0.896 kg Combined: 2.74 kg
r	0.14605 m
T	25.53 s
n	10 oscillations
l	2.446 m
J obtained	Combined: 0.03875 kg m^2 Plate: 0.0322 kg m^2 Precision Pointing Optical Payload: 0.0065 kg m^2

Table 4.1: Moment of inertia measurement for the Precision Pointing Optical Payload

Using 4 Hz update frequency for the global estimator and 1 Hz update frequency for the PD controller, the state measurements from the position/attitude hold experiment were obtained as shown in Figure 4-11.

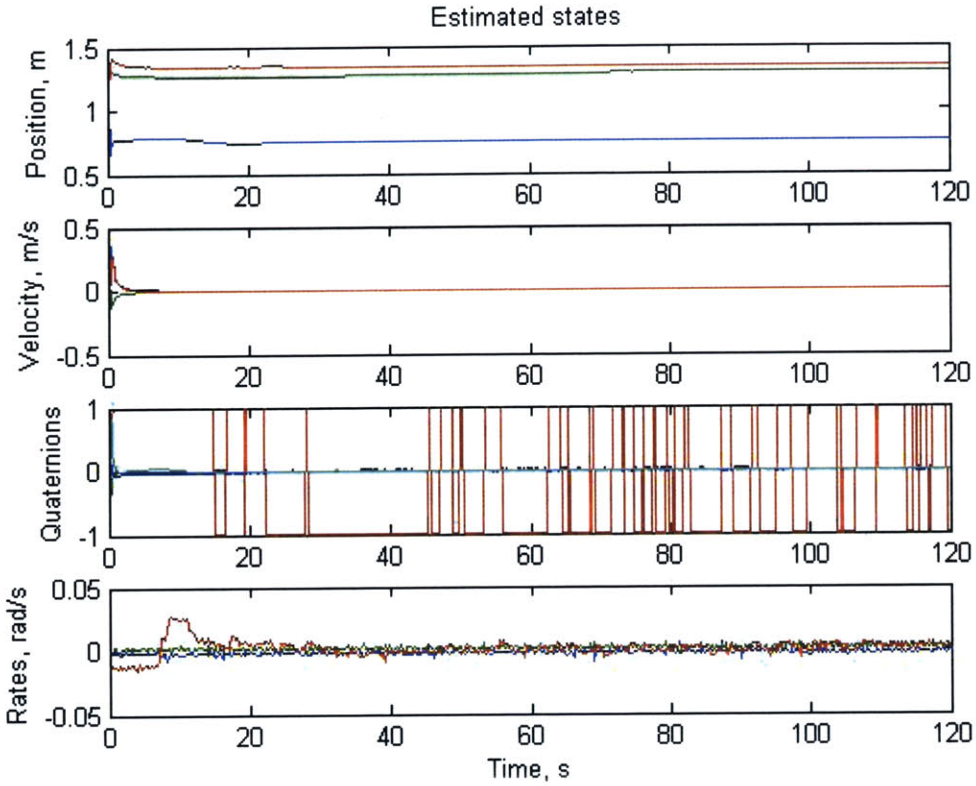

Figure 4-11: State measurements during the position/attitude hold experiment using coarse control. Target states: [0.75 1.30 1.35 0 0 0 0 0 1 0 0 0 0].

All the states were observed to converge towards the target states. The position errors were obtained to be less than 1 cm for all x, y, z directions in the steady state. Note that one of the quaternions, q_3 oscillates between 1 and -1. This is a numerical ambiguity of the global estimator caused by 180° being equal to -180°. The quaternions were converted to degrees, and the angular error of $\sim \pm 1°$ about the vertical axis was obtained as illustrated in Figure 4-12.

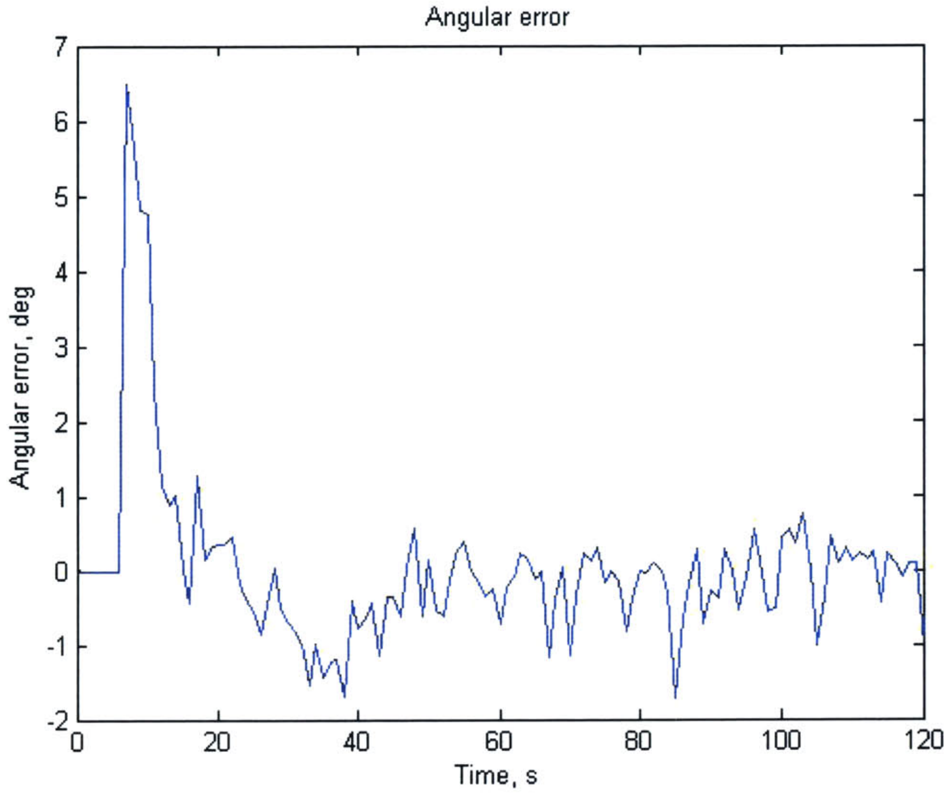

Figure 4-12: Angular error provided by coarse control

The retroreflector was placed 25 cm from the beam splitter of the PPOP, and the movements of the laser dot on the CCD during coarse control without any mirror actuations were measured as shown in Figure 4-13.

Since the Sphere moves only horizontally in the 1-g environment, the motion of the laser dot in the vertical direction is more stablized than the motion in the horizontal direction. The laser dot stays within ∼ ±40 pixels from its pre-aligned location (320) in the vertical direction. For the horizontal direction, the laser dot wanders around on the CCD with a maximum edge to edge separation of ∼ 420 pixels.

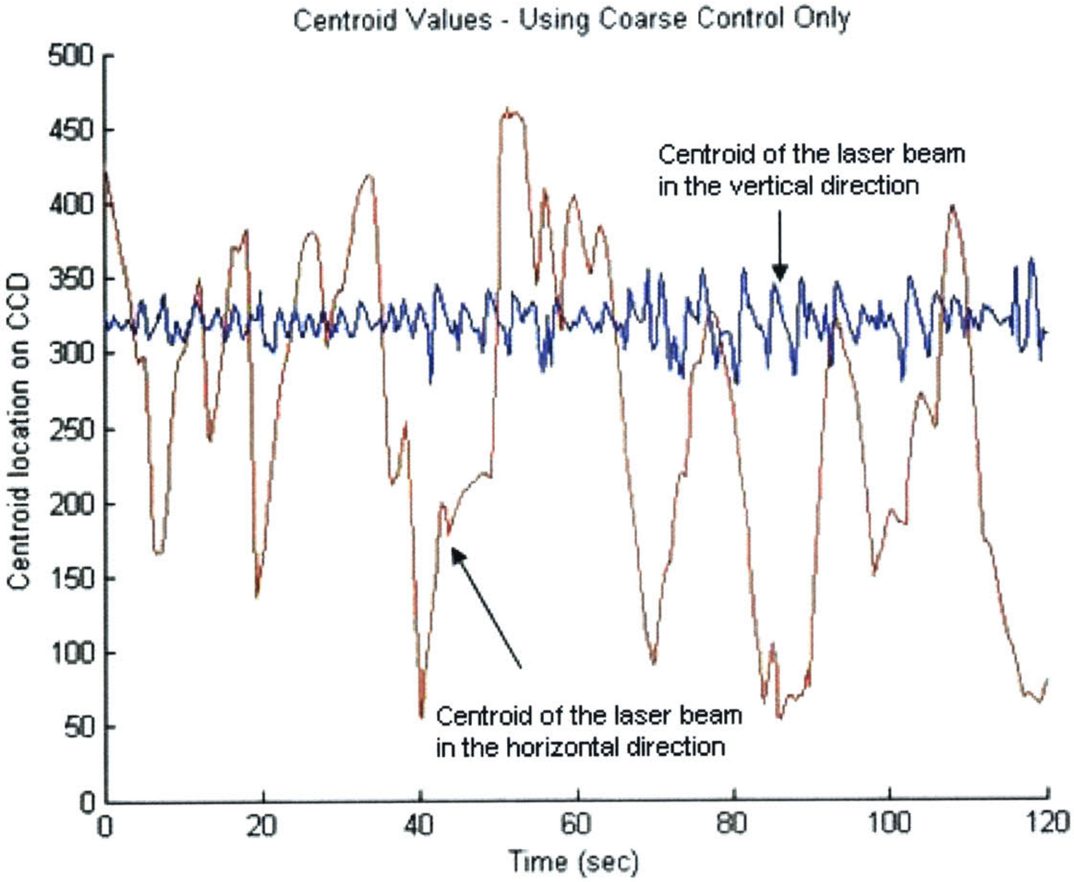

Figure 4-13: Movements of the laser dot on the CCD during coarse control at 25 cm range

4.2.2 Fine Pointing Using Fine Controller Only

This section presents the experimental results obtained using only the PID controller of the Precision Pointing Optical Payload (PPOP). Instead of using an actual Sphere, the SPHERES external stack shown in Figure 4-14 was used in the experiments, simulating a stationary Sphere. The SPHERES external stack is an exact replica of the SPHERES electronics specifically developed for code developments and debugging without risking an actual flight hardware. Using the SPHERES external stack, perturbations in the vertical direction as well as the horizontal direction could be applied.

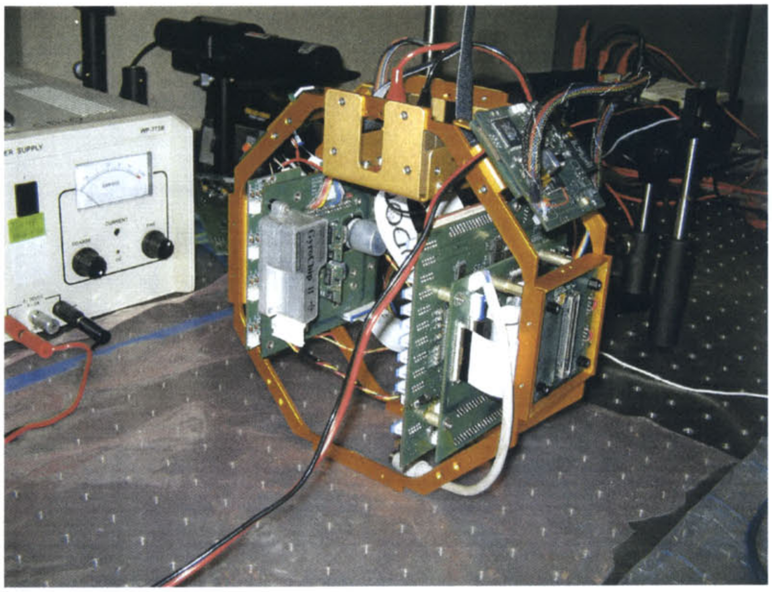

Figure 4-14: SPHERES external stack

The target centroid location was chosen as the center of the 480x640 CCD matrix, (240, 320). The objective of the fine controller was to maintain the laser dot at the target location on the CCD under the presence of perturbations. Two ranges (the distance between the beam splitter and the retroreflector as defined in Section 2.4) were chosen: 25 cm and 50 cm, and initial perturbations were given in both the horizonal and vertical directions. The results are shown in Figures 4-15 and 4-16.

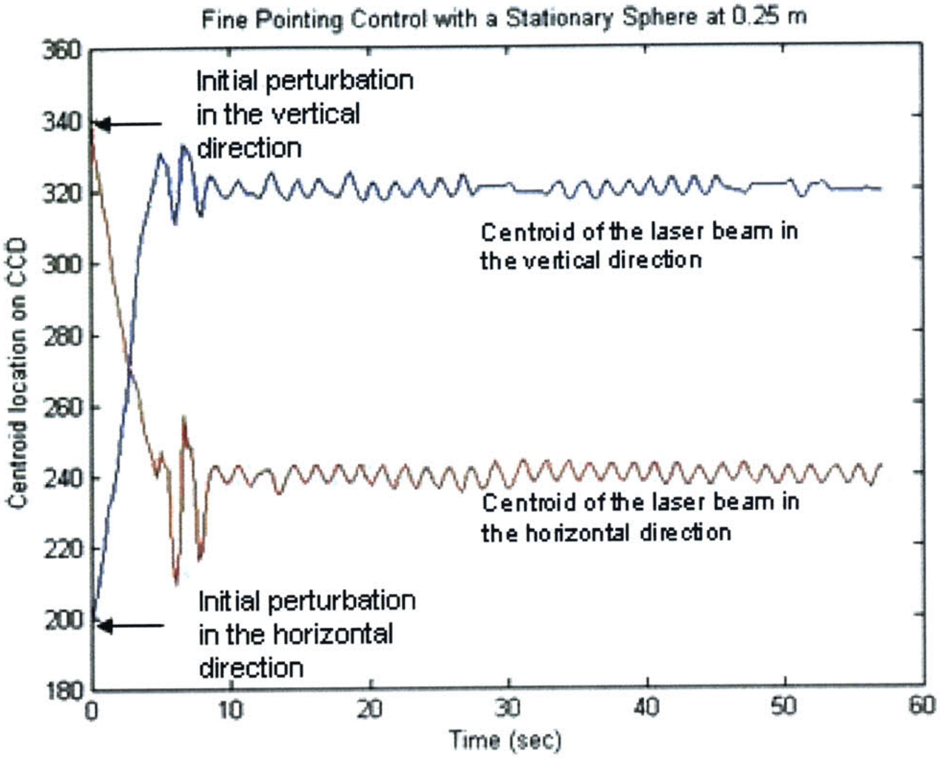

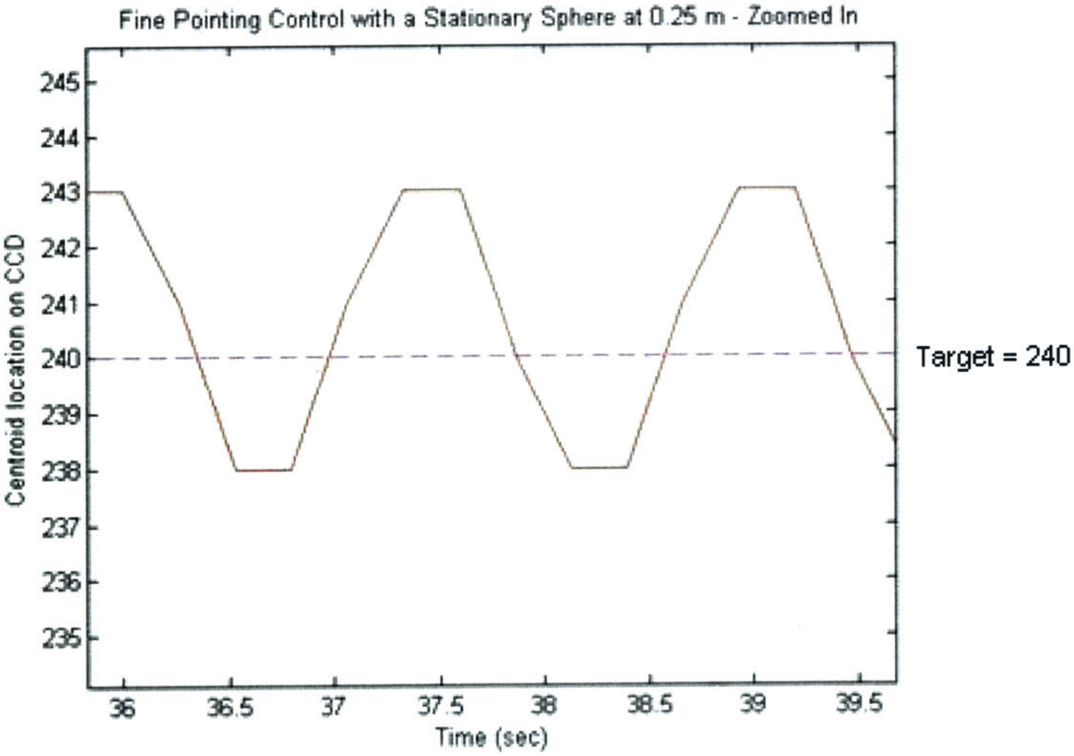

Figure 4-15: Movements of the laser dot on the CCD during fine control at 25 cm range

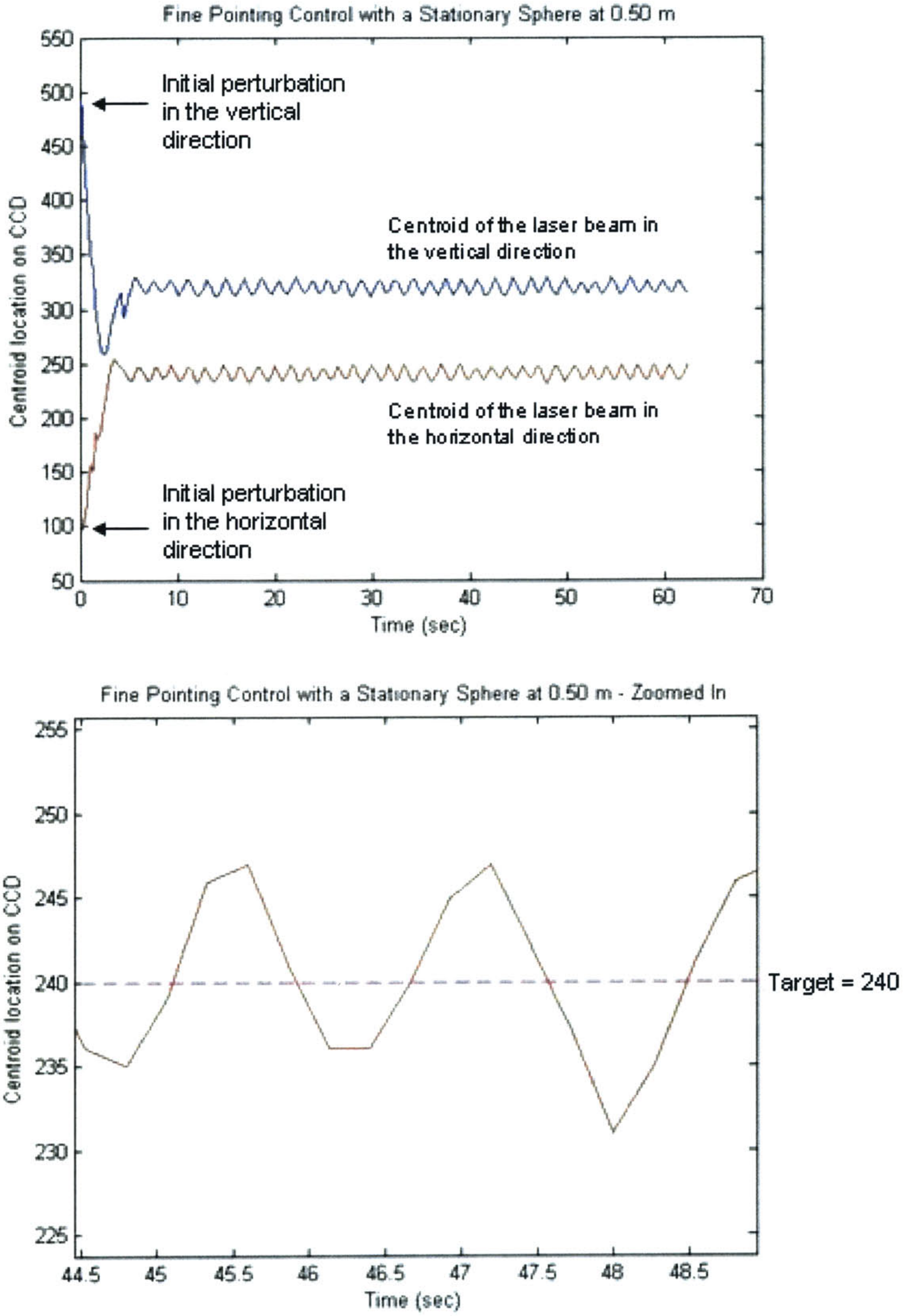

Figure 4-16: Movements of the laser dot on the CCD during fine control at 50 cm range

The error between the location of the centroid of the laser dot on the CCD and the target location on the CCD was obtained to be ~ ±3 pixels for the range of 25 cm. This value increased to ~ ±7 pixels for the range of 50 cm. The oscillatory behavior can be explained by the limitation in the resolution of the the digital-to-analog (D-to-A) converter. The theoretical calculation for the shortest possible displacement of the laser dot on the CCD that can be provided by the mirrors is presented in the following.

In Section 3.2.3, it was determined that one increment in the D-to-A count actuates the fast steering mirrors by ~ 0.01°. Using the ray tracing analysis developed in Section 2.4, the displacement of the laser dot on the transparent screen caused by 0.01° mirror actuation can be first found. This value represents the shortest possible displacement of the laser dot on the transparent screen that can be made by the mirror actuation. Then, the shortest possible displacement of the laser dot on the CCD can be obtained using the thin lens theory illustrated in Figure 4-17. The following relationships for a thin lens are used:

$$\frac{1}{S_o} + \frac{1}{S_i} = \frac{1}{f} \tag{4.15}$$

$$Y_i = \left(\frac{S_i}{S_o}\right) Y_o \tag{4.16}$$

where f is the focal length of the camera lens. The results are shown in Table 4.2.

	Range: 0.25 m	Range: 0.50 m
Minimum displacement on transparent screen	2.02 x 10^{-4} m	3.75 x 10^{-4} m
Minimum displacement on CCD	3.81 x 10^{-5} m	7.14 x 10^{-5} m
Minimum displacement on CCD in pixels	5.15 pixels	9.65 pixels

Table 4.2: The shortest possible displacements provided by the fast steering mirrors

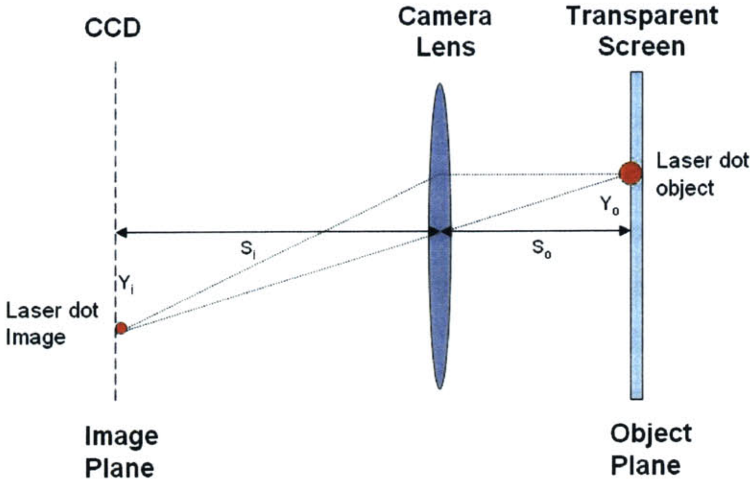

Figure 4-17: The laser dot on the transparent screen being imaged on the CCD

As can be seen in Table 4.2, the theoretical resolution of the laser dot movement on the CCD is ~5 pixels for the range of 25 cm and ~10 pixels for the range of 50 cm. This means that as long as there is an error between the target location and the location of the centroid of the laser dot, the mirror actuation causes the laser dot to oscillate around the target location. If the error were zero, then the laser dot would stay at the target location when a stationary Sphere is used. Using a higher resolution D-to-A converter would reduce the amplitude of the oscillations as long as the D-to-A converter provides the mirrors analog inputs higher than the minimum inputs required by the resolution of the mirrors. It should be noted that the results in Table 4.2 were obtained assuming no misalignments in both translational and angular directions. The experimentally obtained amplitudes of the oscillations from Figures 4-15 and 4-16 are slightly bigger (~6 pixels for the range of 25 cm and ~14 pixels for the range of 50 cm) than the theoretical results obtained under the ideal conditions.

Even though the SPHERES external stack is not moving, once the laser dot is positioned at the target location, it does not stay there constantly. For example, the curve for the vertical beam pointing control (with its target location set at 320) shown in Figure 4-15, does contain short durations of flat regions, which indicate that the laser dot is at the target location and stays there for a while. However, the flat region ends quickly followed by the regions of oscillations. The reason for the short durations of the flat regions is that the slight misalignments in mirror mounts, laser mounts, and other various components, cause the mirrors to affect the movement of the laser dot not only in their major control direction, but also in the other direction that they are not responsible for. In Figure 4-15, when one of the two mirrors gets actuated to control the location of the laser dot in the horizontal direction (with its target set at 240), it does also affect the vertical location of the laser dot slightly and causes errors in the vertical direction, actuating the other mirror to control the vertical motion of the laser dot.

4.2.3 Staged Pointing Using Both Coarse and Fine Controller

To demonstrate staged pointing control with a floating Sphere, both coarse control provided by the SPHERES global metrology system and fine control provided by the PPOP were used in subsequent stages. The retroreflector was placed 25 cm from the beam splitter of the PPOP.

To initiate the staged pointing control, a command was sent wirelessly from the desktop station to the Sphere. The Sphere then used its global metrology system to position and orient itself to the target states defined. Once the motion of the Sphere was stabilized using the global metrology system, the fine pointing control provided by the PPOP was activated. The PPOP computed the error between the location of the centroid of the laser dot and the target centroid location on the CCD, and each of the two fast steering mirrors was actuated appropriately depending on the magnitudes of the errors. The process of acquiring the CCD image, calculating the error, and actuating the mirrors was repeated with an update rate of approximately 3 Hz. The SPHERES global metrology system was activated throughout the test and it continuously provided the coarse position/attitude control. An update rate of 4 Hz was used for acquiring the absolute states using the global estimator, and an update rate of 1 Hz was used for controlling thruster firings using the PD controller. The test result is shown in Figure 4-18.

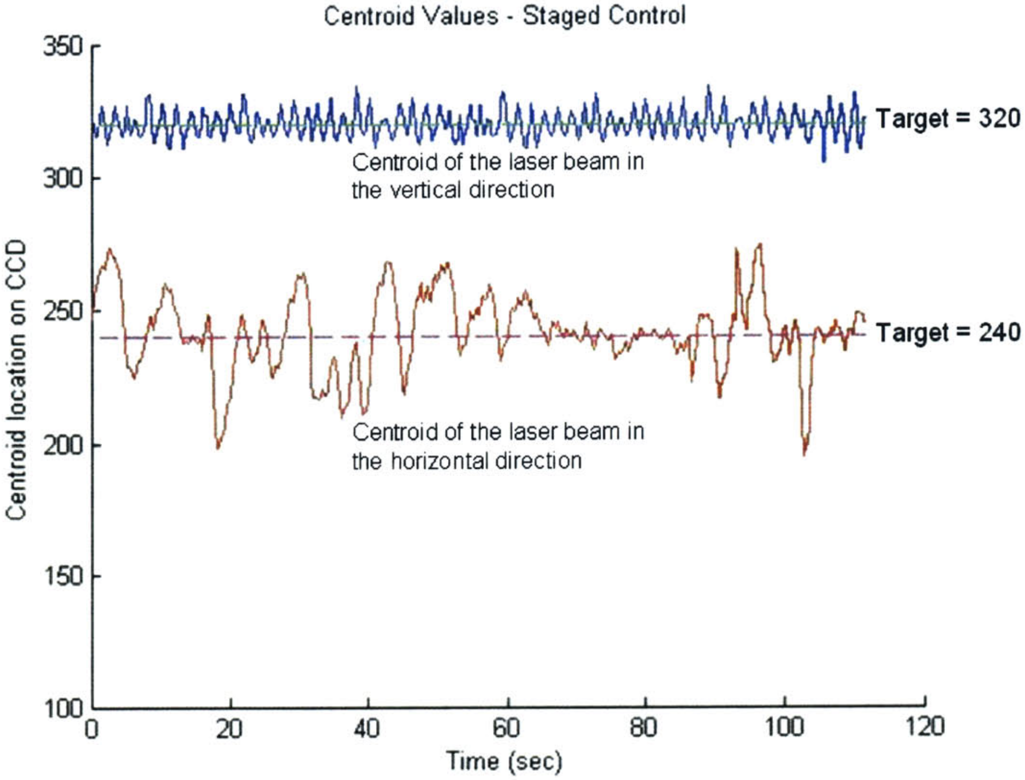

Figure 4-18: Centroid of the laser dot during staged Control at 25 cm range

Since the Sphere was floating only in the horizontal direction, the staged pointing control provided better results for the vertical motion of the laser dot as expected. For the vertical direction, the average error between the location of the centroid of the laser dot on the CCD and the target location on the CCD (320) was estimated to be $\sim \pm 10$ pixels from Figure 4-18. For the horizontal direction, the error was obtained to be $\sim \pm 40$ pixels.

As can be seen in Figure 4-18, the staged pointing control provided notable improvements in the performance when compared with the performance obtained using the coarse control only. The centroid location errors were reduced from $\sim \pm 40$ pixels to $\sim \pm 10$ pixels in the vertical direction, and from $\sim \pm 420$ pixels to $\sim \pm 40$ pixels in the horizontal direction. However, the staged attitude pointing control did not quite meet the performance accuracy provided by the fine control ($\sim \pm 3$ pixels for the range of 25cm).

The gains chosen for the PID controller might have not been the most optimized values and might have caused the performance discrepancy between the staged control and the fine control. The control gains were selected based on trial and error, mainly due to the complexity associated with the time variant nature of the system. As shown in Figure 4-19, the controller selects appropriate inputs for the mirrors depending on the magnitudes of the centroid location errors. Then, the mirrors get actuated, which, in turn, changes the location of the laser dot on the CCD by Δ_{ver} and Δ_{hor}. However, the magnitudes of Δ_{ver} and Δ_{hor} caused by a fixed value of θ_{mirror} keep changing depending on how the beam gets reflected at the retroreflector as depicted in Figure 4-20. This means that different Δ_{ver} and Δ_{hor} could be generated even for the same magnitudes of errors in the centroid locations. As the Sphere moves around, the laser beam hits the retroreflector at different locations with different angles, causing the angle and location of the beam coming into the beam splitter constantly change. This causes different Δ_i's on the transparent screen. In turn, different Δ_i's cause different Δ_{ver} and Δ_{hor} even when a fixed θ_{mirror} is used, thus making the control system time variant. Future versions of the controller will take the time variant nature of the system into consideration and will include models for the system dynamics (mirror model shown in Appendix B).

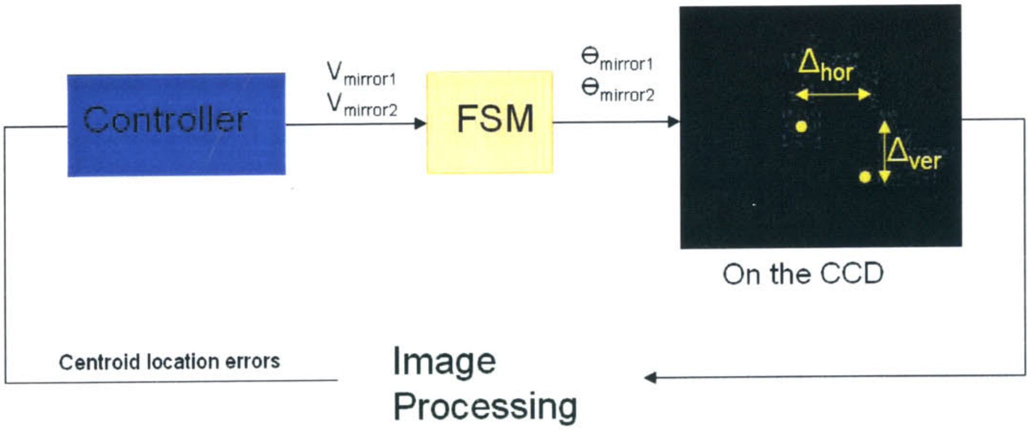

Figure 4-19: Process of the fine pointing control

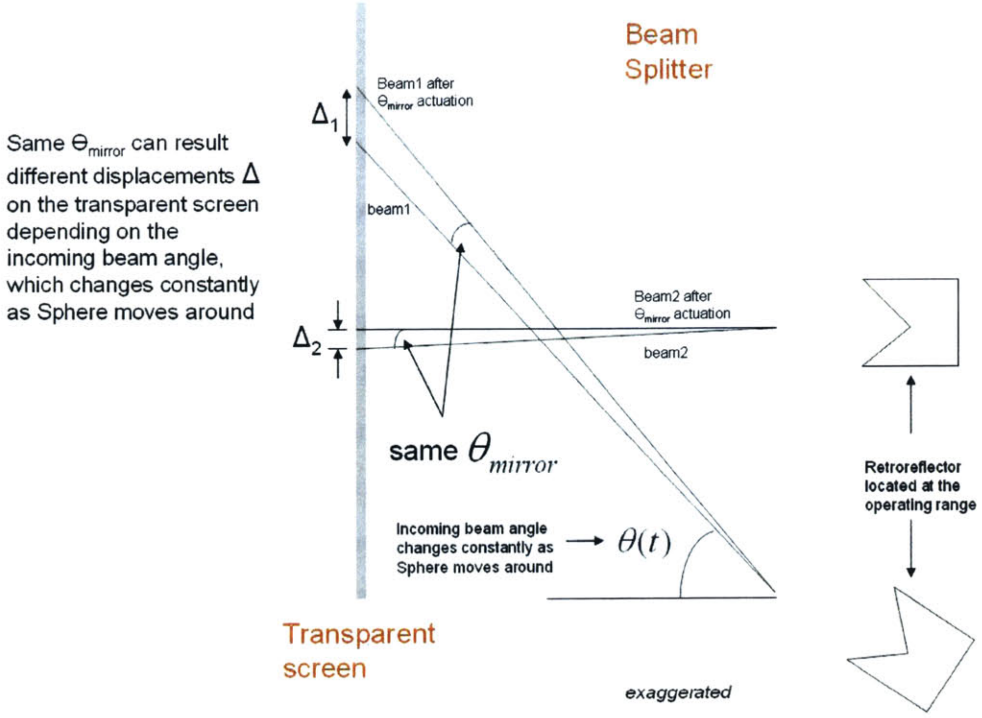

Figure 4-20: Time variant nature of the control system

Future versions of the controller can also include a thruster model to improve the pointing control performance. Considering that it is the thruster firings that actuate the Spheres, if the controller for the fine pointing control knows the thruster firings prior to they actually happen, the fine controller can, perhaps, perform better control by compensating the possible disturbances expected from the next thruster firings before they occur. Currently the communication interface between the Sphere and the PPOP is not being used for control purposes. The thruster model can compute the expected thruster firings and transmit the data containing the expected future thruster firings to the PPOP through the communication interface. Also the centroid data and mirror actuation data sent to the Sphere from the PPOP can be used to affect the control laws for the thruster firings to improve the pointing control performance.

Eliminating the possible sources of error such as improper camera mounting, lens defects, and the friction between the air-bearing pucks and table will also improve the pointing control performance.

4.3 Chapter Summary

This chapter discussed the attitude/position hold experiments performed to demonstrate the staged pointing control concept described in Chapter 2. The SPHERES global metrology system provided the coarse pointing control, whereas the PPOP provided the fine pointing control. Three different experiments were performed: coarse pointing with a floating Sphere using only the coarse control, fine pointing with a stationary Sphere using only the fine control, and staged pointing with a floating Sphere using both the coarse and the fine control. The experimental data were presented, and the performances of the three test cases were compared. As expected, the fine control applied to a stationary Sphere provided the best results among the three test cases, followed by the staged control and the coarse control. The performance of the staged control was not as good as the performance of the fine control. However, the staged control provided notable improvements in the pointing performance when compared to the performance provided by the coarse control.

Chapter 5

Parametric Integrated Modeling of Space Telescope Architectures

The next generation of large, lightweight space imaging systems will require a combination of advanced technologies including lightweight optics to reduce the areal density of mirrors and active optical control to compensate for the increased flexibility of the systems. These new design technologies open up many new possibilities for space telescope architectures, requiring innovative approaches to identify which architecture families most favorably meet the stringent performance requirements. The MIT Space Systems Laboratory (MIT-SSL) is examining alternative architectures for a Modular Optical Space Telescope (MOST) by developing a simulation tool that automatically produces unique realizations of a space telescope model based on parametric inputs. This chapter describes the parametric integrated model developed for the MOST project with particular emphasis on the optics model development.

5.1 Overview of the MOST Model

Development of the next generation of large, lightweight space imaging systems will utilize advanced technologies such as lightweight optics and active control, creating many new possibilities for telescope architecture choices. In the traditional design approach, a single (or at most several) architecture is chosen in the conceptual design stage, mostly based on the experience from the previous missions. The chosen architecture is then passed onto the preliminary design stage, and only then are detailed models created and various analyses performed for the single architecture chosen. However, if the chosen architecture fails to meet the mission requirements, a costly redesign must be performed. In order to mitigate the risk of costly redesigns in the later stages of the design lifecycle, the MOST project has been developing a parametric model for the design of an advanced large, lightweight space telescope. A parametric modeling approach allows identifying the uncertainties and flexibilities embedded in complex systems at an early stage in the design process. Using this approach, the designer can evaluate a large number of alternative architectures quickly with a reasonable degree of fidelity, and identify families of favorable architectures that are likely to fulfill the mission requirements. The MOST model is built using MATLAB, a popular engineering software. All the parametric inputs to the model are maintained in a high-level Parameters module. This Parameters module contains all the design variables, material constants, and declaration variables (for example, mirror type declaration variables: 'mono' or 'hex') needed to create a complete space telescope model. Once given the parametric inputs, the MOST model creates a structural finite element model (FEM). A modal analysis is then performed on the structural model using NASTRAN [14], and modal frequencies and shapes for the model are obtained. The DOCS (Disturbance, Optics, Controls, and Structures) integrated modeling toolbox [15] then creates an integrated state space model, and various analyses, such as uncertainty analysis under the influence of disturbances, are performed. ZEMAX [36] is used for optics model development. The optimization function in ZEMAX provides the optimized prescriptions for the optical components of a telescope such as radius of curvature and diameter for the primary mirror. ZEMAX is also used to calculate the wave front error at the exit pupil of the telescope, and this error can be fed back to the DOCS to perform active optical control. Figure 5-1 illustrates the model creation process.

The MOST model is created based on a modular framework. Each of the submodels, such as the finite element model and the disturbance model, are created

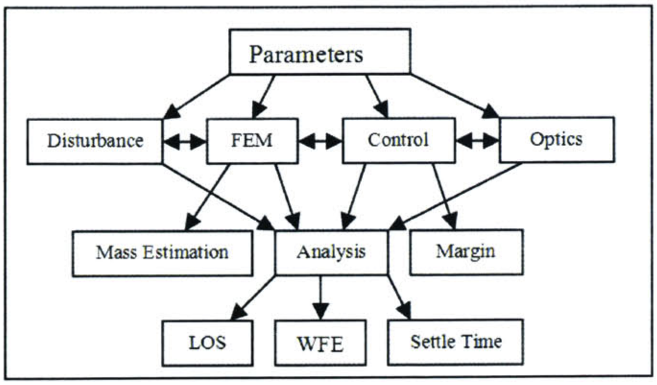

Figure 5-1: Schematic of MOST model creation process [23]

within separate modules. High-level functions pass appropriate parameters to lower-level functions using variable names defined in the Parameters module, which allows users to make changes to the model by just changing the values and type declarations in the Parameters module without full knowledge of each low level function. Also, the modular framework adds the expendability to the model. As more subsystems are developed, the model can be extended without any conflicts by simply adding modules. The entire model creation process is automated, enabling users to explore alternative architectures quickly. Figure 5-2 shows two potential telescope architectures generated with the parametric integrated modeling tool.

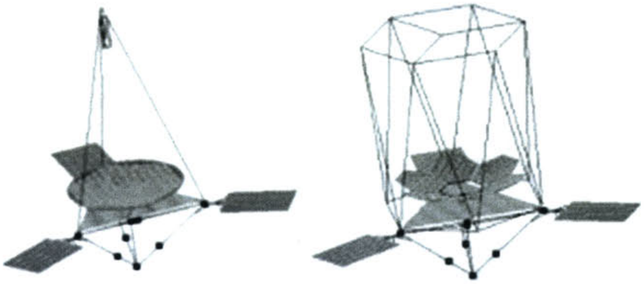

Figure 5-2: Two telescope architectures generated using the parametric integrated modeling tool: (Left) architecture with annular monolith primary mirror and tetrahedral secondary support tower, (Right) architecture with segmented hexagonal primary mirror and hexapod secondary support tower

5.2 Optics Model Development

This section focuses on the development of the optics model, one of the sub-models that constitute the MOST model described in the previous section. Line of sight jitter and wave front error are the optical performance metrics used. The line of sight jitter is computed using first order approximations dependent on the displacements of primary mirror, secondary mirror, and fast steering mirror. For the wave front error calculation, two different methods can be used: root sum square of the displacements of 20 sample points on the primary mirror for a coarse approximation, and a Zernike sensitivity analysis for a finer approximation.

5.2.1 Coarse Calculations of Optical Performance Metrics

The two optical performance outputs created in the integrated state space model are line of sight jitter and wave front error. This section presents the equations used for the coarse approximations of the two optical outputs.

The line of sight (LOS) jitter is computed using first-order optical performance approximations dependent on rotations and translations of three points: a point on the primary mirror, a point on the secondary mirror, and a point on the fast steering mirror. The following equations, originally developed by C. Perrygo and R. Burg [30], are used to compute the line of sight jitter.

$$LOS_x = -\frac{1}{f_1}\delta_{P_y} + \frac{(M-1)}{Mf_1}\delta_{S_y} + \frac{1}{Mf_1}\delta_{F_y} + 2\alpha_{P_x} - \frac{2}{M+1}\alpha_{S_x} - \frac{2}{M+1}\alpha_{F_x} \tag{5.1}$$

$$LOS_y = -\frac{1}{f_1}\delta_{P_x} + \frac{(M-1)}{Mf_1}\delta_{S_x} + \frac{1}{Mf_1}\delta_{F_x} + 2\alpha_{P_y} - \frac{2}{M+1}\alpha_{S_y} - \frac{2}{M+1}\alpha_{F_y} \tag{5.2}$$

where f_1 is the focal length of the primary mirror, f_2 is the focal length of the secondary mirror, M is the secondary mirror magnification. δ are the translations, and α are the rotations of points on the primary mirror (P), secondary mirror (S), and fast steering mirror (F). All calculations assume small displacements.

For the coarse approximation of the wave front error (WFE), the root sum square of the z-direction translations of 20 sample points located across the primary mirror is used. Note that +z-direction points from the primary mirror to the secondary mirror in the optical axis of the telescope.

$$WFE = \sqrt{\sum_{i=1}^{n} z_i^2} \tag{5.3}$$

Using only 20 sample points on the primary mirror for the wave front error calculation is obviously a very coarse approximation, which merely serves the purpose of providing a rough indicator on the optical performance of the model. For more accurate wave front error calculation, a linear model developed using a Zernike basis can be used.

5.2.2 Linear Optical Model Development Using a Zernike Basis

The ideal way to measure the wave front error would be to partition each of the optical surfaces (primary mirror, secondary mirror, etc.) into a dense grid of points (say 100x100), and compute how the wave front error changes with displacements of each grid. For example, one can create a sensitivity matrix S, and compute the optical path difference ϵ by combining the contributions from the displacements q of all the grid points.

$$\epsilon = \epsilon_{tel} + Sq + (higher\ order\ terms) \tag{5.4}$$

$$S = \begin{bmatrix} \left.\frac{\delta\epsilon_1}{\delta q_1}\right|_{q_1=0} & \cdots & \left.\frac{\delta\epsilon_1}{\delta q_m}\right|_{q_m=0} \\ \cdots & \left.\frac{\delta\epsilon_i}{\delta q_k}\right|_{q_k=0} & \cdots \\ \left.\frac{\delta\epsilon_n}{\delta q_1}\right|_{q_1=0} & \cdots & \left.\frac{\delta\epsilon_n}{\delta q_m}\right|_{q_m=0} \end{bmatrix} \tag{5.5}$$

where ϵ_{tel} is a constant offset containing the intrinsic aberrations.

However, due to the limitation of the currently available processing power, the approach of directly relating the grid point displacements to the calculation of OPD at each grid location would require a prohibitively long computational time. As an alternative approach, George Z. Angeli of AURA New Initiatives Office and Brooke Gregory of Cerro Tololo Inter-American Observatory proposed a method for calculating the wave front error based on a linear optical model developed using a Zernike basis [13].

The mirror deformations in the z-direction, the direction of the optical axis of the telescope, can be described in terms of a Zernike basis as shown in Equation 5.6.

$$\delta z = \begin{bmatrix} \delta z_1 \\ \vdots \\ \vdots \\ \delta z_i \\ \vdots \\ \vdots \\ \delta z_n \end{bmatrix} = \Gamma a = [\gamma_0 \ \ \gamma_1 \ \ \dots \ \ \gamma_m] \begin{bmatrix} a_0 \\ a_1 \\ \vdots \\ \vdots \\ a_m \end{bmatrix} = \begin{bmatrix} \Upsilon_{01} & \Upsilon_{11} & \dots & \Upsilon_{m1} \\ \vdots & \vdots & \vdots & \vdots \\ \Upsilon_{0n} & \Upsilon_{1n} & \dots & \Upsilon_{mn} \end{bmatrix} \begin{bmatrix} a_0 \\ a_1 \\ \vdots \\ \vdots \\ a_m \end{bmatrix} \tag{5.6}$$

where γ_i are the Zernike functions, Υ_{ij} are the discretizations of each of the Zernike functions on the same grid as the deformation, and a_i are the Zernike coefficients.

Now the mirror displacements q, including de-centers (dc_x, dc_y), can be expressed as in Equation 5.7. Note that the coefficients $\sqrt{N}$ are needed to preserve the orthonormality of the original Zernike basis (N is the number of grid points used).

$$q = \begin{bmatrix} dc_x \\ dc_y \\ \delta z_1 \\ \vdots \\ dc_x \\ dc_y \\ \delta z_i \\ \vdots \\ dc_x \\ dc_y \\ \delta z_n \end{bmatrix} = \begin{bmatrix} \frac{1}{\sqrt{N}} & 0 & 0 & \ldots & 0 \\ 0 & \frac{1}{\sqrt{N}} & 0 & \ldots & 0 \\ 0 & 0 & \Upsilon_{01} & \ldots & \Upsilon_{m1} \\ \vdots & \vdots & \vdots & \ldots & \vdots \\ \frac{1}{\sqrt{N}} & 0 & 0 & \ldots & 0 \\ 0 & \frac{1}{\sqrt{N}} & 0 & \ldots & 0 \\ 0 & 0 & \Upsilon_{0i} & \ldots & \Upsilon_{mi} \\ \vdots & \vdots & \vdots & \ldots & \vdots \\ \frac{1}{\sqrt{N}} & 0 & 0 & \ldots & 0 \\ 0 & \frac{1}{\sqrt{N}} & 0 & \ldots & 0 \\ 0 & 0 & \Upsilon_{0n} & \ldots & \Upsilon_{mn} \end{bmatrix} \begin{bmatrix} \sqrt{N} dc_x \\ \sqrt{N} dc_y \\ a_0 \\ \vdots \\ a_m \end{bmatrix} = \hat{\Gamma} \hat{a} \tag{5.7}$$

Then, Equation 5.4 can be rewritten in terms of a Zernike basis,

$$\epsilon_{exit} = \epsilon_{tel} + S_p \hat{\Gamma}_p \hat{a}_p + S_s \hat{\Gamma}_s \hat{a}_s \tag{5.8}$$

where the sensitivity matirx is partitioned into contributions from the primary (p) and secondary (s) mirrors.

The exit pupil OPD can also be expanded on a Zernike basis as the following:

$$\epsilon_{exit} = \Gamma_{exit} a_{exit} \tag{5.9}$$

The Zernike coefficients for the exit pupil OPD, a_{exit}, can be expressed as linear combinations of the extended Zernike coefficients $\hat{a}_p$ and $\hat{a}_s$ of the primary and secondary mirror deformation.

$$a_{exit} \approx a_{tel} + \hat{S}_p \hat{a}_p + \hat{S}_s \hat{a}_s \tag{5.10}$$

where,

$$\hat{S}_p = \Gamma^T_{exit} S_p \hat{\Gamma}_p \tag{5.11}$$

$$\hat{S}_s = \Gamma^T_{exit} S_s \hat{\Gamma}_s \tag{5.12}$$

a_{exit} denotes the Zernike expansion of the intrinsic aberrations of the un-deformed telescope. $\hat{S}_p$ and $\hat{S}_s$ are the Zernike sensitivity matrices that describe how the changes in each Zernike coefficient for each optical surface affect the Zernike coefficients for the exit pupil OPD.

Since the FEM module in the MOST model provides the modal frequencies and shapes for the structural model of the telescope, the mirror deformations q are expressed using modal superposition,

$$q = \Phi q_m \tag{5.13}$$

where Φ is the eigenvector matrix containing the modes as columns and q_m is a column vector containing the modal coordinates.

If the output of the optical model is defined as the Zernike decomposition of the exit pupil OPD a_{exit}, the optical output matrix C of the telescope state space representation can be written as follows,

$$C = (\hat{S}_p \hat{\Gamma}_p{}^T \Phi_p + \hat{S}_s \hat{\Gamma}_s{}^T \Phi_s)[I \quad 0] \tag{5.14}$$

where the states X are defined in terms of the modal coordinates:

$$X = [q_m^T \quad \dot{q_m}^T]^T \tag{5.15}$$

Once the Zernike coefficients for the exit pupil OPD are obtained, the RMS wave front error σ can be obtained as a weighted sum of the Zernike coefficient squares.

$$\sigma \simeq \sqrt{\sum_{j=1}^{N} w_j^2 a_{exit\ j}^2} \tag{5.16}$$

The expressions and the associated weights for the Fringe Zernike terms are given in Table 5.1.

Term Number	Term Function	Weight
1	1	
2	$\rho \cos \phi$	$\frac{1}{\sqrt{4}}$
3	$\rho \sin \phi$	$\frac{1}{\sqrt{4}}$
4	$2\rho^2 - 1$	$\frac{1}{\sqrt{3}}$
5	$\rho^2 \cos 2\phi$	$\frac{1}{\sqrt{6}}$
6	$\rho^2 \sin 2\phi$	$\frac{1}{\sqrt{6}}$
7	$(3\rho^3 - 2\rho) \cos \phi$	$\frac{1}{\sqrt{8}}$
8	$(3\rho^3 - 2\rho) \sin \phi$	$\frac{1}{\sqrt{8}}$
9	$6\rho^4 - 6\rho^2 + 1$	$\frac{1}{\sqrt{5}}$

Table 5.1: Zernike functions and weights for the first nine fringe Zernike terms [2]

The Zernike sensitivity matrices, $\hat{S}_p$ and $\hat{S}_s$, are significantly smaller than the full deformation sensitivity matrix, S_p and S_s. The more Zernike terms are used, the larger the Zernike sensitivity matrices will be, but still far smaller than the full deformation sensitivity matrix, thus providing an efficient way of calculating the wave front error. Also it was shown that the amplitude of the error between the wave front error obtained using the linear optical model described and the wave front error obtained through a direct ray tracing is less than 1 nm for realistic deformation cases of a 30 m telescope[13]. Thus, the MOST model uses the linear optical model developed using a Zernike basis for efficient and accurate calculation of the wave front error.

5.2.3 Sample Zernike Sensitivity Analysis

In order to use the linear optical model described in the previous section, the Zernike sensitivity matrices, $\hat{S}_p$ and $\hat{S}_s$, have to be first obtained. The Zernike sensitivity matrices relate the Zernike coefficients for the deformation of each optical surface to the Zernike coefficients of the exit pupil OPD, describing how the changes in each Zernike coefficient for each optical surface affect the Zernike coefficients for the exit pupil OPD. The Zernike sensitivity matrix for the primary mirror, $\hat{S}_p$, has the form shown in Equation 5.17.

$$\begin{bmatrix} a_{exit_1} \\ \vdots \\ a_{exit_i} \\ \vdots \\ a_{exit_m} \end{bmatrix} = \hat{S}_p a_p = \begin{bmatrix} \frac{a_{exit_1}}{a_{p1}} & \frac{a_{exit_1}}{a_{p2}} & \cdots & \frac{a_{exit_1}}{a_{pm}} \\ \vdots & \vdots & \cdots & \vdots \\ \frac{a_{exit_i}}{a_{p1}} & \frac{a_{exit_i}}{a_{p2}} & \cdots & \frac{a_{exit_i}}{a_{pm}} \\ \vdots & \vdots & \cdots & \vdots \\ \frac{a_{exit_m}}{a_{p1}} & \frac{a_{exit_m}}{a_{p2}} & \cdots & \frac{a_{exit_m}}{a_{pm}} \end{bmatrix} \begin{bmatrix} a_{p1} \\ \vdots \\ a_{pi} \\ \vdots \\ a_{pm} \end{bmatrix} \tag{5.17}$$

where a_{exit} is the Zernike decomposition of the exit pupil OPD, a_p is the Zernike decomposition of the primary mirror deformations. The decenter terms are not included for simplicity.

In order to compute the Zernike sensitivity matrices, the MOST model uses an optical design program called ZEMAX. ZEMAX first sets each optical surface type to “Zernike Fringe Surface”. Then, the elements of the Zernike sensitivity matrices are obtained by introducing deformations to the Zernike coefficients of each optical surface, term-by-term, and by looking, at the same time, at the corresponding changes on the Zernike coefficients for the exit pupil OPD. To estimate the derivatives, for each mirror deformation Zernike term, 3 different deformation amplitudes (0 μm, 1μm, and 2 μm) are applied. Then, the resulting Zernike coefficients for the exit pupil OPD are fitted with quadratic curves to obtain the elements of the Zernike sensitivity matrix.

A sample Zernike sensitivity matrix generation for the primary mirror deformations on a 30 m telescope is given in the following. Table 5.2 shows the optical prescription used to build a telescope model in ZEMAX.

Primary Mirror (PM) Dia.	30 m
Secondary Mirror (SM) Dia.	2 m
Conic Constant for PM	-1.001891
Conic Constant for SM	-1.221152
Radius of Curvature for PM	-60.046675
Radius of Curvature for SM	-4.229739
PM-SM separation	28 m
Image Plane Location	18.75 m behind PM

Table 5.2: Telescope parameters used for sample Zernike sensitivity matrix creation

The values in Table 5.2 were put into the Lens Data Editor in ZEMAX and a telescope model was created as shown in Figure 5-3.

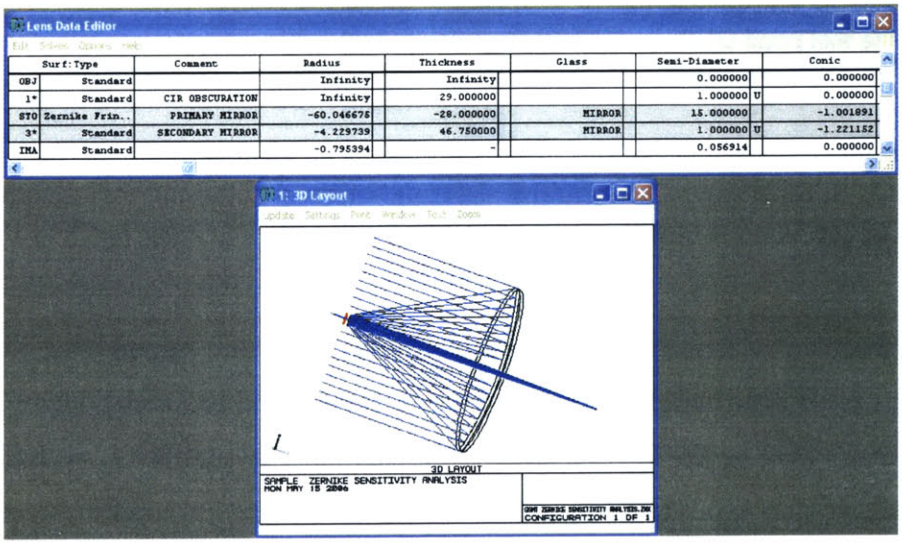

Surf:Type		Comment	Radius	Thickness	Glass	Semi-Diameter		Conic
OBJ	Standard		Infinity	Infinity		0.000000		0.000000
1*	Standard	CIR OBSCURATION	Infinity	29.000000		1.000000	U	0.000000
STO	Zernike Frin..	PRIMARY MIRROR	-60.046675	-28.000000	MIRROR	15.000000		-1.001891
3*	Standard	SECONDARY MIRROR	-4.229739	46.750000	MIRROR	1.000000	U	-1.221152
IMA	Standard		-0.795394	-		0.056914		0.000000

SAMPLE ZERNIKE SENSITIVITY ANALYSIS
MON MAY 15 2006

CONFIGURATION 1 OF 1

Figure 5-3: Telescope model creation in ZEMAX

Using the Extra Data Editor, each Zernike coefficient for the primary mirror was perturbed by 0 μm, 1μm, and 2 μm, and the corresponding changes in the Zernike coefficients for the exit pupil OPD were recorded as shown in Figure 5-4. In the calculation of the Zernike coefficients for the exit pupil OPD, the first nine fringe Zernike terms given in Table 5.1 were used and a sampling grid of 128x128 was used.

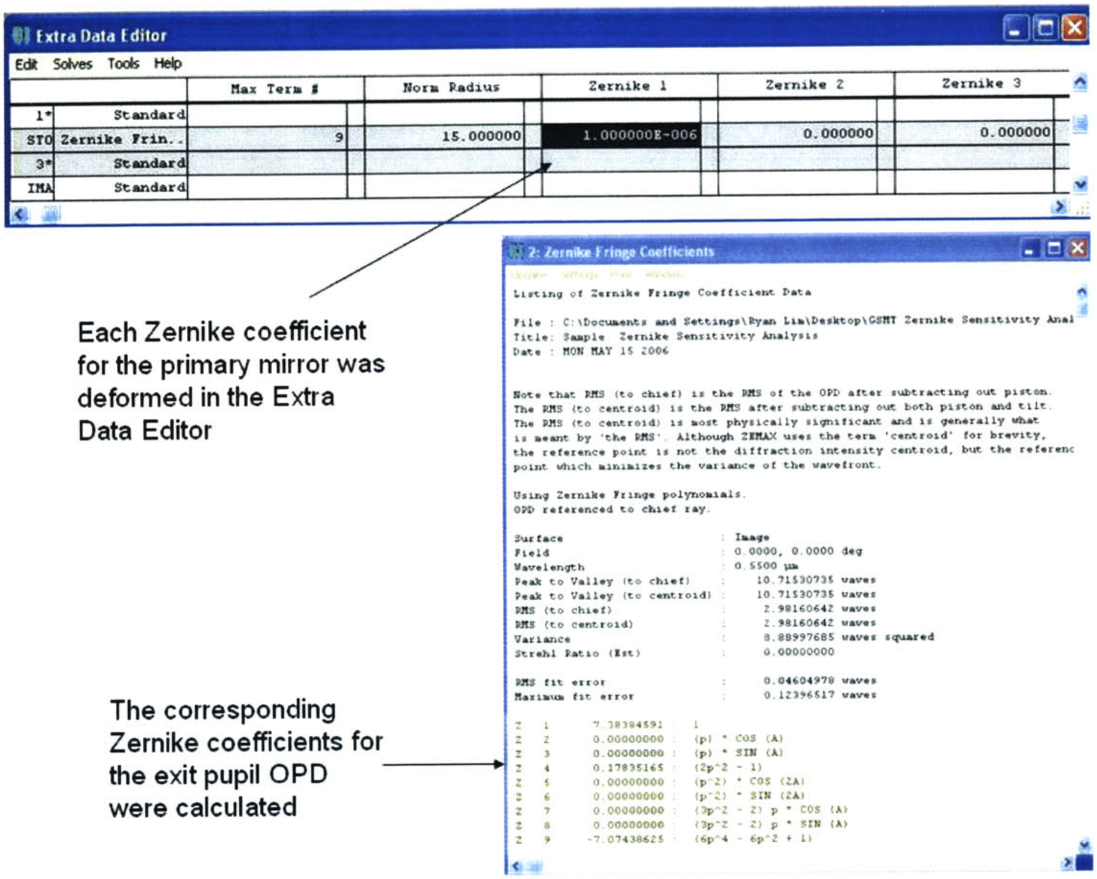

		Max Term #	Norm Radius	Zernike 1	Zernike 2	Zernike 3
1*	Standard					
STO	Zernike Frin..	9	15.000000	1.000000E-006	0.000000	0.000000
3*	Standard					
IMA	Standard					

```
Listing of Zernike Fringe Coefficient Data

File : C:\Documents and Settings\Ryan Lim\Desktop\GSMT Zernike Sensitivity Anal
Title: Sample  Zernike Sensitivity Analysis
Date : MON MAY 15 2006


Note that RMS (to chief) is the RMS of the OPD after subtracting out piston.
The RMS (to centroid) is the RMS after subtracting out both piston and tilt.
The RMS (to centroid) is most physically significant and is generally what
is meant by 'the RMS'. Although ZEMAX uses the term 'centroid' for brevity,
the reference point is not the diffraction intensity centroid, but the referenc
point which minimizes the variance of the wavefront.

Using Zernike Fringe polynomials.
OPD referenced to chief ray.

Surface                         : Image
Field                           : 0.0000, 0.0000 deg
Wavelength                      : 0.5500 µm
Peak to Valley (to chief)       :    10.71530735 waves
Peak to Valley (to centroid)    :    10.71530735 waves
RMS (to chief)                  :     2.98160642 waves
RMS (to centroid)               :     2.98160642 waves
Variance                        :     8.88997685 waves squared
Strehl Ratio (Est)              :     0.00000000

RMS fit error                   :     0.04604978 waves
Maximum fit error               :     0.12396517 waves

Z   1       7.38384591 :  1
Z   2       0.00000000 :  (p) * COS (A)
Z   3       0.00000000 :  (p) * SIN (A)
Z   4       0.17835165 :  (2p^2 - 1)
Z   5       0.00000000 :  (p^2) * COS (2A)
Z   6       0.00000000 :  (p^2) * SIN (2A)
Z   7       0.00000000 :  (3p^2 - 2) p * COS (A)
Z   8       0.00000000 :  (3p^2 - 2) p * SIN (A)
Z   9      -7.07438625 :  (6p^4 - 6p^2 + 1)
```

Figure 5-4: Introducing primary mirror deformations and obtaining the corresponding changes in the Zernike coefficients for the exit pupil OPD

The Zernike coefficients for the exit pupil OPD obtained by applying the three different mirror deformations were fitted using the method of Least-Squares to produce the elements in the Zernike sensitivity matrix. For simplicity, no rigid body deformations were applied and therefore, the decenter terms were not included in the Zernike sensitivity matrix. Figure 5-5 shows the Zernike sensitivity matrix obtained for the telescope model created in ZEMAX.

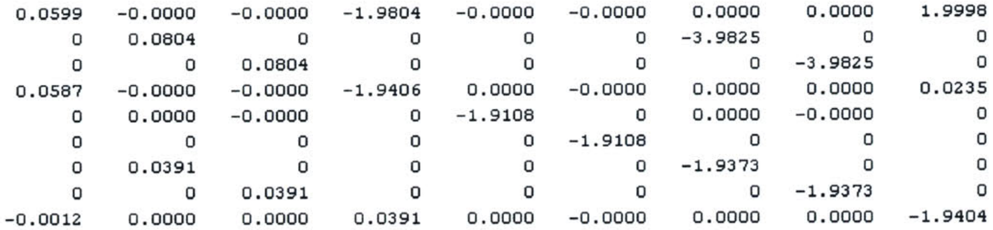

```
  0.0599   -0.0000   -0.0000   -1.9804   -0.0000   -0.0000    0.0000    0.0000    1.9998
       0    0.0804         0         0         0         0   -3.9825         0         0
       0         0    0.0804         0         0         0         0   -3.9825         0
  0.0587   -0.0000   -0.0000   -1.9406    0.0000   -0.0000    0.0000    0.0000    0.0235
       0    0.0000   -0.0000         0   -1.9108         0    0.0000   -0.0000         0
       0         0         0         0         0   -1.9108         0         0         0
       0    0.0391         0         0         0         0   -1.9373         0         0
       0         0    0.0391         0         0         0         0   -1.9373         0
 -0.0012    0.0000    0.0000    0.0391    0.0000   -0.0000    0.0000    0.0000   -1.9404
```

Figure 5-5: Sample Zernike sensitivity matrix obtained for the primary mirror deformations using the telescope model given in Figure 5-3

The Zernike sensitivity matrix obtained in Figure 5-5 was compared with the Zernike sensitivity matrix obtained by George Z. Angeli for the Thirty Mirror Telescope project [1], [13] in order to provide a rough check on the validity of the sample Zernike sensitivity matrix created.

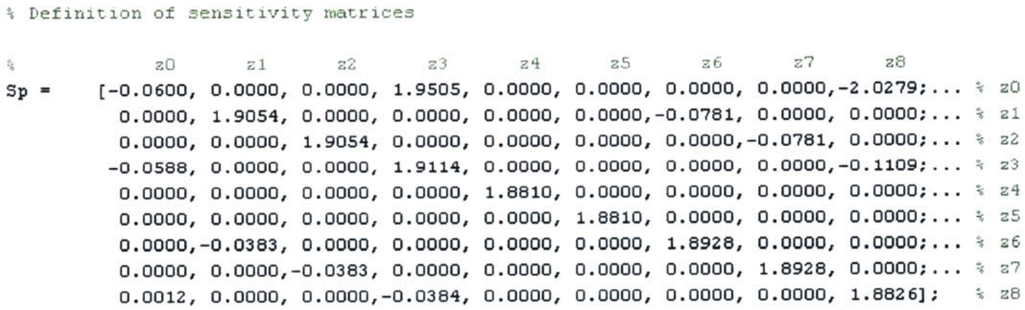

```
% Definition of sensitivity matrices

%           z0       z1       z2       z3       z4       z5       z6       z7       z8
Sp =    [-0.0600, 0.0000, 0.0000, 1.9505, 0.0000, 0.0000, 0.0000, 0.0000,-2.0279;... % z0
          0.0000, 1.9054, 0.0000, 0.0000, 0.0000, 0.0000,-0.0781, 0.0000, 0.0000;... % z1
          0.0000, 0.0000, 1.9054, 0.0000, 0.0000, 0.0000, 0.0000,-0.0781, 0.0000;... % z2
         -0.0588, 0.0000, 0.0000, 1.9114, 0.0000, 0.0000, 0.0000, 0.0000,-0.1109;... % z3
          0.0000, 0.0000, 0.0000, 0.0000, 1.8810, 0.0000, 0.0000, 0.0000, 0.0000;... % z4
          0.0000, 0.0000, 0.0000, 0.0000, 0.0000, 1.8810, 0.0000, 0.0000, 0.0000;... % z5
          0.0000,-0.0383, 0.0000, 0.0000, 0.0000, 0.0000, 1.8928, 0.0000, 0.0000;... % z6
          0.0000, 0.0000,-0.0383, 0.0000, 0.0000, 0.0000, 0.0000, 1.8928, 0.0000;... % z7
          0.0012, 0.0000, 0.0000,-0.0384, 0.0000, 0.0000, 0.0000, 0.0000, 1.8826];   % z8
```

Figure 5-6: Zernike sensitivity matrix created by George Z. Angeli [1] for the Thirty Mirror Telescope project

As can be seen in Figure 5-5 and 5-6, the two Zernike sensitivity matrices roughly match their patterns; that is, they have zero entries at the common places and the same order of magnitudes for each non-zero entry. The sign mismatches in the entries might have been caused by the different sign conventions that George Z. Angeli and ZEMAX used. The exact parameters used for the creation of the Zernike sensitivity matrix in Figure 5-6 were not available, and therefore, the matrix in Figure 5-6 cannot be used as the absolute truth measure for the validity of the sample Zernike sensitivity matrix created. However, based on the pattern matching, it can be inferred that the Zernike sensitivity matrix creation using ZEMAX produces correct results.

5.2.4 ZEMAX-MATLAB Interface

As mentioned in Section 5.1, the MOST model has been developed using MATLAB as its platform. In order to fully integrate the optics model into the MOST model, first, an interface between ZEMAX and MATLAB had to be established. The communication between ZEMAX and MATLAB is accomplished using Dynamic Data Exchange (DDE). DDE is a protocol defined within the Windows operation system for sharing data between programs [31]. Two programs can establish a DDE link, with one program acting as the "server" and the other as the "client". The client generally requests specific data from the server, and the server sends the data back to the client. To establish the interface between ZEMAX and MATLAB, ZEMAX was made as the server and MATLAB as the client.

MATLAB first sends the telescope prescriptions set in the Parameters module of the MOST model to ZEMAX. Once ZEMAX receives the telescope prescriptions, it builds a telescope model and performs the Zernike sensitivity analysis described in the previous section. The resulting Zernike sensitivity matrix is fed back to MATLAB for the wave front error calculation and further analysis. Figure 5-7 illustrates the DDE communication between ZEMAX and MATLAB. An example of a successful DDE communication is given in Figure 5-8. Note that in Figure 5-8, the calculation of the fringe Zernike coefficients was performed in ZEMAX, and the results were transmitted to MATLAB. Note that the ZEMAX-MATLAB interface successfully transmitts the results and MATLAB displays the same results as seen in ZEMAX. A sample MATLAB code for changing the curvature of the primary mirror is given in Figure 5-9.

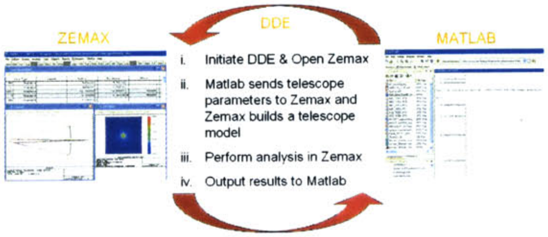

i. Initiate DDE & Open Zemax
ii. Matlab sends telescope parameters to Zemax and Zemax builds a telescope model
iii. Perform analysis in Zemax
iv. Output results to Matlab

Figure 5-7: Data communication between ZEMAX and MATLAB using DDE

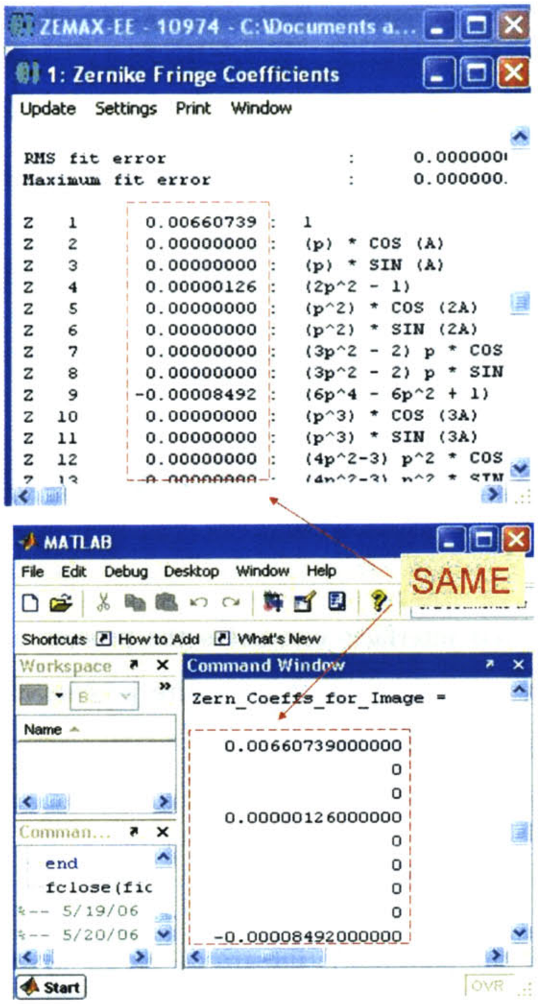

```
RMS fit error                     :    0.000000
Maximum fit error                 :    0.000000.

Z   1        0.00660739 :  1
Z   2        0.00000000 :  (p) * COS (A)
Z   3        0.00000000 :  (p) * SIN (A)
Z   4        0.00000126 :  (2p^2 - 1)
Z   5        0.00000000 :  (p^2) * COS (2A)
Z   6        0.00000000 :  (p^2) * SIN (2A)
Z   7        0.00000000 :  (3p^2 - 2) p * COS
Z   8        0.00000000 :  (3p^2 - 2) p * SIN
Z   9       -0.00008492 :  (6p^4 - 6p^2 + 1)
Z  10        0.00000000 :  (p^3) * COS (3A)
Z  11        0.00000000 :  (p^3) * SIN (3A)
Z  12        0.00000000 :  (4p^2-3) p^2 * COS
```

```
  end
  fclose(fic
%-- 5/19/06
%-- 5/20/06
```

```
Zern_Coeffs_for_Image =

     0.00660739000000
                    0
                    0
     0.00000126000000
                    0
                    0
                    0
                    0
    -0.00008492000000
```

Figure 5-8: An example of a successful DDE communication: (Top) ZEMAX calculates the Zernike coefficients for the exit pupil and sends the data to MATLAB through the DDE interface created, (Bottom) MATLAB receives the data and stores them in a vector.

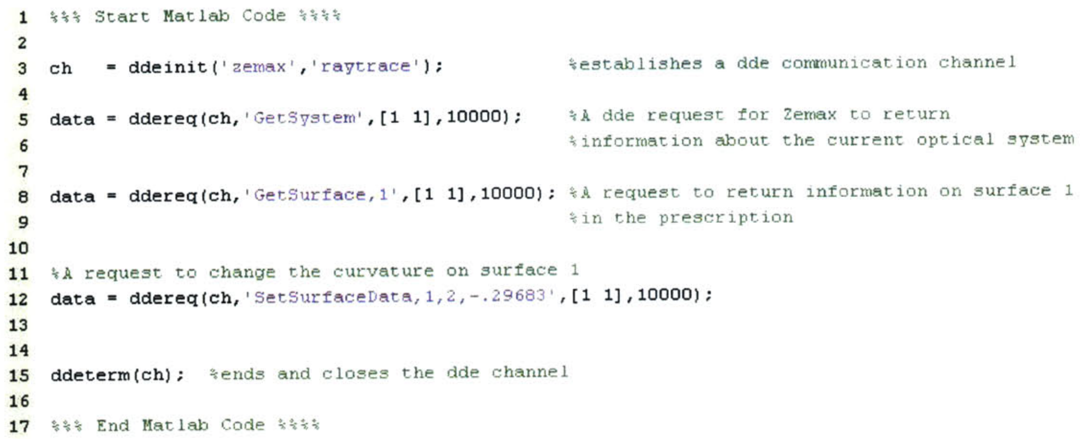

```
%%% Start Matlab Code %%%%

ch   = ddeinit('zemax','raytrace');           %establishes a dde communication channel

data = ddereq(ch,'GetSystem',[1 1],10000);    %A dde request for Zemax to return
                                              %information about the current optical system

data = ddereq(ch,'GetSurface,1',[1 1],10000); %A request to return information on surface 1
                                              %in the prescription

%A request to change the curvature on surface 1
data = ddereq(ch,'SetSurfaceData,1,2,-.29683',[1 1],10000);


ddeterm(ch);  %ends and closes the dde channel

%%% End Matlab Code %%%%
```

Figure 5-9: Sample MATLAB code used in the ZEMAX-MATLAB interface. The code sets the radius of curvature for the primary mirror

The ZEMAX-MATLAB interface automates the process of performing Zernike sensitivity analysis. In turn, this makes the entire process of model creation and analysis in the MOST model automated.

5.3 Chapter Summary

This chapter described the parametric integrated model developed for the MOST project. A brief overview of the entire MOST model was provided. The line of sight jitter and the wave front error were introduced as the two optical performance metrics, and the expressions for the coarse approximations of the two metrics were provided. For more accurate calculation of the wave front error, the linear optical model developed using a Zernike basis was introduced. A sample Zernike sensitivity analysis was performed using ZEMAX, and it was inferred that ZEMAX produces correct Zernike sensitivity matrices when the results obtained by ZEMAX were compared with the hi-fidelity results developed for the Thirty Meter Telescope project. The work done on establishing the data interface between ZEMAX and MATLAB was also described.

Chapter 6

Conclusion

6.1 Thesis Summary

This thesis explored two different technologies that have the potential to contribute in improving the performance of space imaging systems. Chapters 2 through 4 described the first technology, the precision pointing control technology, which can be used to realize space imaging systems with a longer baseline such as a formation flying interferometer. Chapter 5 described the second technology, parametric integrated modeling, which provides a design tool to explore a wide variety of different telescope architectures at an early stage of the design lifecycle.

Chapter 2 gave an overview of the SPHERES testbed and the SPHERES Position Attitude Determination System (PADS). The limitations of the SPHERES PADS were described, and the concepts for precision pointing control were introduced as the ways to overcome the limitations posed by the SPHERES PADS. Three possible concepts were introduced for precision pointing control: the Sub Aperture Metrology (SAM), the Full Aperture Metrology (FAM), and the Hybrid Metrology (HM). The SAM concept was chosen for further analysis due to its simplicity. A ray tracing analysis was performed on the SAM concept using the the geometrical optics approximations. Based on the ray tracing results, it was determined that the original concept developed for SAM was not appropriate for an actual prototype development. Therefore, the original SAM concept was modified to include a transparent screen in the optical train. The modified concept was chosen for the development of a prototype named the "Precision Pointing Optical Payload (PPOP)."

Chapter 3 discussed the prototype development of the PPOP. Each of the optical components as well as the avionics that constitute the PPOP were described.

Chapter 4 presented the results from pointing control experiments. Three types of experiments were performed: coarse pointing control using the SPHERES global metrology, fine pointing control using the fast steering mirrors in the PPOP, and staged control using both coarse and fine control. Notable improvements in the performance were delivered by staged pointing control when compared with the performance provided by coarse pointing control. However, staged pointing control performance was not as good as the performance provided by fine control, and suggestions for the controller improvements were made.

Chapter 5 provided an overview of the parametric integrated model developed for a Modular Optical Space Telescope (MOST). The optics model was discussed in detail which included the description of the linear optical model developed using a Zernike basis. A data interface was established between ZEMAX and MATLAB using Windows Dynamic Data Exchange. With the ZEMAX-MATLAB interface, the model creation process of the MOST model can be completely automated.

6.2 Contributions

This thesis made the following contributions:

- The concept developments for precision pointing control technology.
- The development of a complete ray tracing analysis using the geometrical optics approximations.
- The design and fabrication of the Precision Pointing Optical Payload (PPOP) that provides fine pointing control.
- The demonstration of staged pointing control using the SPHERES global metrology system and the fast steering mirrors in the PPOP.

- An overview of the parametric integrated model for a Modular Optical Space Telescope, which provides a design tool for building complex space imaging systems.
- An introduction to the linear optical model development using a Zernike basis.
- The development of the data interface between ZEMAX and MATLAB, which makes the entire model creation process in the MOST model fully automated.

6.3 Recommendations for Future Work

The current design of the PPOP represents the first prototype built, and many modifications could be made to improve the performance of the staged pointing control.

First of all, a more advanced control algorithm needs to be developed. The effects of aberrations and diffraction could be added to the ray tracing analysis in order to provide a high fidelity optics model. The thruster firings could be modeled and added as a part of the control loop. The time variant nature of the system shown in Figure 4-20 also needs to be taken into consideration. A more efficient centroid calculation algorithm and a more optimized code structure would increase the control bandwidth and thus would improve the overall performance of the controller.

Hardware could also be improved. The PPOP can be made lighter using materials such as Lexan. By making PPOP lighter, the control load on the SPHERES global metrology system could be reduced. Higher quality optical components as well as better sizing of the optical components could improve the performance of the PPOP. For example, a larger beam splitter could be used to allow more retroreflector offset, and an array of small retroreflectors could be used to reduce the magnitude of the offset the current retroreflector produces.

The next step of the PPOP would be to perform staged pointing maneuvers using multiple Spheres in formation flying. Also the transparent screen needs to be removed, and the precision pointing maneuvers need to be demonstrated using the various concepts described in Section 2.3. Once staged pointing control without the transparent screen is achieved, the work can be expanded to do path length control using optical delay lines to form interference fringes. Two possible concepts are shown in Figure 6-1.

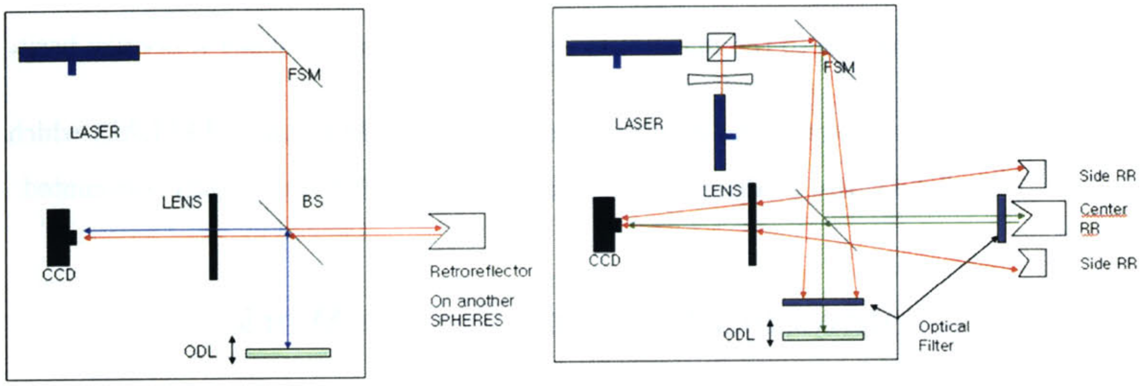

Figure 6-1: Concepts for path length control with optical delay line

The parametric integrated model for a Modular Optical Space Telescope is still under development and requires further refinement. The scheme for active optical control needs to be developed, and the optical models for various telescope configurations, such as Golay 3, have to be developed in Zemax. More sub-models (e.g. Thermal Model) need to be added to the MOST model to better represent real space imaging systems. A testbed is currently scheduled to be developed. Once the testbed is built, model validations will be performed to build confidence in the results.

Appendix A

Calculation of Allowable Mirror Actuation Angle with Consideration of Misalignments

The ray tracing analysis given in Section 2.4 is based on the assumption that the center of the beam splitter and the center of the retroreflector lie on the same axis; in other words, two operating Spheres are perfectly aligned as shown in Figure 2-6. But in real operations, Spheres will not necessarily be aligned at all times. In fact, the purpose of the Precision Pointing Optical Payload is to bring misaligned Spheres to better aligned positions. This section describes the expressions developed for calculating the allowable mirror actuation angles in the case where angular and translational misalignments exist.

Two different misalignments are considered: Translational misalignment and Angular misalignment, as shown in Figure A-1.

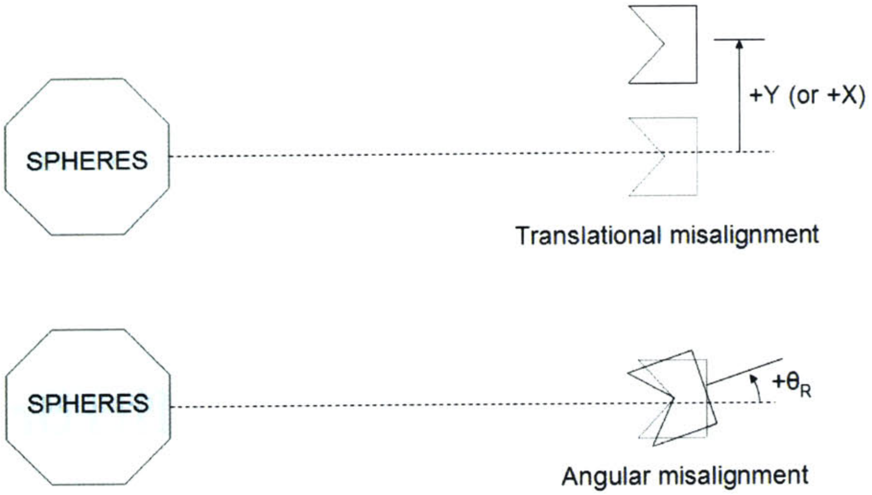

Figure A-1: Definition of misalignments

A.1 Translational Misalignment

Translational misalignment refers to the displacement offset in the Y (or X) direction from the axis that passes through the center of the beam splitter. As shown in Figure A-2, the direction of the retroreflector offset changes depending on how large the mirror actuation angle (θ_m) is.

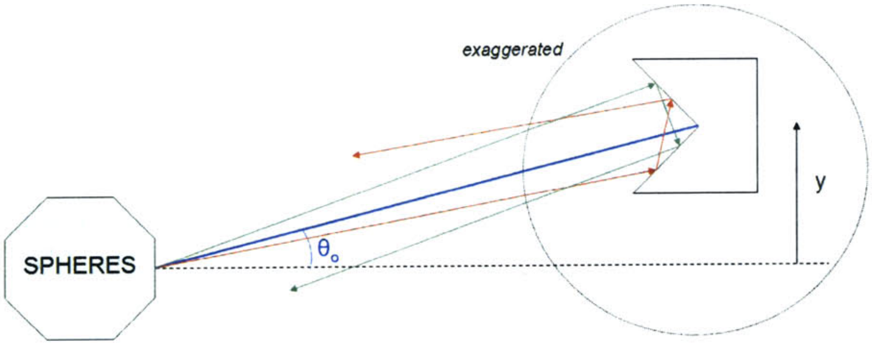

Figure A-2: Offset at retroreflector with the presence of translational misalignment

The critical value which determines the direction of the retroreflector offset is θ_o, which is equal to:

$$\theta_o = \arctan \frac{y}{R + \frac{1}{2} D_{RR}} \tag{A.1}$$

If $2\theta_m$ is larger than θ_o, then the incident beam hits the top portion the retroreflector and the offset is created downward. If $2\theta_m$ is smaller than θ_o, then the incident beam hits the bottom portion the retroreflector and the offset is created upward.

In order to determine the allowable mirror actuation angles with the presence of translational misalignments in the X and Y direction, ΔX and ΔY, the location of the beam on the beam splitter face towards the focusing lens can be first obtained using the following expressions.

If $\mid 2\theta_m \mid \; < \; \mid \theta_o \mid$:

Mirror 1:

$$v = \frac{d}{2} - k\cos\theta_{g1} + k\cos\theta_{g1}\tan\theta_{g1} + S_1 \tag{A.2}$$

Mirror 2:

$$h_{to\_lens} = h\tan 2\theta_{m2} + S_2 \tag{A.3}$$

If $\mid 2\theta_m \mid \; > \; \mid \theta_o \mid$:

Mirror 1:

$$v = \frac{d}{2} - k\cos\theta_{g1} + k\cos\theta_{g1}\tan\theta_{g1} - S_1 \tag{A.4}$$

Mirror 2:

$$h_{to\_lens} = h\tan 2\theta_{m2} - S_2 \tag{A.5}$$

Once the angle and location of the beam going towards the focusing lens are obtained, the thick lens formula (2.11, 2.12) and the tangent relations (2.15, 2.21) can be used to obtain the maximum allowable mirror actuation angles for the given translational misalignments, ΔX and ΔY.

A.2 Angular Misalignment

Positive angular misalignment is defined as the rotation about the -X axis. Angular misalignment, θ_R, creates offset at the retroreflector as shown in Figure A-3.

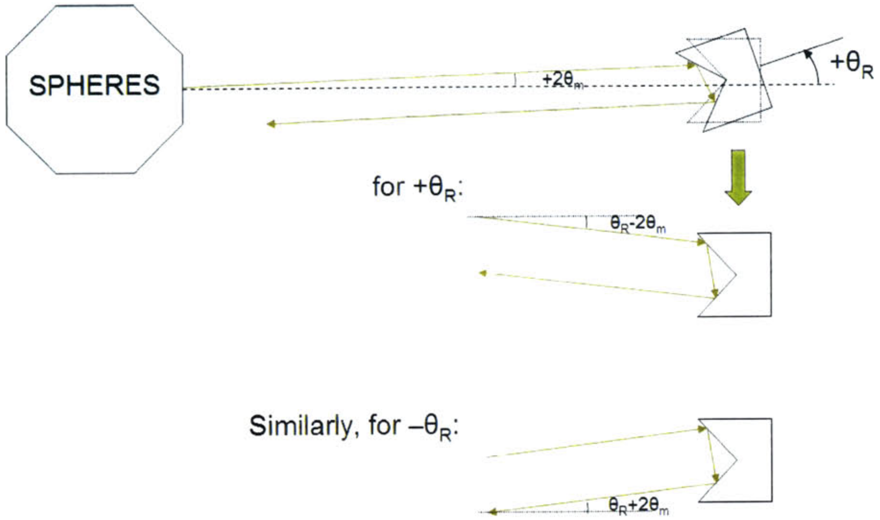

Figure A-3: Offset at retroreflector with the presence of angular misalignment

Again, the location of the beam on the beam splitter face towards the focusing lens can be first obtained using the following expressions.

Mirror 1:

$$v = \frac{d}{2} - k\cos\theta_{g1} + k\cos\theta_{g1}\tan\theta_{g1} - S_{1\_new} \tag{A.6}$$

Mirror 2:

$$h_{to\_lens} = h\tan 2\theta_{m2} - S_{2\_new} \tag{A.7}$$

The above equations are very similar to the ones used for the case with the translations misalignment, except that S_{1_new} and S_{2_new} are used instead of S_1 and S_2. S_{1_new} and S_{2_new} include the effects caused by the angular misalignment and can be calculated as following.

$$S_{1\_new} = \frac{\delta_1}{\cos\left(\theta_R - 2\theta_{m1}\frac{|\theta_R|}{\theta_R}\right)} \frac{\left|\theta_R - 2\theta_{m1}\frac{|\theta_R|}{\theta_R}\right|}{\theta_R - 2\theta_{m1}\frac{|\theta_R|}{\theta_R}} \tag{A.8}$$

$$S_{2\_new} = \frac{\delta_2}{\cos\left(\theta_R - 2\theta_{m2}\frac{|\theta_R|}{\theta_R}\right)} \frac{\left|\theta_R - 2\theta_{m2}\frac{|\theta_R|}{\theta_R}\right|}{\theta_R - 2\theta_{m2}\frac{|\theta_R|}{\theta_R}} \tag{A.9}$$

Once the angle and location of the beam going towards the focusing lens are obtained, the thick lens formula (2.11, 2.12) and the tangent relations (2.15, 2.21) can be used to obtain the maximum allowable mirror actuation angles for the given angular misalignments, θ_R.

Appendix B

Equation of Motion for Fast Steering Mirrors

The equation of motion for the fast steer mirrors can be derived using a simple spring model shown in Figure B-1, where K is the spring stiffness and D is the damping constant.

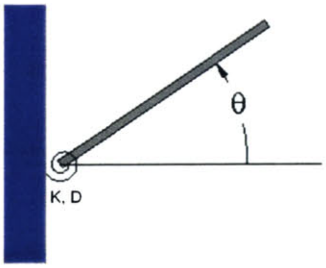

Figure B-1: Simplified model for the fast steering mirrors

Using the second order approximation, the equation of motion for the fast steering mirrors can be written as:

$$I\ddot{\theta} + D\dot{\theta} + K\theta = \tau_c. \tag{B.1}$$

where I is the mass moment of inertia of the mirror and τ_c is the torque input applied to the mirror.

If the torque input is assumed to be proportional to the current applied to the mirror,

$$\tau_c = q_c i \tag{B.2}$$

where q_c is a constant,

then, Equation (B.1) becomes,

$$\ddot{\theta} + \frac{D}{I}\dot{\theta} + \frac{K}{I}\theta = \frac{q_c}{I}i \tag{B.3}$$

The coefficients in Equation (B.3) can be found by first rearranging the variables as

$$\frac{q_c}{I} = \frac{q_c}{K}\frac{K}{I} \tag{B.4}$$

then, by comparing coefficients with the coefficients of the second order equation given in the following:

$$\ddot{\theta} + 2\xi\omega_n\dot{\theta} + \omega_n^2\theta = \frac{q_c}{I}i \tag{B.5}$$

Using the experimentally obtained values for ξ and ω_n (Section 3.1.2), first $\frac{D}{I}$ and $\frac{K}{I}$ can be obtained.

The result obtained from the mirror calibration (Section 3.1.2) can be used for $\frac{\theta}{i}$. During the calibration, $\dot{\theta}$ and $\ddot{\theta}$ were assumed to be zero. By substituting $\dot{\theta} = \ddot{\theta} = 0$ into Equation (B.3) and rearranging, the following relation can be obtained.

$$\frac{\theta}{i} = \frac{q_c}{K} \tag{B.6}$$

Now the remaining coefficient $\frac{q_c}{I}$ can be found by substituting Equation (B.6) into Equation (B.4).

Appendix C

MATLAB Code for Ray Tracing Analysis

```
%===========================================================================
%       SPHERES Optical Payload Ray Tracing Analysis Code
%       for Sub Aperture Metrology
%===========================================================================
% written by Ryan Lim
% Sep 29th, 2005

clear all;
dia_mirror=0.5*0.0254; %diameter of mirror = 0.5 inch

%typical beam splitter side length in [m] from Edmund Optics
BS=0.001*[5, 6.25, 10, 12.5, 15, 20, 25, 30, 35, 40, 45, 50];

%typical retroreflector inner diamemter sizes in [m] from Edmund Optics
RR=0.001*[6.35, 12.7, 25.4,38.1, 50.8, 63.5];
h=0.01; %distance between center of Mirror2 and the top face of the BS

n_BS=1.5; %index of refraction for the glass in the BS
```

```
distance_lens_BS=0.005; %distance between focusing lens and the BS
distance_CCD_lens=0.02247; %distance between focusing lens and CCD

%Focusing Lens Properties
%P32-489
n_f_lens=1.5; %index of refraction for the glass in the focusing lens
dia_f_lens=0.025; %diameter of the focusing lens

% t_f_lens_edge=0; % thin lens approximation
% t_f_lens_center=0; % thin lens approximation
% t_f_lens=0; %thin lens approximation

t_f_lens_edge=0.0029; %edge thickness of the focusing lens
t_f_lens_center=0.008; %center thinkness of the focusing lens
t_f_lens=(t_f_lens_edge+t_f_lens_center)*0.5; %thickness of the lens
R1_f=0.03194; %radius of curvarture for the first surface of the lens
R2_f=-0.03194; %radius of curvarture for the second surface of the lens

data_passed_M1=[]; data_passed_M2=[];

for R=.5:0.5:0.5 %vary range from 0.5m to 1m,3m
for i=1:1:length(BS) %try different BS lengths
d_BS=BS(i); %side length of the BS
    for j=1:1:length(RR) %vary RR
    d_RR=RR(j); %inner diameter of RR

    thetaM1_passed=[];
    thetaM2_passed=[];
    pass_successful_M1=0;
    pass_successful_M2=0;
```

```
        for theta=-2:0.01:2 %vary theta (degrees)

%==========================================================================
%Sub-Aperture Metrology - Mirror 1
%==========================================================================

pass_flag=1;
thetaM1=theta*pi/180; %conversion from degrees to radians

%hitting Mirror2
if abs(0.01*tan(2*thetaM1)) > 0.5*dia_mirror pass_flag=0; end
if pass_flag%1
%hitting the BS
if abs((0.01+h)*tan(2*thetaM1))>0.5*d_BS pass_flag=0; end
if pass_flag%2
%going out from the beam splitter
thetaG1=asin(sin(2*thetaM1)/n_BS);
k=(0.5*d_BS-(h+0.01)*tan(2*thetaM1))/sin(thetaG1+45*pi/180)*sin(45*pi/180);
y_BS_right=0.5*d_BS-k*cos(thetaG1)+(d_BS-k*cos(thetaG1))*tan(thetaG1);
if abs(y_BS_right)>0.5*d_BS pass_flag=0; end
if pass_flag%3
%hitting the Retroreflector
y_RR=y_BS_right+R*tan(2*thetaM1); if abs(y_RR)>0.5*d_RR pass_flag=0;
%disp('Beam does not hit retroreflector')
end
if pass_flag%4
%returning to the BS and going out towards the lens
e1=(0.5*d_RR-abs(y_RR))*(1-1/(1+tan(2*abs(thetaM1))));
```

```
v1=abs(y_RR)+e1;
z1=2*v1/sin(45*pi/180-2*abs(thetaM1))*sin(135*pi/180);
delta1=z1*sin(90*pi/180-4*abs(thetaM1));
y1=delta1/cos(2*thetaM1)*sign(thetaM1);
y_BS_left=y_BS_right-y1-d_BS*tan(thetaG1); if abs(y_BS_left)>d_BS/2
pass_flag=0;
%disp('Failed: beam does not get out of the BS towards focusing lens')
end
if pass_flag%5
%Going into the lens
d_lens_minimum=abs(y_BS_left-distance_lens_BS*tan(2*thetaM1))*2; if
dia_f_lens<d_lens_minimum pass_flag=0;
%disp('FAILED: Use bigger Lens!');
end
if pass_flag%6
alpha_in=-2*thetaM1; %note the negative sign!
y_in=y_BS_left-distance_lens_BS*tan(2*thetaM1);
alpha_out=(1+(n_f_lens-1)/n_f_lens*t_f_lens/R2_f)*alpha_in-((n_f_lens-1)...
    *(1/R1_f-1/R2_f)+(n_f_lens-1)^2*t_f_lens/n_f_lens/R1_f/R2_f)*y_in;
y_out=t_f_lens/n_f_lens*alpha_in+(1-(n_f_lens-1)/n_f_lens*t_f_lens/R1_f)...
    *y_in;

%Focusing onto the CCD
y_CCD=y_out+distance_CCD_lens*tan(alpha_out);

if abs(y_CCD) < 0.0036/2 %0.0036 m = horizontal dimension of the CCD sensor
%disp('Success: Beam gets focused onto CCD');
pass_successful_M1=1; thetaM1=thetaM1*180/pi;
thetaM1_passed=[thetaM1_passed;thetaM1]; end
end%6
```

```
end%5
end%4
end%3
end%2
end%1


%==========================================================================
%Sub-Aperture Metrology - Mirror 2
%==========================================================================
pass_flag=1;
thetaM2=theta*pi/180; %conversion from degrees to radians



%hitting the BS
if abs(h*tan(2*thetaM2))>0.5*d_BS pass_flag=0; end
if pass_flag%1
%going out from the beam splitter
thetaG2=asin(sin(2*thetaM2)/n_BS);
x_BS_right=h*tan(2*thetaM2)+d_BS*tan(thetaG2);%on the right face of the BS
if abs(x_BS_right)>0.5*d_BS pass_flag=0; end
if pass_flag%2
%hitting the Retroreflector
x_RR=x_BS_right+R*tan(2*thetaM2); if abs(x_RR)>0.5*d_RR pass_flag=0;
%disp('Beam does not hit retroreflector')
end
if pass_flag%3
%returning to the BS and going out towards the lens

e2=(0.5*d_RR-abs(x_RR))*(1-1/(1+tan(2*abs(thetaM2))));
```

```
v2=abs(x_RR)+e2;
z2=2*v2/sin(45*pi/180-2*abs(thetaM2))*sin(135*pi/180);
delta2=z2*sin(90*pi/180-4*abs(thetaM2));
k2=delta2/cos(2*thetaM2)*sign(thetaM2);
x_BS_left=x_BS_right-k2-d_BS*tan(thetaG2); if abs(x_BS_left)>d_BS/2
pass_flag=0;
%disp('Failed: beam does not get out of the BS towards focusing lens')
end
if pass_flag%4
%Going into the lens
d_lens_minimum=abs(x_BS_left-distance_lens_BS*tan(2*thetaM2))*2; if
dia_f_lens<d_lens_minimum pass_flag=0;
%disp('FAILED: Use bigger Lens!');
end
if pass_flag%5
alpha_in=-2*thetaM2; %note the negative sign!
x_in=x_BS_left-distance_lens_BS*tan(2*thetaM2);
alpha_out=(1+(n_f_lens-1)/n_f_lens*t_f_lens/R2_f)*alpha_in-((n_f_lens-1)...
*(1/R1_f-1/R2_f)+(n_f_lens-1)^2*t_f_lens/n_f_lens/R1_f/R2_f)*x_in;
x_out=t_f_lens/n_f_lens*alpha_in+(1-(n_f_lens-1)/n_f_lens*t_f_lens/R1_f)...
*x_in;

%Focusing onto the CCD
x_CCD=x_out+distance_CCD_lens*tan(alpha_out);

if abs(x_CCD) < 0.0048/2 %0.0048 m = vertical dimension of the CCD sensor
%disp('Success: Beam gets focused onto CCD');
pass_successful_M2=1; thetaM2=thetaM2*180/pi;
thetaM2_passed=[thetaM2_passed;thetaM2]; end
end%5
```

```
end%4
end%3
end%2
end%1



end%vary theta

%displaying results
if pass_successful_M1 max_thetaM1=max(thetaM1_passed);
min_thetaM1=min(thetaM1_passed); data_passed_M1=[data_passed_M1; R,
d_BS, d_RR, min_thetaM1, max_thetaM1]; end

if pass_successful_M2 max_thetaM2=max(thetaM2_passed);
min_thetaM2=min(thetaM2_passed); data_passed_M2=[data_passed_M2; R,
d_BS, d_RR, min_thetaM2, max_thetaM2]; end

end%vary RR
end%vary BS
end%vary range
```

Appendix D

Electronic Schematics of Precision Pointing Optical Payload

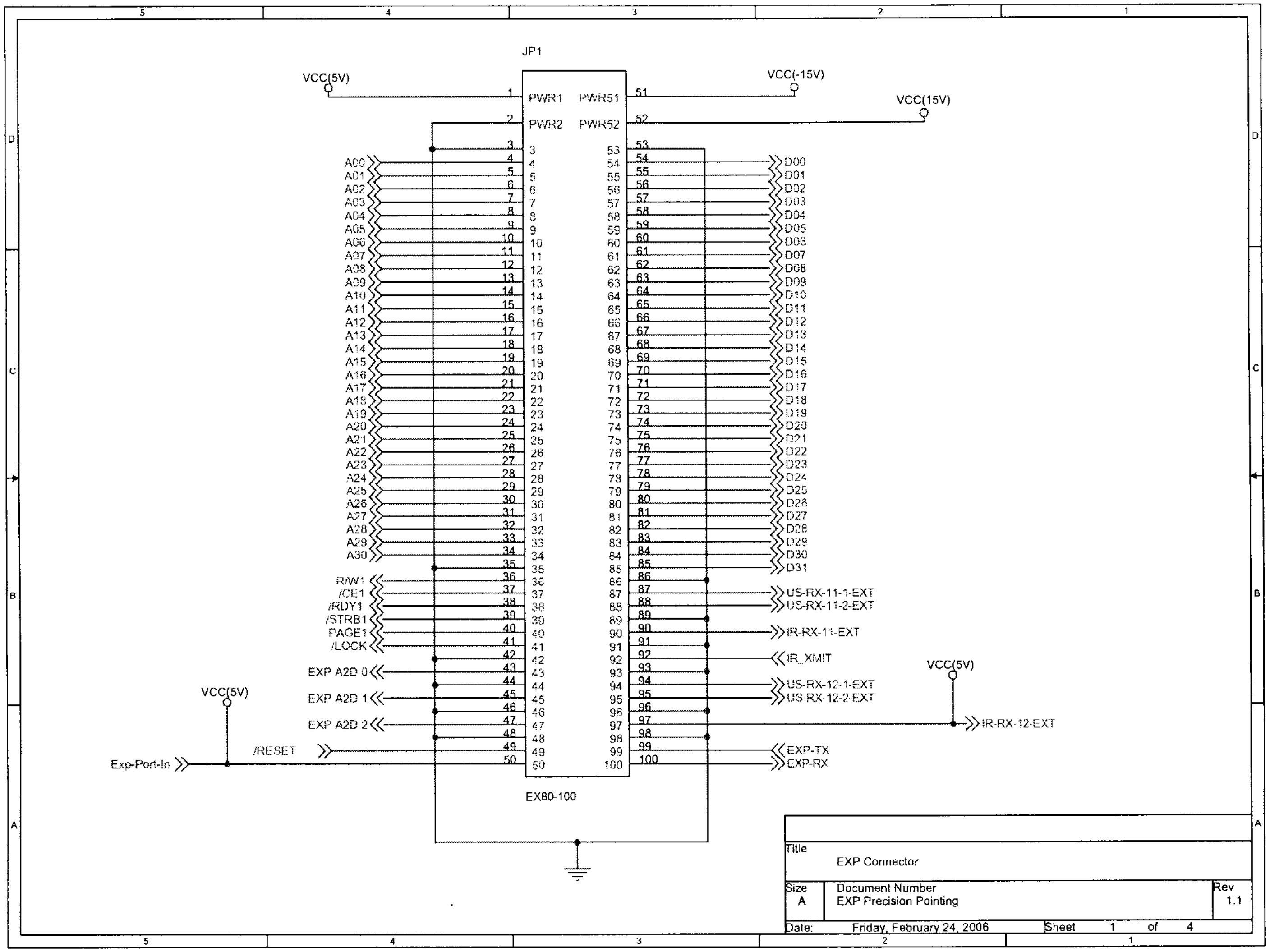

Title
EXP Connector

Size: A
Document Number: EXP Precision Pointing
Rev: 1.1

Date: Friday, February 24, 2006
Sheet 1 of 4

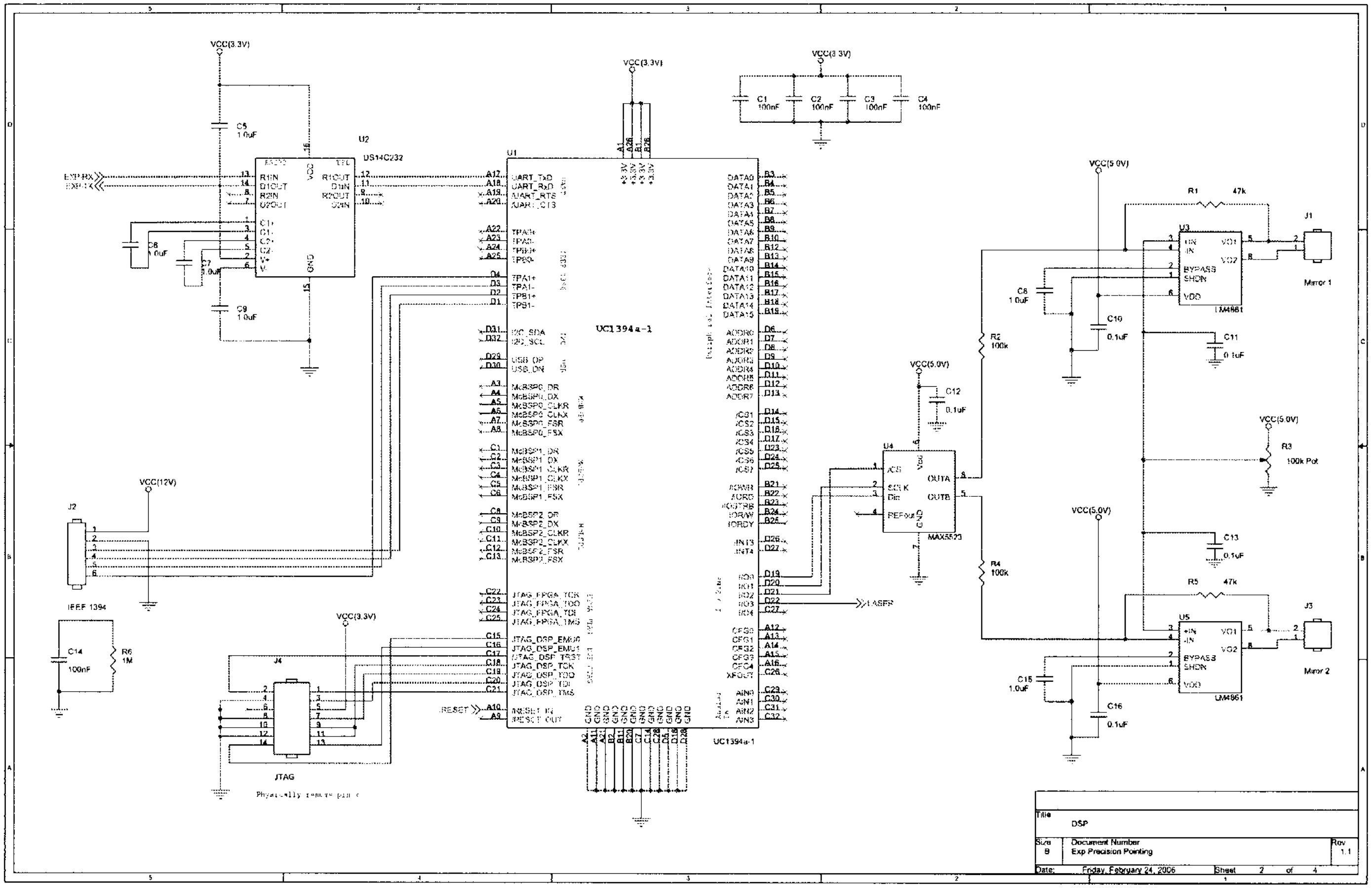
VCC(3.3V)
C5
1.0uF
U2
US14C232
EXP.RX
EXP.TX
R1IN
D1OUT
R2IN
D2OUT
R1OUT
D1IN
R2OUT
D2IN
C1+
C1-
C2+
C2-
V+
V-
VDD
GND
C6
1.0uF
C7
1.0uF
C9
1.0uF
U1
UART_TxD
UART_RxD
UART_RTS
UART_CTS
TPA0+
TPA0-
TPB0+
TPB0-
TPA1+
TPA1-
TPB1+
TPB1-
I2C_SDA
I2C_SCL
USB_DP
USB_DN
McBSP0_DR
McBSP0_DX
McBSP0_CLKR
McBSP0_CLKX
McBSP0_FSR
McBSP0_FSX
McBSP1_DR
McBSP1_DX
McBSP1_CLKR
McBSP1_CLKX
McBSP1_FSR
McBSP1_FSX
McBSP2_DR
McBSP2_DX
McBSP2_CLKR
McBSP2_CLKX
McBSP2_FSR
McBSP2_FSX
JTAG_FPGA_TCK
JTAG_FPGA_TDO
JTAG_FPGA_TDI
JTAG_FPGA_TMS
JTAG_DSP_EMU0
JTAG_DSP_EMU1
JTAG_DSP_TRST
JTAG_DSP_TCK
JTAG_DSP_TDO
JTAG_DSP_TDI
JTAG_DSP_TMS
RESET_IN
RESET_OUT
RESET
UC1394a-1
DATA0
DATA1
DATA2
DATA3
DATA4
DATA5
DATA6
DATA7
DATA8
DATA9
DATA10
DATA11
DATA12
DATA13
DATA14
DATA15
ADDR0
ADDR1
ADDR2
ADDR3
ADDR4
ADDR5
ADDR6
ADDR7
/CS1
/CS2
/CS3
/CS4
/CS5
/CS6
/CS7
/OWR
/ORD
/OSTRB
/ORW
/ORDY
INT3
INT4
IO0
IO1
IO2
IO3
IO4
CFG0
CFG1
CFG2
CFG3
CFG4
XFOUT
AIN0
AIN1
AIN2
AIN3
GND
LASER
VCC(3.3V)
C1
100nF
C2
100nF
C3
100nF
C4
100nF
J2
VCC(12V)
IEEE 1394
C14
100nF
R6
1M
J4
VCC(3.3V)
JTAG
Physically remove pin 6
VCC(5.0V)
C12
0.1uF
U4
/CS
SCLK
Din
REFout
OUTA
OUTB
Vdd
GND
MAX5523
R2
100k
R4
100k
VCC(5.0V)
R1
47k
U3
+IN
-IN
BYPASS
SHDN
VDD
VO1
VO2
LM4861
J1
Mirror 1
C8
1.0uF
C10
0.1uF
C11
0.1uF
VCC(5.0V)
R3
100k Pot
C13
0.1uF
VCC(5.0V)
R5
47k
U5
+IN
-IN
BYPASS
SHDN
VDD
VO1
VO2
LM4861
J3
Mirror 2
C15
1.0uF
C16
0.1uF
Title
DSP
Size
B
Document Number
Exp Precision Pointing
Rev
1.1
Date:
Friday, February 24, 2006
Sheet
2
of
4

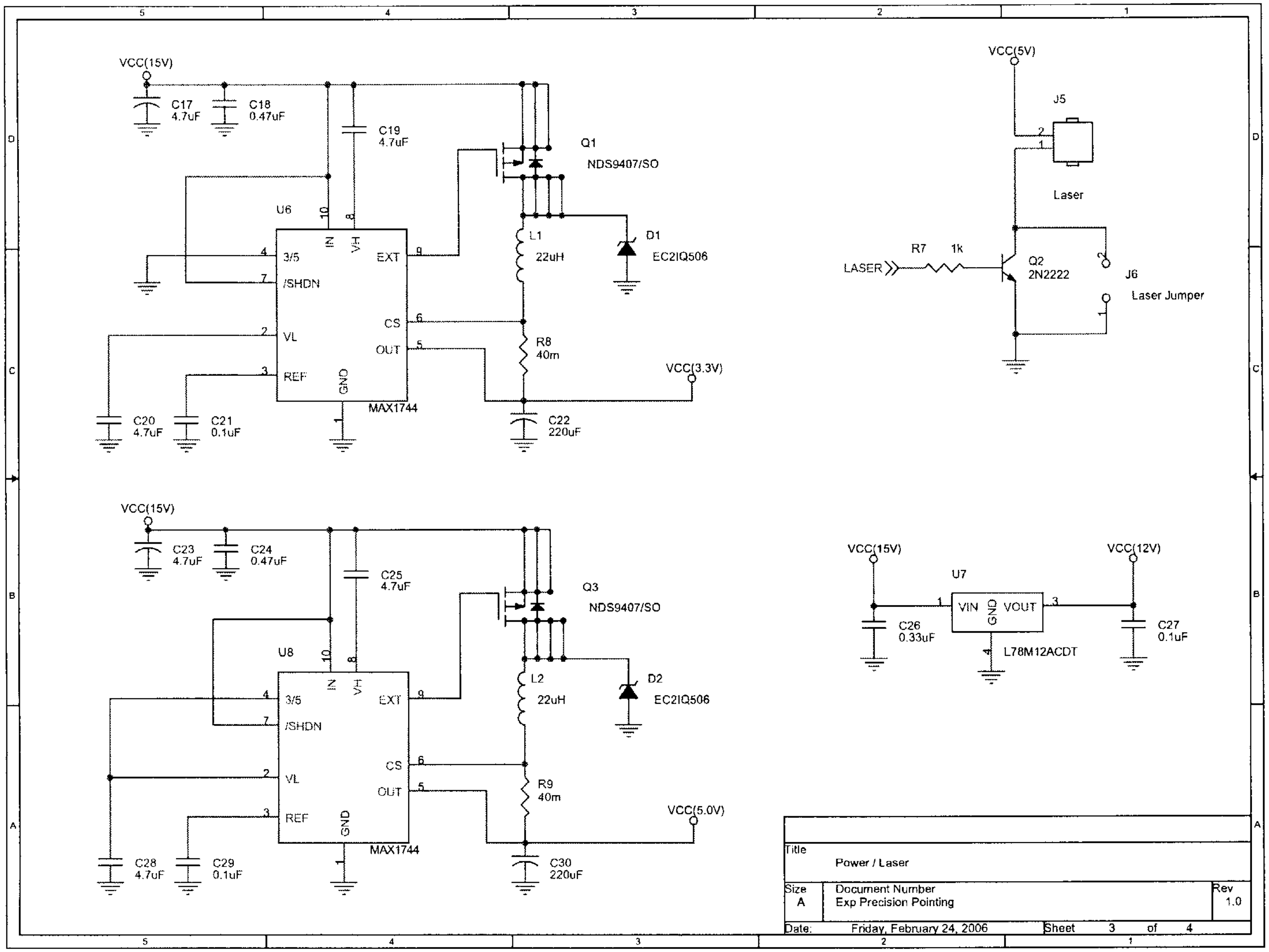
VCC(15V)
C17
4.7uF
C18
0.47uF
C19
4.7uF
Q1
NDS9407/SO
U6
10
IN
8
VH
EXT
9
4
3/5
7
/SHDN
L1
22uH
D1
EC2IQ506
CS
6
OUT
5
2
VL
3
REF
GND
1
R8
40m
VCC(3.3V)
MAX1744
C20
4.7uF
C21
0.1uF
C22
220uF
VCC(15V)
C23
4.7uF
C24
0.47uF
C25
4.7uF
Q3
NDS9407/SO
U8
L2
22uH
D2
EC2IQ506
R9
40m
VCC(5.0V)
MAX1744
C28
4.7uF
C29
0.1uF
C30
220uF
VCC(5V)
J5
Laser
R7
1k
LASER
Q2
2N2222
J6
Laser Jumper
VCC(15V)
U7
VIN
VOUT
GND
L78M12ACDT
VCC(12V)
C26
0.33uF
C27
0.1uF
Title
Power / Laser
Size
A
Document Number
Exp Precision Pointing
Rev
1.0
Date:
Friday, February 24, 2006
Sheet
3
of
4
5
4
3
2
1
D
C
B
A

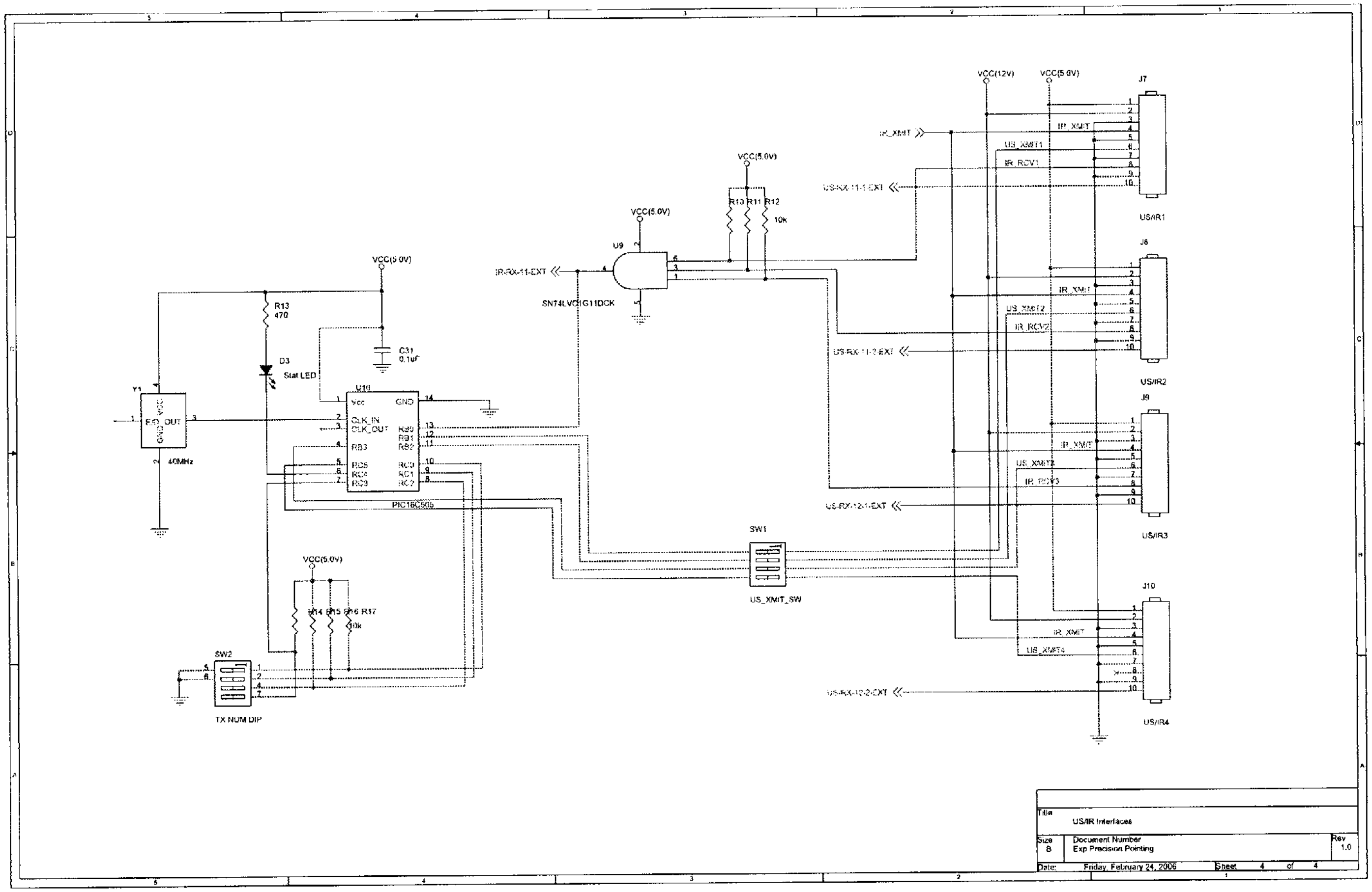

Title
US/IR Interfaces
Size B
Document Number
Exp Precision Pointing
Rev 1.0
Date: Friday, February 24, 2006
Sheet 4 of 4

Appendix E

Zernike Polynomials

The expressions [2] and sample plots of the Zernike polynomials are given in the following.

Name	**Fringe #**	**Noll #**	**Term (in fringe form)**	**Term (in Noll form)**
Piston	0	1	1	1
Tip	1	2	$\rho\cos\varphi$	$2\rho\cos\varphi$
Tilt	2	3	$\rho\sin\varphi$	$2\rho\sin\varphi$
Focus	3	4	$2\rho^2-1$	$\sqrt{3}(2\rho^2-1)$
Astigmatism	4	6	$\rho^2\cos(2\varphi)$	$\sqrt{6}\,\rho^2\cos(2\varphi)$
Astigmatism	5	5	$\rho^2\sin(2\varphi)$	$\sqrt{6}\,\rho^2\sin(2\varphi)$
Coma	6	8	$(3\rho^2-2)\rho\cos\varphi$	$\sqrt{8}(3\rho^2-2)\rho\cos\varphi$
Coma	7	7	$(3\rho^2-2)\rho\sin\varphi$	$\sqrt{8}(3\rho^2-2)\rho\sin\varphi$
Spherical	8	11	$6\rho^4-6\rho^2+1$	$\sqrt{5}(6\rho^4-6\rho^2+1)$
Trefoil	9	10	$\rho^3\cos(3\varphi)$	$\sqrt{8}\,\rho^3\cos(3\varphi)$
Trefoil	10	9	$\rho^3\sin(3\varphi)$	$\sqrt{8}\,\rho^3\sin(3\varphi)$
	11	12	$(4\rho^2-3)\rho^2\cos(2\varphi)$	$\sqrt{10}(4\rho^2-3)\rho^2\cos(2\varphi)$
	12	13	$(4\rho^2-3)\rho^2\sin(2\varphi)$	$\sqrt{10}(4\rho^2-3)\rho^2\sin(2\varphi)$
	13	16	$(10\rho^4-12\rho^2+3)\rho\cos\varphi$	$\sqrt{12}(10\rho^4-12\rho^2+3)\rho\cos\varphi$
	14	17	$(10\rho^4-12\rho^2+3)\rho\sin\varphi$	$\sqrt{12}(10\rho^4-12\rho^2+3)\rho\sin\varphi$
	16	14	$\rho^4\cos(4\varphi)$	$\sqrt{10}\,\rho^4\cos(4\varphi)$
	17	15	$\rho^4\sin(4\varphi)$	$\sqrt{10}\,\rho^4\sin(4\varphi)$

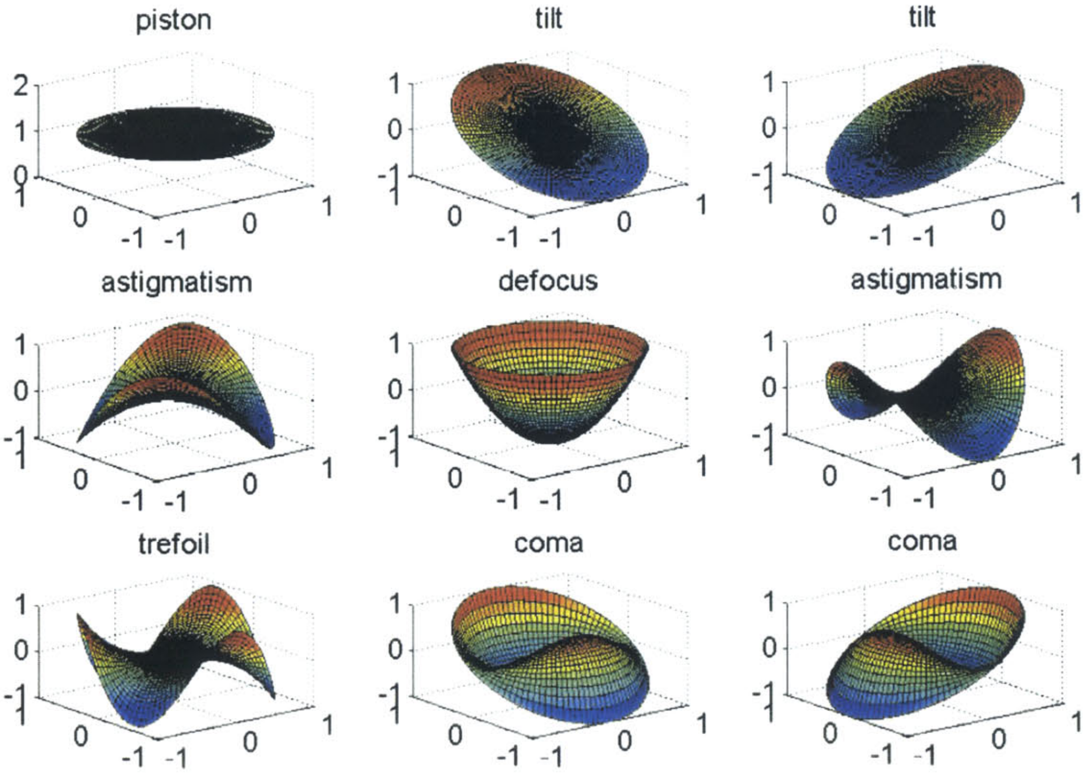
piston
2
1
0
1
0
-1 -1
0
1
tilt
1
0
-1
tilt
1
0
-1
astigmatism
1
0
-1
defocus
1
0
-1
astigmatism
1
0
-1
trefoil
1
0
-1
coma
1
0
-1
coma
1
0
-1

Bibliography

[1] MATLAB code: 'new_zern.m'. Author: George Angeli.

[2] Cost Function for Wavefront Control. Technical report, AURA New Initiatives Office.

[3] LM4861 Boomer: 1.1W Audio Power Amplifier with Shutdown Mode. Technical report, National Semiconductor.

[4] MAX5522-MAX5525 Specifications. Technical report, MAXIM.

[5] SWARM Design Document Revision 3.0. Technical report, Massachusetts Institute of Technology.

[6] NASA Origins webpage, May 2006. URL: <http://origins.jpl.nasa.gov>.

[7] Traquair webpage, May 2006. URL: <http://www.traquair.com/>.

[8] SWARM webpage, May 2006. URL: <http://spacestation.mit.edu/spheres/swarm/index.html>.

[9] JWST webpage, May 2006. URL: <http://www.jwst.nasa.gov/>.

[10] Terrestrial Planet Finder webpage, April 2006. URL: <http://planetquest.jpl.nasa.gov/TPF/tpf_index.cfm>.

[11] MACE webpage, May 2006. URL: <http://ssl.mit.edu/flight/mace.html/>.

[12] CCS webpage, May 2006. URL: <http://focus.ti.com/docs/toolsw/folders/print/ccstudio.html>.

[13] George Z. Angeli and Brooke Gregory. Linear optical model for a large ground based telescope.

[14] Carl Blaurock. *Disturbance-Optics-Controls-Structures (DOCS): NASTRAN Reference Manual.* Nightsky Systems, Inc., Raleigh, NC, Nov. 19, 2004.

[15] Carl Blaurock. *Disturbance-Optics-Controls-Structures (DOCS) Overview.* Nightsky Systems, Inc., Raleigh, NC, 2004.

[16] Soon-Jo Chung, Danielle Adams, Alvar Saenz-Otero, Edmund Kong, David W. Miller, David Leisawitz, Enrico Lorenzini, and Steve Sell. SPHERES Tethered Formation Flight Testbed: Advancements in Enabling NASA's SPECS Mission. In *SPIE Astronomical Telescopes and Instrumentation Symposium*, Orlando, FL, May 2006.

[17] Soon-Jo Chung, David W. Miller, and Olivier L. de Weck. ARGOS testbed: study of multidisciplinary challenges of future spaceborne interferometric arrays. In *Optical Engineering*, volume 43, Sep. 2004.

[18] A. Dressler. HST and Beyond - Exploration and the Search for Origins: A Vision for Ultraviolet-Optical-Infrared Space Astronomy. *Association of Universities for Research in Astronomy*, 1, May 1996.

[19] C. Eyerman and M. Shea. A Systems Engineering Approach to Disturbance Minimization for Spacecraft Utilizing Controlled Structures Technology. Technical report, Massachusetts Institute of Technology, Space Systems Laboratory.

[20] Gene F. Franklin, J. David Powell, and Michael Workman. *Digital Control of Dynamic Systems.* Addison-Wesley, Menlo Park, CA, 3^{th} edition, 1998.

[21] Mark O. Hilstad, John P. Enright, and Arthur G. Richards. The SPHERES Guest Scientist Program. URL: <http://ssl.mit.edu/spheres/gsp/>, Massachusetts Institute of Technology, 2003.

[22] Mark Ole Hilstad and David W. Miller. A Multi-Vehicle Testbed and Interface Framework for the Development and Verification of Separated Spacecraft Control Algorithms. Master's thesis, Massachusetts Institute of Technology, Cambridge, MA, June 2002.

[23] Elizabeth Jordan, Andrzej Stewart, Scott A. Uebelhart, and David W. Miller. Parametric modeling of space telescope architectures. In *SPIE Astronomical Telescopes and Instrumentation*, Orlando, Florida, May 24-31 2006.

[24] Edmund M. Kong, Alvar Saenz-Otero, Simon Nolet, Dustin S. Berkovitz, and David W. Miller. SPHERES as a Formation Flight Algorithm Development and Validation Testbed: Current Progress and Beyond. In *2nd International Symposium on Formation Flying Missions and Technologies*, Washington, DC, Sep. 14-16, 2004.

[25] Peter R. Lawson and Jennifer A. Dooley. Technology Plan for the Terrestrial Planet Finder Interferometer. Technical report, Jet Propulsion Laboratory, Pasadena, CA., June 2005.

[26] D.W. Miller, J. de Luis, and E.F. Crawley. Dynamics and Control of Multipayload Platforms: The Middeck Active Control Experiment (MACE). In *41st International Astronautical Federation Congress*, Dresden, GDR, Oct. 1990.

[27] Simon Nolet. Experimental Measurement of the Inertia of the New Air Carriage. MIT Space Systems Laboratory internal memorandum.

[28] Simon Nolet, Edmund Kong, and David W. Miller. Autonomous docking algorithm development and experimentation using the SPHERES testbed. In *Spacecraft Platforms and Infrastructure*, volume 5419 of *Proc. SPIE*, pages 1–15, Sep. 2004.

[29] ORSYS GmbH. *DCAM API for UC1394a-1 V1.1 User's Guide*, 2004.

[30] C. Perrygo and R. Burg. Hand calculation of line-of-sight sensitivity to optics displacements. Jan. 1999.

[31] Glenn Puchtel. *Dynamic Data Exchange for Os/2 Programmers*. Van Nostrand Reinhold, 1995.

[32] Lennon Rodgers and David W. Miller. Concepts and Technology Development for the Autonomous Assembly and Reconfiguration of Modular Space Systems. Master's thesis, Massachusetts Institute of Technology, Cambridge, MA, December 2005.

[33] Alvar Saenz-Otero. SPHERES Expansion Port Interface Control Document. Technical report, Massachusetts Institute of Technology.

[34] Alvar Saenz-Otero and David W. Miller. *Design Principles for the Development of Space Technology Maturation Laboratories Aboard the International Space Station.* PhD thesis, Massachusetts Institute of Technology, Cambridge, MA, May 2005.

[35] Alvar Saenz-Otero and David W. Miller. SPHERES: a platfrom for formation-flight research. In *UV/Optical/IR Space Telescopes: Innovative Technologies and Concepts II conference*, San Diego, CA, Aug. 2005.

[36] ZEMAX Development Corporation. *ZEMAX Optical Design Program User's Guide*, 2005.